TIME-DOMAIN COUPLED SIMULATIONS OF MULTI-UNIT DYNAMIC SYSTEMS IN THE OCEAN

A Dissertation

by

CHUNG-KUK JIN

Submitted to the Office of Graduate and Professional Studies of
Texas A&M University
in partial fulfillment of the requirements for the degree of

DOCTOR OF PHILOSOPHY

Chair of Committee,	Moo-Hyun Kim
Co-Chair of Committee,	Robert Randall
Committee Members,	Kuang-An Chang
	Steven DiMarco
	Heonyong Kang
Head of Department,	Sharath Girimaji

May 2019

Major Subject: Ocean Engineering

ABSTRACT

Multi-unit coupled dynamic systems, which can be widely applicable to ocean engineering, are necessary. In this study, the coupled numerical simulation program, which solves multi-body dynamics, has been developed based on the in-house program, CHARM3D. Through the developed program, two different problems, which require multi-body dynamics, are solved in the time domain.

The first application is to analyze the dynamic behavior of the surface riding wave energy converter (SR-WEC). Two rigid-body dynamic equations of motion are derived in the time domain, and wave, generator, and sliding forces are considered. Wave forces are computed in the frequency domain using the diffraction-radiation program, WAMIT, and used for time-domain analysis. In addition, generator dynamics is based on the resister-inductor (RL) circuit, and the generator force, the interaction force between two bodies estimated by the Lorentz force, is computed. The sliding force is also calculated by using the sliding mechanism of an object. The developed program is validated by comparing with experiments, which provides reliability of the program. Performance evaluation of the SR-WEC is further conducted after parametric studies. A substantial performance improvement of the SR-WEC can be achieved through parametric studies.

The second application is to investigate the dynamic behavior of a submerged floating tunnel (SFT). First, global dynamic analysis of a 700-m-long SFT section considered in the South Sea of Korea is carried out under survival wave and seismic excitations. The hydro-elastic equation of motion for the tunnel and mooring lines is based

on rod-theory-based finite element formulations with the Galerkin method with a fully coupled full matrix. The dummy-connection-mass method is devised to conveniently connect tunnel elements and mooring lines with linear and rotational springs. Hydrodynamic forces on the SFT are evaluated by the modified Morison equation for a moving object so that the hydrodynamic forces by wave or seismic excitations can be computed at its instantaneous positions at each time step. In the case of a seabed earthquake, both the dynamic effect transferred through mooring lines and the seawater-fluctuation-induced seaquake effect are considered. For validation purposes, the hydro-elastic analysis results by the developed numerical simulation code are compared with those by a commercial program, OrcaFlex, which shows excellent agreement between them. For the given design condition, extreme storm waves cause higher hydro-elastic responses and mooring tensions than those of the severe seismic case. Second, the tunnel-mooring-line-vehicle coupled time-domain numerical model is developed. A vehicle is modeled by using the rigid-body dynamic method. The interaction between the tunnel and the vehicle is taken into consideration based on the correspondence assumption and the simplified Kalker linear creep theory. To validate the proposed model, dynamic responses and mooring tensions are compared with results generated by OrcaFlex under the still water condition. The effects of the moving vehicle on dynamic responses of the tunnel is small, and the moving vehicle meets the safety criteria at high vehicle speed under the inputted environmental conditions.

DEDICATION

This dissertation is dedicated,

with love and respect,

to my parents, Yangkyu Jin and Eunsuk Cha

and my wife, He Yang.

ACKNOWLEDGEMENTS

Foremost, I would like to express my sincere appreciation to my advisor, Professor Moo-Hyun Kim, for his continuous support of my Ph.D. research, for his great guidance, motivation, and enthusiasm.

I would like to appreciate my co-chair, Professor Robert Randall, for his continuous guidance and support throughout my Ph.D. research. Also, I would like to thank my committee members, Prof. Kuang-An Chang, Prof. Steven DeMarco, and Dr. Heonyong Kang, for their valuable guidance and support thought my Ph.D. research. I also thank my colleagues in the Smart Ocean Systems Laboratory, HanSung Kim, WooChul Chung, Farid Putra Bakti, and Zaid Zainuddin for sharing research ideas and their encouragement. In particular, I appreciate many colleagues, Dr. Heonyong Kang, Farid Putra Bakit, Zaid Zainuddin, Dr. Wei-Liang Chuang, and Jitae do, for their much and continuous help with experiments of the wave energy converter.

Last but not least, I really thank my parents, parents-in-law, and my brother for their love and continuous encouragement, and my wife He Yang for not only her love and the greatest patience but also investigating several topics together so that I can write good dissertation.

CONTRIBUTORS AND FUNDING SOURCES

Contributors

This work was supervised by dissertation committees consisting of Professors Moo-Hyun Kim, Robert Randall, Kuang-An Chang, and Heonyong Kang of the Department of Ocean Engineering and Professor Steven DiMarco of the Department of Oceanography.

The experiments in Chapter II were conducted in part by Farid Bakti of the Department of Ocean Engineering.

All other work conducted for the dissertation was completed by the student independently.

Funding Sources

This work was made possible in part by the National Research Foundation of Korea (NRF) grant funded by the Korea government (MSIT) under Grant Number 2017R1A5A1014883.

TABLE OF CONTENTS

Page

LIST OF FIGURES

Page

LIST OF TABLES

Page

CHAPTER I

INTRODUCTION

The major topics in this dissertation is the development of the surface-riding wave energy converter using the permanent magnet linear generator presented in CHAPTER II and global-performance analysis of a submerged floating tunnel and tunnel-mooring-line-vehicle interaction under wave and seismic excitations presented in CHAPTER III.

The work presented in this dissertation is based on the paper 'Time-domain hydro-elastic analysis of a SFT (submerged floating tunnel) with mooring lines under extreme wave and seismic excitations' published in Applied Sciences (Jin and Kim, 2018).

Introduction for CHAPTER II

Conventional energy sources based on fossil fuels have been beneficial to industrial development with high efficiency; however, it causes severe problems to the natural environment and human health simultaneously. Due to a growing interest in these issues, traditional energy sources are constrained to be produced under strict regulations, which is one of the most critical challenges for this energy source. Also, controlling the amount of greenhouse gas requires additional cost and effort, which leads to an increase in the total cost of producing energy (Herzog et al., 2001).

Utilization of renewable energy sources (RESs) has been considered as an efficient, environmentally friendly option to replace conventional energy sources. RESs, such as wind, sun, and ocean waves, provide approximately 14 % of the global energy

demand (Goldemberg, 2000). In particular, ocean waves are a promising renewable energy source because of its higher density of 2-3 kW/m^2 than other sources (wind: 0.4-0.6 kW/m^2, solar: 0.1-0.2 kW/m^2) and constant availability (90 % of the time) than solar and wind energies (20-30 % of the time) (López et al., 2013). The global net resource is approximately 3 TW as given in Table 1 (Mørk et al., 2010), and the US is one of the high potential areas for the harness of WEC devices.

Table 1. Global and regional theoretical wave power resource (GW) where P_{gross} in left column is gross power, P in middle column is power without the areas where P < 5 kW/m, and P_{net} is net power without areas where P < 5 kW/m and ice is potentially covered (Mørk et al., 2010).

Region	P_{gross} (GW)	P (GW)	P_{net} (GW)
Europe (N and W)	381	371	286
Baltic Sea	15	4	1
European Russia	37	22	3
Mediterranean	75	37	37
North Atlantic Archipelagos	111	111	111
North America (E)	115	103	35
North America (W)	273	265	207
Greenland	103	99	3
Central America	180	171	171
South America (E)	206	203	202
South America (W)	325	324	324
North Africa	40	40	40
West and Middle Africa	77	77	77
Africa (S)	178	178	178
Africa (E)	133	133	127
Asia (E)	173	164	157
Asia (SE) and Melanesia	356	283	283
Asia (W and S)	100	90	84
Asiatic Russia	172	162	23
Australia and New Zealand	590	574	574
Polynesia	63	63	63
Total (GW)	3702	3475	2985

One of the main concerns for WEC development is to optimize the energy harness during conversion from wave power to electric power without much energy loss, and a proper power take-off (PTO) system can be a way to improve conversion efficiency. The PTO system is generally designed by using hydraulic systems (e.g., Pelamis WEC), turbines (e.g., Wave Dragon WEC) and direct-drive linear generators (e.g., PowerBuoy OPT WEC). Hydraulic and turbine PTO systems require additional energy conversion to operate the rotary generator, making the system complex. The complexity of this process can create reliability and maintenance issues (Baker and Mueller, 2001). Besides, additional energy loss is inevitable during the double energy-conversion process. However, the direct-drive linear generators do not require this intermediate step to generate electric power from wave power; therefore, OPEX can be small as well as the design is simple (Drew et al., 2009).

The direct-drive linear generator, which is also known as a permanent magnet linear generator (PMLG), has widely been proposed to generate electricity in the ocean. The PMLG produces electricity from the relative motion between a coiled armature and a permanent magnet, and most of them gain energy from the relative heave motion. For example, Parthasarathy (2012) and Prudell et al. (2010) designed a rectangular and tubular dual-buoy WEC. These two studies were based on the assumption that the heave motion of one body exactly follows wave elevation while the location of another buoy is fixed; therefore, their main focus was actually to develop a generator design without solving hydrodynamics of the dual buoy. Kim et al. (2017) performed experiments to investigate dual-buoy WEC to utilize resonance motions of two bodies and the moon-pool that cover

wide wave-frequency ranges. Stelzer and Joshi (2012) investigated a point-absorber WEC, which is one of the most popular WEC types with the PMLG, and feasibility studies are conducted under random waves excitations with assumptions of hydrodynamic coefficients. Zheng et al. (2015) analyzed the electromagnetic force of the PMLG in the point-absorber WEC. Lejerskog et al. (2015) conducted large-scale tests of the point absorber in the Lysekil research side in Sweden, and they concluded that higher power output can be achieved in upward motions than downward motions. Besides, through the parametric study, power output can be maximized. Park et al. (2013) evaluated the WEC equipped with two masses and three springs to maximize the relative velocity by inducing resonance. Gao et al. (2016) evaluated a fully floating WEC equipped with the PMLG, and springs are installed to increase the performance.

In this study, a novel WEC concept with the PMLG is developed, called as the surface riding WEC (SR-WEC). The SR-WEC is specially devised to generate appreciable electrical power even in low sea conditions, which cover 80 to 90 % of annual sea state. There are several advantages of the SR-WEC. First, regardless of sea states, the wave slopes are about the same, so the system is particularly effective in low sea states, which cover more than 90% of annual sea conditions. Other existing WECs are not very efficient in such low sea states. The SR-WEC has relative velocity driven by the gravity acceleration whereas existing devices utilize inertia acceleration usually in an order less scale of the gravity. Secondly, a tubular design leads to easier maintenance by merely replacing components. Thirdly, the generated energy is clean without any emission of greenhouse gas. Finally, the movable ring-mass can easily be combined into the system

for the active control to generate resonant pitch motions depending on variable sea states if necessary.

Feasibility studies are carried out using frequency-domain and time-domain numerical simulations. In the frequency-domain analysis, not only wave forces and moments but also hydrodynamic coefficients are acquired using a widely used 3D diffraction-radiation program, WAMIT. In the time-domain numerical simulation, floater-mooring-line-generator coupled dynamic analysis is carried out using the in-house program, CHARM3D, with code development. Generator dynamics is coupled with the CHARM3D; therefore, the electricity generation from 6 DOFs is numerically feasible. Design optimization is also carried out to optimize the performance of the SR-WEC.

Introduction for CHAPTER III

The submerged floating tunnel (SFT) is an innovative solution used to cross deep waterways (Ge et al., 2010; Paik et al., 2004). The SFT mainly consists of a tunnel for vehicle transportation and mooring lines for station-keeping. The tunnel is usually positioned at a certain submergence depth, typically greater than 20 m, with positive net buoyancy that is balanced by mooring lines anchored in the seabed (Di Pilato et al., 2008; Long et al., 2009).

Considering that wave, current, and wind effects are greatly reduced, the cost is almost constant along the length (Faggiano et al., 2005), and the structure does not obstruct ship passage, the SFT has been regarded as a competitive alternative to floating bridges and immersed tunnels. In this regard, since Norway's first patent in 1923 (Muhammad et

al., 2017), many proposals and case studies have been published worldwide, which includes Høgsfjord/Bjørnafjord in Norway (Engebretsen et al., 2017; Remseth et al., 1999; Skorpa, 1989), the Strait of Messina in Italy (Faggiano et al., 2001), Funka Bay in Japan (Fujii, 1996; Lu et al., 2011), Qiandao Lake in China (Martinelli et al., 2011; Mazzolani et al., 2008), and the Mokpo-Jeju SFT in Korea (Han et al., 2016). Even though there is no installed large-scale structure in the world despite extensive research (Lee et al., 2017), the first construction of the SFT is being considered by Norwegian Public Road Administration (NPRA) with global interest (Ghimire and Prakash, 2017).

To provide sufficient confidence for the concept, feasibility studies under diverse catastrophic environmental conditions, such as extreme waves and earthquakes, must be extensively studied in advance. Along with this line, numerous researches have been carried out to verify structural safety in wave and seismic excitations on the SFT. Regarding wave-excitation effects, Kunisu et al. (1994) evaluated the effect of mooring-line configurations on SFT dynamic responses including possible snap loading. Lu et al. (2011) and Hong et al. (2016) focused on slack mooring phenomena at various buoyancy-weight ratios (BWRs) of the SFT and inclination angles of mooring lines. Long et al. (2009) conducted parametric studies to investigate the effects of the BWR and mooring-line stiffness. Dynamic motions at varying BWRs and the corresponding comfort index were investigated by Long et al. (2015). Seo et al. (2015) compared experimental results with a simplified numerical approach for a segment of the SFT. Chen et al. (2018) evaluated the influence of VIV (vortex induced vibration) of mooring lines on the SFT dynamic responses using a simplified numerical model. Also, with regard to seismic-

excitation effects, Di Pilato et al. (2008) carried out a coupled dynamic analysis to investigate the effect of wave and seismic excitations. Martinelli et al. (2011) suggested detailed procedures to generate artificial seismic excitations and performed the corresponding structural analysis. Dynamic responses at various shore connections under transverse earthquake were investigated by Xiao and Huang (2010). Martinelli et al. (2016) and Wu et al. (2018) focused on hydrodynamic fluid-structure interaction induced by vertical fluid fluctuations known as the seaquake. Mirzapour et al. (2017) derived simplified analytical solutions for 2D and 3D cases and computed SFT dynamic responses in diverse stiffness conditions. Muhammad et al. (2017) compared the dynamic effects induced by wave and seismic excitations.

During the past decade, various SFT-related studies have been carried out in our research lab. Cifuentes et al. (2015) compared the dynamics of a moored-SFT segment in regular waves for various BWRs and mooring types between experimental results and numerical simulations. For the numerical simulations, both commercial program (OrcaFlex) and the developed, in-house program CHARM3D were used for cross-checking. Lee et al. (2017) further investigated the dynamics of the short tunnel segment under irregular waves and random seabed earthquakes. Then, the initial studies of hydro-elastic responses of a long SFT with many mooring lines by random waves and seabed earthquakes were conducted by Jin and Kim (2017) and Jin et al. (2017) by using commercial software, OrcaFlex. However, when using OrcaFlex for seismic excitations, indirect modeling with many seabed dummy masses has to be introduced instead of direct inputs of dynamic boundary conditions at those anchor points.

To add the capability of hydro-elastic analyses of a long SFT with many mooring lines in the in-house coupled dynamic-analysis program, a new approach called 'dummy-connection-mass method' is developed. The equation of motion for the line element is derived by rod theory, and finite element modeling is implemented by using the Galerkin method. Linear and rotational springs are employed to connect several objects with given connection conditions conveniently. The Adams-Moulton implicit integration method combined with the Adam-Bashforth explicit scheme is used for the time-domain-integration method so that stable and time-efficient numerical integration can be done without iteration.

In the Case Study I, the newly developed program is applied to calculate the hydro-elastic responses of a 700m-long SFT (with both ends fixed) with many mooring lines by extreme random waves or severe random earthquakes. The results from the newly developed program are cross-checked against those from OrcaFlex program. In the case of seabed earthquake, the seabed motions are transferred to SFT through mooring lines and through seawater fluctuations called seaquake, which is extensively discussed in Case Study I based on the produced numerical results. In the present study, the effect of seismic-induced acoustic pressure is not considered since the resulting frequency range is much higher (Lee et al., 2016), and thus it is of little importance for the mooring design.

Furthermore, the SFT is designed for vehicle traffic; therefore, the tunnel-mooring-line-vehicle interaction should be taken into account. Tariverdilo et al. (2011) investigated the vertical dynamic response of the SFT induced by a moving load and the effect of varying levels of vehicle speed and mooring stiffness. They simplified a moving load as a

point mass and mooring lines as the continuous elastic foundation. Yuan et al. (2016) focused on vertical dynamic responses of the SFT under various vehicle speeds and moving-mass magnitudes with the simplified model. Lin et al. (2018) considered fluid-vehicle-tunnel interaction at different current velocities, BWRs, and inclination angles of the mooring line. They modeled a moving vehicle using a single mass, and interactions between the tunnel and vehicle were considered by introducing linear springs and dampers. They simplified mooring lines as the continuous elastic foundation. Besides, similar studies were carried out for the floating bridge. Shixiao et al. (2005) and Fu and Cui (2012) compared the vertical response obtained by experiments with that by numerical simulations for a floating bridge to mainly look at the effect of moving-vehicle velocity.

According to the current state of the art, the influences of a vehicle on dynamic responses of the SFT or floating the bridge were only investigated while the reverse effect on the vehicle was not considered. However, the safety and comfort of passengers are also significant factors, and related research is required for the SFT structure. In this regard, the coupled time-domain numerical model is developed to solve the tunnel-mooring-line-vehicle-interaction. The basic theory for tunnel model is the same as the Case Study I; however, for the Case Study II, a vehicle model is additionally developed. The rigid-body dynamic method is used to model a train element as seven rigid bodies, i.e., a car-body, two bogies, and four wheel-sets. The interaction between the vehicle and a tunnel is based on the correspondence assumption, and the simplified Kalker creep theory, which is widely used to solve bridge-vehicle interactions (Song et al., 2003; Zhang and Xia, 2013; ZHANG et al., 2010). Dynamic responses and mooring tensions of the structure are

investigated to evaluate structural safety. Moreover, various criteria for the train, i.e., the derailment factor, the offload factor, and the riding comfort criterion are utilized to assess the safety of passengers extensively.

CHAPTER II

DEVELOPMENT OF THE SURFACE-RIDING WAVE ENERGY CONVERTER USING THE PERMANENT MAGNET LINEAR GENERATOR

Theory and Formulation of the Two-Body SR-WEC

Introduction

Mathematical and numerical formulations to develop the two-body SR-WEC are reviewed in the section. The configuration of the SR-WEC is presented in Figure 1, which is largely divided into inner and outer cylinders. There are several significant considerations to develop the numerical model. The outer cylinder interacts with waves, and wave forces and moments on the outer cylinder should be estimated. The sliding mechanism should also be well understood. Moreover, the magnet assembly is installed in the inner cylinder, which interacts with the outer cylinder where the armature assembly is installed; thus, the magnetic force between armature and magnet assemblies is needed to be estimated. A single point mooring (SPM) system is installed for a station-keeping purpose, and the structure-mooring-line interaction should be considered. At both ends of the outer cylinder, rubber springs and dampers are positioned to reduce impact-induced fatigue by the magnet assembly; therefore, dynamics related to this impact is also investigated.

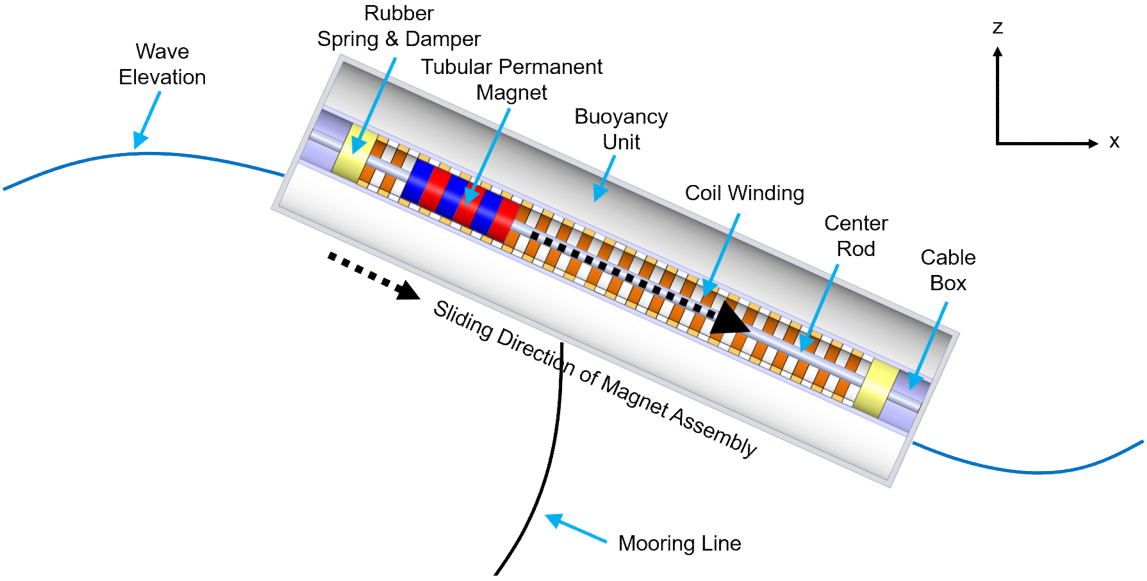

Figure 1. Configuration of the SR-WEC.

Dynamics of Floating Structures

Introduction

In this section, the dynamics of the floating structure, which can be a theoretical background for the outer cylinder, is summarized. First, the first order wave theory is reviewed. In addition, diffraction and radiation theories are presented with the first order potential forces and moments acting on a floating structure. Morison equation for slender, cylindrical structures, which allows computation of inertia and drag loads, are also presented. Finally, the equation of motion for a floating structure is presented in the time domain with consideration of external forces, i.e., the hydrodynamic forces.

Wave Theory

The boundary value problem with appropriate boundary conditions is required to be solved in order to derive the wave theory. The governing equation of fluid in CHARM3D is derived from Laplace's equation with the assumption of incompressible, irrotational, and inviscid properties:

$$\nabla^2 \Phi = 0 \tag{1}$$

The appropriate boundary conditions, i.e., kinematic and dynamic boundary conditions have to be satisfied on the free surface. The kinematic boundary condition is derived by assuming that water particles stay on the free surface at $z = \eta(x, y, t)$, and the following formulation is used to describe the kinematic boundary condition:

$$\frac{\partial \eta}{\partial t} + u\frac{\partial \eta}{\partial x} + v\frac{\partial \eta}{\partial y} - \frac{\partial \Phi}{\partial t} = 0 \tag{2}$$

where $\eta(x, y, t)$ is the free surface elevation as a function of space and time. In addition, the dynamic free-surface boundary condition describes that the pressure on the free surface at $z = \eta(x, y, t)$ is equal to a constant atmospheric pressure, which can be formulated as follows:

$$\rho\frac{\partial \Phi}{\partial t} + \frac{1}{2}\left(\Phi_x^2 + \Phi_y^2 + \Phi_z^2\right) + \rho g z = 0 \tag{3}$$

where ρ is water density and g is gravity acceleration. The bottom boundary condition is defined on the sea bottom, i.e., $z = -d$ where d is water depth. The condition means that water particles cannot penetrate the sea floor. Therefore, the velocity of water particles in the vertical direction is zero on the sea bottom as follows:

$$\frac{\partial \Phi}{\partial z} = 0 \tag{4}$$

In Laplace's equation, the exact solution is difficult to acquire because of nonlinear terms given in the free surface boundary conditions. Thus, the perturbation method with an assumption of the small wave amplitude can be utilized to obtain the approximated solution of a specific order of accuracy (Ran, 2000). The derived first-order velocity potential and free surface elevation are expressed as follows:

$$\Phi^{(1)} = \mathrm{Re}\left[-\frac{igA}{\omega} \frac{\cosh k\left(z+d\right)}{\cosh kd} e^{i\left(kx\cos\theta + ky\sin\theta - \omega t\right)} \right] \tag{5}$$

$$\eta^{(1)} = A\cos\left(kx\cos\theta + ky\sin\theta - \omega t\right) \tag{6}$$

where ω is the wave angular frequency, k is the wave number, A is the wave amplitude, and θ is the incident wave heading angle. The derived second-order velocity potential and free surface elevation are also presented as follows:

$$\Phi^{(2)} = \mathrm{Re}\left[-\frac{3}{8}\omega A^2 \frac{\cosh 2k\left(z+d\right)}{\sinh^4 kd} e^{i\left(2kx\cos\theta + 2ky\sin\theta - 2\omega t\right)} \right] \tag{7}$$

$$\eta^{(2)} = A^2 \frac{\cosh kd}{\sinh^3 kd} \cos\left(2kx\cos\theta + 2ky\sin\theta - 2\omega t\right) \tag{8}$$

A fully developed wave condition in a target location can be modeled by using the wave spectrum, e.g., the JONSWAP wave spectrum used in the North Sea, and the time history of random waves from a wave spectrum $S\left(\omega\right)$ is generated by superposition of a certain number of sinusoidal wave components with random phases:

$$\eta\left(x,t\right) = \sum_{i=1}^{N} A_i \cos\left(k_i x - \omega_i t + \varepsilon_i\right) = \mathrm{Re}\left[\sum_{i=1}^{N} A_i e^{i\left(k_i x - \omega_i t + \varepsilon_i\right)} \right] \tag{9}$$

$$A_i = \sqrt{2S(\omega_i)\Delta\omega} \tag{10}$$

where N denotes the number of wave components, $\Delta\omega$ is intervals of frequency division, and ε_i is a random phase angle produced by a random function. A generated time history is repeated with a certain time interval for long simulations; thus, to avoid the signal repetition, the following modification can be made:

$$\eta(x,t) = \mathrm{Re}\left[\sum_{i=1}^{N} A_i e^{i(k_i x - \omega_i' t + \varepsilon_i)}\right] \tag{11}$$

where $\omega_i' = \omega_i + \delta\omega_i$ and $\delta\omega_i$ is the randomly perturbed number uniformly distributed between $-\Delta\omega/2$ and $\Delta\omega/2$.

Wave Loads on Floating Structures

The estimation of wave forces on the floating structure is one of the most important issues in static and dynamic analyses. The diffraction theory is the most proper way to estimate wave loads in deep water. Morison equation is widely used for a slender object. In addition, the viscous force can be a significant factor in the dynamic analysis under extreme wave conditions and must be taken into consideration. Therefore, in this section, the diffraction theory and Morison equation are described, and both of them can be utilized to estimate the wave loads for the SR-WEC simulation.

Diffraction and Radiation Theory

The boundary value problem for the wave-floating-structure interaction is reviewed. Total velocity potential Φ should satisfy not only the Laplace's equation but

also free surface and bottom boundary conditions. The total velocity potential Φ is divided into the incident potential Φ_I, the diffraction potential Φ_D, and the radiation potential Φ_R, which can be expressed by using the perturbation method in terms of the wave slope parameter ε (Ran, 2000):

$$\Phi = \sum_{n=1}^{\infty} \varepsilon^n \Phi^{(n)} = \sum_{n=1}^{\infty} \varepsilon^n \left(\Phi_I^{(n)} + \Phi_D^{(n)} + \Phi_R^{(n)} \right) \tag{12}$$

where $\Phi^{(n)}$ represents the nth order solution of Φ. In general, first and second order solutions are generally considered in dynamic simulations of floating structures whereas higher order solutions are neglected.

Since the wave-structure interaction is solved in this study, the body boundary condition is also considered, and the body boundary condition is expressed with the surface normal vector $\mathbf{n}$ and the normal velocity vector of the structure at its surface V_n:

$$\frac{\partial \Phi}{\partial \mathbf{n}} = V_n \tag{13}$$

In addition, the diffraction and radiation potentials, i.e., Φ_D and Φ_R have to satisfy the Sommerfeld radiation condition at the far field boundary expressed as follows (Ran, 2000):

$$\lim_{r \to \infty} \sqrt{r} \left(\frac{\partial \Phi_{D,R}}{\partial r} \pm ik\Phi_{D,R} \right) = 0 \tag{14}$$

where r represents the radial distance from the center of the floating body.

First Order Boundary Value Problem

In this section, the first order boundary value problem of a floating structure with a monochromatic incident wave is described. The first order potential can be re-written by explicitly separating the time dependency as (Bae, 2013):

$$\begin{aligned}\Phi^{(1)} &= \varepsilon\left(\Phi_I^{(1)} + \Phi_D^{(1)} + \Phi_R^{(1)}\right) \\ &= \mathrm{Re}\left\{\left[\phi_I^{(1)}(x,y,z) + \phi_D^{(1)}(x,y,z) + \phi_R^{(1)}(x,y,z)\right]e^{-i\omega t}\right\}\end{aligned} \tag{15}$$

In particular, the first order incident potential $\phi_I^{(1)}$ can be re-written as:

$$\phi_1^{(1)}(x,y,z) = \mathrm{Re}\left[-\frac{igA}{\omega}\frac{\cosh k(z+d)}{\cosh kd}e^{i\mathbf{K}\cdot\mathbf{x}}\right] \tag{16}$$

where **K** and **x** represent a vector wave number with Cartesian components i.e., $(k\cos\theta, k\sin\theta, 0)$ and the position vector in the fluid, respectively, and θ is the angle of the incident wave relative to the positive x axis. Thus, the boundary value problem governing the first order diffraction and radiation potentials are finally expressed as (Bae, 2013):

$$\nabla^2\phi_{D,R}^{(1)} = 0 \qquad \text{in the fluid } (z<0) \tag{17}$$

$$\left(-\omega^2 + g\frac{\partial}{\partial z}\right)\phi_{D,R}^{(1)} = 0 \qquad \text{on the free surface } (z=0) \tag{18}$$

$$\frac{\partial\phi_{D,R}^{(1)}}{\partial z} = 0 \qquad \text{on the bottom } (z=-d) \tag{19}$$

$$\frac{\partial\phi_R^{(1)}}{\partial n} = -i\omega\mathbf{n}\cdot\left(\boldsymbol{\xi}^{(1)} + \boldsymbol{\alpha}^{(1)}\times\mathbf{r}\right) \qquad \text{on the body surface} \tag{20}$$

$$\lim_{x\to\infty}\sqrt{r}\left(\frac{\partial}{\partial r}\pm ik\right)\phi_{D,R}^{(1)}=0 \qquad \text{at far field} \tag{21}$$

where $\mathbf{r}$ denotes the position vector on the body surface, r represents the radial distance from the origin, and $\mathbf{n}$ denotes the unit normal vector pointing into the fluid domain at the body surface. Besides, the first order motions of the floating structure in the translational $\boldsymbol{\Xi}^{(1)}$ and rotational $\boldsymbol{\Theta}^{(1)}$ directions can be expressed as (Bae, 2013):

$$\boldsymbol{\Xi}^{(1)}=\mathrm{Re}\left\{\boldsymbol{\xi}^{(1)}e^{-i\omega t}\right\} \quad \boldsymbol{\xi}^{(1)}=\left\{\xi_1^{(1)},\xi_2^{(1)},\xi_3^{(1)}\right\} \tag{22}$$

$$\boldsymbol{\Theta}^{(1)}=\mathrm{Re}\left\{\boldsymbol{\alpha}^{(1)}e^{-i\omega t}\right\} \quad \boldsymbol{\alpha}^{(1)}=\left\{\alpha_1^{(1)},\alpha_2^{(1)},\alpha_3^{(1)}\right\} \tag{23}$$

where the subscripts 1, 2, and 3 represent the translational modes, i.e., surge, sway, and heave, and the rotational modes, i.e., roll, pitch, and yaw, with respect to the x, y, z axis, respectively. The six degrees of freedom of the first order motion can also be re-written as (Bae, 2013):

$$\zeta_i=\xi_i^{(1)} \qquad \text{for } i=1,2,3 \tag{24}$$

$$\zeta_i=\alpha_{i-3}^{(1)} \qquad \text{for } i=4,5,6 \tag{25}$$

The radiation potential, which denotes the fluid disturbance because of the motion of the structure, can further be decomposed as:

$$\phi_R^{(1)}=\sum_{i=1}^{6}\zeta_i\phi_i^{(1)} \tag{26}$$

where ϕ_i denotes the first order potential of the structure's motion with unit amplitude in the ith mode without the incident waves (Ran, 2000). The body boundary condition of all modes can further be represented by replacing $\phi_i^{(1)}$ as (Bae, 2013):

$$\frac{\partial \phi_i^{(1)}}{\partial n} = n_i \qquad \text{for } i=1,2,3 \tag{27}$$

$$\frac{\partial \phi_i^{(1)}}{\partial n} = \left(\mathbf{r} \times \mathbf{n}\right)_{i-3} \qquad \text{for } i=4,5,6 \tag{28}$$

on the body surface.

The first order diffraction potential $\phi_D^{(1)}$ is the disturbance to the incident wave induced by the existence of the structure in its fixed position. The velocity potential has to meet the body surface boundary condition represented in the following equation (Bae, 2013):

$$\frac{\partial \phi_D^{(1)}}{\partial n} = -\frac{\partial \phi_I^{(1)}}{\partial n} \qquad \text{on the body surface} \tag{29}$$

First Order Potential Forces

In this section, the first order hydrodynamic force acting on the floating structure is reviewed, which can be acquired by solving both the first order diffraction $\phi_D^{(1)}$ and radiation $\phi_R^{(1)}$ potentials. The hydrodynamic pressure $P(t)$, which is obtained by the perturbation method, can be expressed as (Bae, 2013):

$$P^{(1)} = -\rho \frac{\partial \Phi^{(1)}}{\partial t} \tag{30}$$

Calculation of the total force and moment on the structure at each time step can be done by integration over the instantaneous wetted body surface $S(t)$ (Bae, 2013):

$$\mathbf{F}\left(t\right)_i = \begin{cases} \iint_{S_b} Pn_i dS & i = 1,2,3 \\ \iint_{S_b} P\left(\mathbf{r}\times\mathbf{n}\right)_i \, dS & i = 4,5,6 \end{cases} \tag{31}$$

where S_b is the body surface at rest.

The total first order force and moment, which also include the hydrostatic term, can be expressed as:

$$\mathbf{F}^{(1)} = \mathbf{F}_{HS}^{(1)} + \mathbf{F}_{R}^{(1)} + \mathbf{F}_{EX}^{(1)} \tag{32}$$

where the subscripts HS , R , and EX represent the hydrostatic restoring force and moment, the force and moment from the radiation potential, and the wave exciting force and moment from the incident and diffraction potentials, respectively.

The first order hydrostatic restoring forces and moments $\mathbf{F}_{HS}^{(1)}$ are induced by the variations of hydrostatic pressure on the structure because of the motion of the floating structure, and it can be defined as:

$$\mathbf{F}_{HS}^{(1)} = -\mathbf{K}\left\{\zeta^{(1)}\right\} \tag{33}$$

where symbols $\zeta^{(1)}$ and $\mathbf{K}$ represent the first order motion of the floating structure and the hydrostatic restoring stiffness, respectively.

The first order force and moment acting on the floating structure induced by radiation potential $\mathbf{F}_{R}^{(1)}$ can be expressed as:

$$\mathbf{F}_{R}^{(1)} = \mathrm{Re}\left(\left[\mathbf{f}\right]\left\{\zeta^{(1)}\right\}\right) \tag{34}$$

where

$$\mathbf{f} = f_{ij} = -\rho \iint_{S_b} \frac{\partial \phi_i}{\partial n} \phi_j dS \qquad i, j = 1, 2, ..., 6 \tag{35}$$

and the frequency-dependent variable f_{ij} is the complex variable, which is divided into real and imaginary parts and can be written as:

$$f_{ij} = -\omega^2 M_{ij}^a - i\omega C_{ij} \tag{36}$$

Thus, the force and moment from the radiation potential can be expressed as (Bae, 2013):

$$\mathbf{F}_R^{(1)} = \mathrm{Re}\left(\left[\mathbf{M}^a \right] \left\{ \ddot{\zeta}^{(1)} \right\} + \left[\mathbf{C} \right] \left\{ \dot{\zeta}^{(1)} \right\} \right) \tag{37}$$

where $\mathbf{M}^a$ and $\mathbf{C}$ denote the added mass coefficients and radiation damping coefficients, respectively.

Moreover, the term $\mathbf{F}_{EX}^{(1)}$, which is the first order wave excitation forces and moments, is derived by incident and diffraction wave potentials and can be defined as:

$$\mathbf{F}_{EX}^{(1)} = \mathrm{Re}\left\{ -\rho A e^{-i\omega t} \iint_{S_0} \left(\phi_I + \phi_D \right) \frac{\partial \phi_j}{\partial n} dS \right\} \qquad j = 1, 2, ..., 6 \tag{38}$$

The first order wave excitation forces and moments are proportional to wave amplitude and frequency dependent. The first order wave exciting force under unit wave amplitude is defined as the Linear Transfer Function (LTF), which shows the relationship between incident wave elevation and the first order diffraction forces on the floating structure (Bae, 2013).

Wave Loads in Time Domain

The first order wave forces are calculated at a specific wave frequency while the second order sum and different frequency forces are acquired from the interactions of bi-chromatic waves (Bae, 2013). The first and second order hydrodynamic forces and moments acting on a floating structure due to stationary Gaussian random sea in the time domain can be represented as a two-term Volterra series as (Ran, 2000):

$$\mathbf{F}^{(1)}(t)+\mathbf{F}^{(2)}(t)=\int_{-\infty}^{\infty}h_1(\tau)\eta(t-\tau)d\tau+\int_{-\infty}^{\infty}\int_{-\infty}^{\infty}h_2(\tau_1,\tau_2)\eta(t-\tau_1)\eta(t-\tau_2)d\tau_1 d\tau_2 \tag{39}$$

where $h_1(\tau)$ represents the linear impulse response function, $h_2(\tau_1,\tau_2)$ denotes the quadratic impulse response function, and $\eta(t)$ is the ambient wave free surface elevation at a reference location. The wave exciting forces, which come from incident and diffraction potentials, can be expressed as a form of the superposition of the N frequency components for unidirectional waves (Bae, 2013):

$$\mathbf{F}_I^{(1)}(t)=\mathrm{Re}\left[\sum_{i=1}^{N}A_i\mathbf{L}(\omega_i)e^{i\omega_i t}\right] \tag{40}$$

$$\mathbf{F}_I^{(2)}(t)=\mathrm{Re}\left[\sum_{j=1}^{N}\sum_{k=1}^{N}A_j A_k^{*}\mathbf{D}(\omega_j,-\omega_k)e^{i(\omega_j-\omega_k)t}+\sum_{j=1}^{N}\sum_{k=1}^{N}A_j A_k\mathbf{S}(\omega_j,\omega_k)e^{i(\omega_j+\omega_k)t}\right] \tag{41}$$

where a superscript * is the complex conjugate of a variable, $\mathbf{L}(\omega_i)$ denotes the linear force transfer functions (LTF), $\mathbf{S}(\omega_j,\omega_k)$ and $\mathbf{D}(\omega_j,-\omega_k)$ represent the sum and difference frequency quadratic force transfer functions (QTF), respectively.

The forces and moments from radiation potentials in the time domain can be expressed as:

$$\mathbf{F}_R(t) = -\mathbf{M}^a(\infty)\ddot{\zeta}(t) - \int_{-\infty}^{t} \mathbf{R}(t-\tau)\dot{\zeta}(\tau)\,d\tau \tag{42}$$

where $\mathbf{M}^a(\infty)$ denotes the added mass at infinite frequency, the convolution integral represents the memory effect of the wave forces on a structure prior to time t. $\mathbf{R}(t)$ is the retardation function, which is associated with the frequency-domain solution of the radiation problem as follows (Bae, 2013):

$$\mathbf{R}(t) = \frac{2}{\pi}\int_0^{\infty} C(\omega)\frac{\sin \omega t}{\omega}\,d\omega \tag{43}$$

where $C(\omega)$ is the radiation damping coefficient at a frequency ω. Also, $\mathbf{M}^a(\infty)$ can further be expressed as:

$$\mathbf{M}^a(\infty) = \mathbf{M}^a(\omega) - \int_0^{\infty} \mathbf{R}(t)\cos \omega t dt \tag{44}$$

where $\mathbf{M}^a(\omega)$ is the added mass at a frequency ω.

The total wave forces can be acquired by summation of each force component in the time domain as follows (Bae, 2013):

$$\mathbf{F}_{total}(t) = \mathbf{F}_I(t) + \mathbf{F}_R(t) \tag{45}$$

where $\mathbf{F}_{total}(t) = \mathbf{F}^{(1)}(t) + \mathbf{F}^{(2)}(t)$ is the total wave exciting force, $\mathbf{F}_I(t) = \mathbf{F}_I^{(1)}(t) + \mathbf{F}_I^{(2)}(t)$ is the summation of the Equations (40) and (41), and $\mathbf{F}_R(t)$ is the radiation force from the Equation (42).

Morison Equation

Morison equation (Morison et al., 1950) can be used to estimate the inertia and damping effects for slender, cylindrical structures because the viscous effect is dominant whereas the diffraction effect is ordinarily negligible. Morison equation represents that the wave load per unit length of the slender structure normal to the element section with a diameter D, which is small compared with the wavelength, is a summation of inertia, added mass and drag forces represented as follows (Bae, 2013):

$$F_m = C_m \rho \frac{\pi D^2}{4} \dot{u}_n - C_a \rho \frac{\pi D^2}{4} \ddot{\zeta}_n + \frac{1}{2} \rho C_D D_S \left(u_n - \dot{\zeta}_n \right) \left| u_n - \dot{\zeta}_n \right| \tag{46}$$

where F_m represents Morison force, $C_m = 1 + C_a$ is the inertia coefficient, C_a is the added mass coefficient, C_D is the drag coefficient, D_S is a breadth or a diameter of the floating structure, $\dot{u}_n$ and u_n are the acceleration and the velocity of a fluid particle normal to the floating structure, respectively, and $\ddot{\zeta}_n$ and $\dot{\zeta}_n$ respectively represent the normal acceleration and velocity of the structure. In the above Equation, the first term in the right-hand side is the inertia force, i.e., the Froude-Krylov force and the diffraction force, the second term is the inertia force induced by the added mass, and the last term is the drag force as a function of relative velocity between a floating structure and a fluid particle. The relative-velocity form indicates that the drag force contributes to not only the exciting force but also the damping force on the motion of a structure. In this study, the SR-WEC is slender, cylindrical structure; therefore, the viscous effects of the SR-WEC are estimated by Morison equation, which is combined with the potential forces to estimate the total wave force on the structure.

Time-Domain Solution of the Structure Motions

Based on the Cummins equation, the equations of motion for a floating structure with consideration of the hydrodynamic force in the time domain can be expressed by follows:

$$\left[\mathbf{M}+\mathbf{M}^{a}\left(\infty\right)\right]\ddot{\boldsymbol{\xi}}+\mathbf{K}\boldsymbol{\zeta}=\mathbf{F}_{I}\left(t\right)+\mathbf{F}_{C}\left(t,\dot{\boldsymbol{\xi}}\right)+\mathbf{F}_{m}\left(t,\boldsymbol{\zeta}\right) \tag{47}$$

where

$$\mathbf{F}_{C}\left(t,\dot{\zeta}\right)=-\int_{-\infty}^{t}\mathbf{R}\left(t-\tau\right)\dot{\zeta}d\tau \tag{48}$$

where $\mathbf{F}_{I}\left(t\right)$ is the first and second order wave exciting force, which is presented in Equations (40) and (41) and $\mathbf{F}_{m}\left(t,\zeta\right)$ denotes the nonlinear drag forces obtained by Morison equation given in Equation (46). Equation (47) only includes hydrodynamic forces on a structure, and other forces, e.g., forces generated by the mooring-line-structure interaction and a linear generator, are not included in the equation.

Time integration is completed by the second order Adams-Moulton method, which is an implicit integration scheme. However, since accelerations and velocities are unknown parameters, with the initial value assumption, the iterative procedure is usually required to get converged solution to solve the equations, which may increase computation time for a complex system. In this study, the Adams-Bashforth explicit scheme is further introduced and combined with the Adams-Moulton method so that the iterative procedure can be avoided during time integration.

Dynamics of Mooring Lines

Introduction

In this section, the dynamics of a mooring line is explained, which is based on a three-dimensional elastic rod theory suggested by Garrett (1982). The behaviors of a line and its extensible condition are derived, and derived equations are further formulated by the finite element method. The equation of motion is solved in general coordinate whose tangential direction follows the line profile; therefore, coordinate transformations, which increase computation time, are not required. Also, geometric nonlinearity is considered without specific assumptions associated with the shape or orientation of lines (Kim et al., 2005).

The SR-WEC maintains its location by a single point mooring (SPM) system. A slack mooring line can be modeled in this case without having high static tension. In this case, the mooring line is highly flexible, and prediction of the line's behavior is hard if a linear spring is used to model the mooring line. Therefore, the elastic theory is adopted for the simulation of line's dynamic behaviors in the time domain. It is noted that this theory can also be applied for risers and pipelines with reasonable bending stiffness, and the tunnel model, which is described in CHAPTER II, is also completed by the line theory explained in this section.

Theory of Rod

The behavior of a slender rod is described with respect to the location of the centerline of the rod. As shown in Figure 2, in order to define a space curve, a position vector $\mathbf{r}(s,t)$ is defined as a function of arc length s and time t. If an inextensible condition is applied to the rod, the arc length s is identical regardless of the deformed state. Therefore, the unit tangent vector to the space curve is $\mathbf{r}'$, the principal normal vector is directed along $\mathbf{r}''$, and bi-normal is directed along $\mathbf{r}'\times\mathbf{r}''$ where the prime symbol denotes the differentiation with respect to arc length (Garrett, 1982; Ran, 2000).

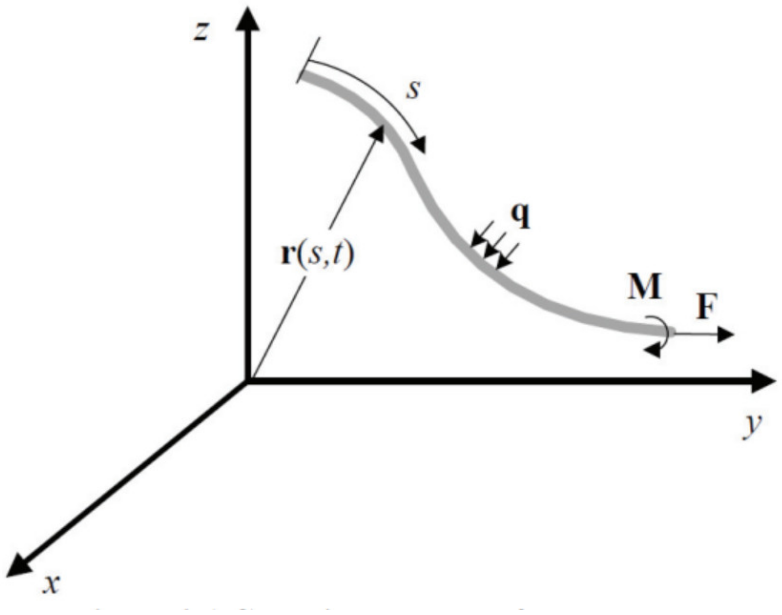

Figure 2. Coordinate system of the rod (Bae, 2013).

By using the equilibrium state of the linear force and moment at unit arc length of the slender rod, i.e., a segment of the rod, the equations of motion can be expressed as (Ran, 2000):

$$\mathbf{F}' + \mathbf{q} = \rho\ddot{\mathbf{r}} \tag{49}$$

$$\mathbf{M}' + \mathbf{r}' \times \mathbf{F} + \mathbf{m} = 0 \tag{50}$$

where $\mathbf{q}$ and $\mathbf{m}$ denote the applied force and moment per unit length, respectively, ρ represents the mass of the rod per unit length, $\mathbf{F}$ and $\mathbf{M}$ represent the resultant force and moment along the centerline, respectively, and the dot represents the differentiation with respect to time.

The bending moment proportionally increases with curvature if the principal stiffness along the rod is identical, and is directed along the bi-normal. In this condition, the resultant moment $\mathbf{M}$ can further be represented as:

$$\mathbf{M} = \mathbf{r}' \times EI\mathbf{r}'' + H\mathbf{r}' \tag{51}$$

where EI is the bending stiffness and H is the torque. Substituting the Equation (51) into (50), Equation (52) can be derived (Ran, 2000):

$$\mathbf{r}' \times \left[\left(EI\mathbf{r}'' \right)' + \mathbf{F} \right] + H'\mathbf{r}' + H\mathbf{r}'' + \mathbf{m} = 0 \tag{52}$$

and the scalar product of the Equation (52) with $\mathbf{r}'$ yields:

$$H' + \mathbf{m} \cdot \mathbf{r}' = 0 \tag{53}$$

In the case of mooring lines, there is no distributed torsional moment from the hydrodynamic force, i.e., $\mathbf{m} \cdot \mathbf{r}' = 0$ since they are usually circular shape. Moreover, the torque in mooring lines is normally small and negligible (Garrett, 1982; Ran, 2000). In

this case, H and $\mathbf{m}$ in Equation (52) are assumed to be zero, and the Equation (52) is simplified as (Ran, 2000):

$$\mathbf{r}' \times \left[\left(EI\mathbf{r}'' \right)' + \mathbf{F} \right] = 0 \tag{54}$$

A scalar function $\lambda(s,t)$, which is also known as the Lagrange multiplier, is introduced to express the resultant force $\mathbf{F}$ as:

$$\mathbf{F} = -\left(EI\mathbf{r}'' \right)' + \lambda \mathbf{r}' \tag{55}$$

The scalar product can be defined from Equation (55) as:

$$\lambda = \mathbf{F} \cdot \mathbf{r}' - \left(EI\mathbf{r}'' \right)' \cdot \mathbf{r}' \tag{56}$$

or

$$\lambda = T - EI\kappa^2 \tag{57}$$

where T is the tension and κ is the curvature of the rod.

By combining Equation (55) with Equation (49), the equation of motion for the slender rod can be expressed as:

$$-\left(EI\mathbf{r}'' \right)'' + \left(\lambda \mathbf{r}' \right)' + \mathbf{q} = \rho \ddot{\mathbf{r}} \tag{58}$$

Moreover, if the inextensible condition is assumed, $\mathbf{r}$ has to satisfy the following relationship (Ran, 2000):

$$\mathbf{r}' \cdot \mathbf{r}' = 1 \tag{59}$$

If the rod is regarded as extensible, and the stretch is linear and small, the Equation (59) can be approximated by (Ran, 2000):

$$\frac{1}{2}\left(\mathbf{r}'\cdot\mathbf{r}'-1\right)=\frac{T}{AE}\approx\frac{\lambda}{AE} \tag{60}$$

Equation (58) for the equation of motion of the slender rod and Equation (59) or (60) for the extensible condition, with not only initial and boundary conditions but also the applied force $\mathbf{q}$, are sufficient to determine both the position vector $\mathbf{r}(s,t)$ and the Lagrange multiplier $\lambda(s,t)$ (Ran, 2000). The applied force $\mathbf{q}$ on the rod can be divided into the hydrostatic force, the hydrodynamic force, and the gravity force of the rod, which can be expressed as:

$$\mathbf{q}=\mathbf{w}+\mathbf{F}^{s}+\mathbf{F}^{d} \tag{61}$$

where $\mathbf{w}$ denotes the weight of the rod per unit length, $\mathbf{F}^{s}$ is the hydrostatic force on the rod per unit length, and $\mathbf{F}^{d}$ is the hydrodynamic force on the rod per unit length. In particular, the hydrostatic force can be represented as:

$$\mathbf{F}^{s}=\mathbf{B}-\left(\mathrm{P}\,\mathbf{r}'\right)' \tag{62}$$

where $\mathbf{B}$ is the buoyancy force on the rod per unit length, and P is hydrostatic pressure at a point $\mathbf{r}$ on the rod. The hydrodynamic force $\mathbf{F}^{d}$ is calculated by using the Morison equation as follows:

$$\begin{aligned}\mathbf{F}^{d}&=-C_{A}\ddot{\mathbf{r}}^{n}+C_{M}\dot{\mathbf{V}}^{n}+C_{D}\left|\mathbf{V}^{n}-\dot{\mathbf{r}}^{n}\right|\left(\mathbf{V}^{n}-\dot{\mathbf{r}}^{n}\right)\\&=-C_{A}\ddot{\mathbf{r}}^{n}+\overline{\mathbf{F}}^{d}\end{aligned} \tag{63}$$

where C_A is the added mass coefficient i.e., added mass/unit length, C_M is the inertia coefficient, i.e., inertia force per unit length per unit normal acceleration, and C_D is the drag coefficient, i.e., drag force per unit length per unit normal velocity, $\mathbf{V}^{n}$ and $\dot{\mathbf{V}}^{n}$

denote the velocity and acceleration of a fluid particle normal to the rod centerline, respectively. The velocity and acceleration of the fluid particle can be computed from the total velocity of the fluid particle and tangent vector of the rod as (Ran, 2000):

$$\mathbf{V}^n = \left(\mathbf{V} - \dot{\mathbf{r}}\right) - \left[\left(\mathbf{V} - \dot{\mathbf{r}}\right) \cdot \mathbf{r}'\right] \mathbf{r}' \tag{64}$$

$$\dot{\mathbf{V}}^n = \dot{\mathbf{V}} - \left(\dot{\mathbf{V}} \cdot \mathbf{r}'\right) \cdot \mathbf{r}' \tag{65}$$

where $\mathbf{V}$ and $\dot{\mathbf{V}}$ represent the velocity and acceleration of the fluid particle, respectively, at the centerline of the rod without disturbance by the existence of the rod. Besides, the velocity $\dot{\mathbf{r}}^n$ and acceleration $\ddot{\mathbf{r}}^n$ of the rod normal to the centerline of the rod can be calculated by:

$$\dot{\mathbf{r}}^n = \dot{\mathbf{r}} - \left(\dot{\mathbf{r}} \cdot \mathbf{r}'\right) \cdot \mathbf{r}' \tag{66}$$

$$\ddot{\mathbf{r}}^n = \ddot{\mathbf{r}} - \left(\ddot{\mathbf{r}} \cdot \mathbf{r}'\right) \cdot \mathbf{r}' \tag{67}$$

The equation of motion for the rod can be expressed by substituting Equations (61)-(63) into Equation (58):

$$\begin{aligned} -\left(EI\mathbf{r}''\right)'' + \left(\lambda \mathbf{r}'\right)' + \mathbf{w} + \mathbf{B} - \left(P\mathbf{r}'\right)' - C_A \ddot{\mathbf{r}}^n + \overline{\mathbf{F}}^d &= \rho \ddot{\mathbf{r}} \\ \rho \ddot{\mathbf{r}} + C_A \ddot{\mathbf{r}}^n + \left(EI\mathbf{r}''\right)'' - \left(\lambda \mathbf{r}'\right)' + \left(P\mathbf{r}'\right)' &= \mathbf{w} + \mathbf{B} + \overline{\mathbf{F}}^d \\ \rho \ddot{\mathbf{r}} + C_A \ddot{\mathbf{r}}^n + \left(EI\mathbf{r}''\right)'' - \left(\overline{\lambda} \mathbf{r}'\right)' &= \overline{\mathbf{w}} + \overline{\mathbf{F}}^d \end{aligned} \tag{68}$$

where

$$\overline{\lambda} = \overline{T} - EI\kappa^2 \tag{69}$$

$$\overline{\mathbf{w}} = \mathbf{w} + \mathbf{B} \tag{70}$$

$$\overline{T} = T + P \tag{71}$$

$\bar{T}$ is the effective tension in the rod, and $\bar{\mathbf{w}}$ is the effective weight also known as the wet weight of the rod. The equation (68) combined with the stretching condition presented in Equation (60) are the governing equations for dynamic simulation of the slender rod.

Finite Element Model of Rod

The governing equations are further formulated by the Galerkin finite element method as (Garrett, 1982; Ran et al., 1999):

$$-\rho\ddot{r}_i - C_A\ddot{r}_i^n - \left(EIr_i''\right)'' + \left(\bar{\lambda}r_i'\right)' + \bar{w}_i + \bar{F}_i^d = 0 \tag{72}$$

$$\frac{1}{2}\left(r_n'r_n' - 1\right) - \frac{\lambda}{AE} = 0 \tag{73}$$

The position vector $r_i(s,t)$ and Lagrange multiplier $\lambda(s,t)$ for a single element of the length L are expressed as follows:

$$r_i(s,t) = A_l(s)U_{il}(t) \tag{74}$$

$$\lambda(s,t) = P_m(s)\lambda_m(t) \tag{75}$$

where A_m and P_n are shape functions defined on the interval $0 \le s \le L$. The weak forms of the governing equations are generated by using the Galerkin method and integration by parts:

$$\begin{aligned}\int_0^L \left[A_l\left(\rho\ddot{r}_i + C_A\ddot{r}_i^n\right) + EIA_l''r_i'' + \bar{\lambda}A_l'r_i' - A_l\left(\bar{w}_i + \bar{F}_i^d\right)\right]ds \\ = EIr_i''A_l'\Big|_0^L + \left[\bar{\lambda}r_i' - \left(EIr_i''\right)'\right]A_l\Big|_0^L\end{aligned} \tag{76}$$

$$\int_0^L P_m \left\{ \frac{1}{2}\left(r_n' \cdot r_n' - 1 \right) - \frac{\lambda}{AE} \right\} ds = 0 \tag{77}$$

where the first and second terms of the right-hand side in Equation (76) are related to moment and force at the boundary. Cubic and quadratic shape functions, i.e., A_l and P_m, which are continuous on the element, are defined for the position vector and Lagrange multiplier, respectively:

$$\begin{aligned}
A_1 &= 1 - 3\xi^2 + 2\xi^3 \\
A_2 &= L\left(\xi - 2\xi^2 + \xi^3 \right) \\
A_3 &= 3\xi^2 - 2\xi^3 \\
A_4 &= L\left(-\xi^2 + \xi^3 \right) \\
P_1 &= 1 - 3\xi + 2\xi^2 \\
P_2 &= 4\xi\left(1 - \xi \right) \\
P_3 &= \xi\left(2\xi - 1 \right)
\end{aligned} \tag{78}$$

where $\xi = s / L$.

The position vector, tangent of the position vector, and Lagrange multiplier are chosen to be continuous at the node between the neighboring elements. Therefore, the parameters U_{il} and λ_m can be written as:

$$\begin{aligned}
&U_{i1} = r_i\left(0,t\right), \qquad U_{i2} = r_i'\left(0,t\right), \\
&U_{i3} = r_i\left(L,t\right), \qquad U_{i4} = r_i'\left(L,t\right), \\
&\lambda_1 = \lambda\left(0,t\right), \qquad \lambda_2 = \lambda\left(L/2,t\right), \quad \lambda_3 = \lambda\left(L,t\right)
\end{aligned} \tag{79}$$

The position and its tangent vectors are obtained at both ends of the element while the Lagrange multiplier is computed at both ends and the middle point of the element. The

final finite element formulation of the governing equation for the 3-dimensional problem is presented in Equation (80).

$$\left(M_{ijlk}+M^{a}_{ijlk}\right)\ddot{U}_{jk}+\left(K^{1}_{ijlk}+\lambda_{n}K^{2}_{nijlk}\right)U_{jk}=F_{il} \tag{80}$$

Subscripts i and j are 1-3 for the 3-dimensional problem, and subscripts l, k, s, and t are 1-4 in Equation 80. In Equations (80)-(85), the general mass, the added mass, the general stiffness from the bending stiffness and rod tension, and external force matrices are defined with Kronecker Delta function δ_{ij}:

$$M_{ijlk}=\int_{0}^{L}\rho A_{l}A_{k}\delta_{ij}ds \tag{81}$$

$$M^{a}_{ijlk}=C_{A}\left[\int_{0}^{L}A_{l}A_{k}\delta_{ij}ds-\left(\int_{0}^{L}A_{l}A_{k}A'_{s}A'_{t}ds\right)U_{it}U_{js}\right] \tag{82}$$

$$K^{1}_{ijlk}=\int_{0}^{L}EIA''_{l}A''_{k}\delta_{ij}ds \tag{83}$$

$$K^{2}_{nijlk}=\int_{0}^{L}P_{n}A'_{l}A'_{k}\delta_{ij}ds \tag{84}$$

$$F_{il}=\int_{0}^{L}\left(\overline{w}_{i}+\overline{F}^{d}_{i}\right)A_{l}ds \tag{85}$$

In addition, the stretching condition can be formulated as given in Equation (77):

$$G_{m}=A_{mil}U_{kl}U_{ki}-B_{m}-C_{mt}\lambda_{t}=0 \tag{86}$$

where

$$A_{mil}=\frac{1}{2}\int_{0}^{L}P_{m}A_{i}'A_{l}'ds \tag{87}$$

$$B_m = \frac{1}{2}\int_0^L P_m ds \tag{88}$$

$$C_{mt} = \frac{1}{AE}\int_0^L P_m P_t ds \tag{89}$$

In the finite element formulations, 15 equations which are 6 equations for displacement vectors, 6 equations for tangential vectors, and 3 equations for Lagrange multiplier, are defined at each rod element for the 3-dimensional problem. The variables U_{jk} and λ_n constructs a kind of displacement vector $\mathbf{y}$ as:

$$\mathbf{y}^T = \{U_{11}, U_{12}, U_{21}, U_{22}, U_{31}, U_{32}, \lambda_1, \lambda_2, U_{13}, U_{14}, U_{23}, U_{24}, U_{33}, U_{34}, \lambda_3\}$$

(90)

Similarly, the force vector $\mathbf{F}$ is also defined as:

$$\mathbf{F}^T = \{R_{11}, R_{12}, R_{21}, R_{22}, R_{31}, R_{32}, -G_1, -G_2, R_{13}, R_{14}, R_{23}, R_{24}, R_{33}, R_{34}, -G_3\} \tag{91}$$

From the right-hand side of the Equation (76), the force vector can be expressed as:

$$\mathbf{F}^r = \begin{bmatrix} -\bar{\lambda} r_i' + \left(EIr_i'' \right)' \Big|_{s=0,i=1} \\ -EIr_i'' \Big|_{s=0,i=1} \\ -\bar{\lambda} r_i' + \left(EIr_i'' \right)' \Big|_{s=0,i=2} \\ -EIr_i'' \Big|_{s=0,i=2} \\ -\bar{\lambda} r_i' + \left(EIr_i'' \right)' \Big|_{s=0,i=3} \\ -EIr_i'' \Big|_{s=0,i=3} \\ 0 \\ 0 \\ \bar{\lambda} r_i' - \left(EIr_i'' \right)' \Big|_{s=L,i=1} \\ EIr_i'' \Big|_{s=L,i=1} \\ \bar{\lambda} r_i' - \left(EIr_i'' \right)' \Big|_{s=L,i=2} \\ EIr_i'' \Big|_{s=L,i=2} \\ \bar{\lambda} r_i' - \left(EIr_i'' \right)' \Big|_{s=L,i=3} \\ EIr_i'' \Big|_{s=L,i=3} \\ 0 \end{bmatrix} = \begin{bmatrix} -N_1^{[1]} \\ -L_1^{[1]} \\ -N_2^{[1]} \\ -L_2^{[1]} \\ -N_3^{[1]} \\ -L_3^{[1]} \\ 0 \\ 0 \\ N_1^{[2]} \\ L_1^{[2]} \\ N_2^{[2]} \\ L_2^{[2]} \\ N_3^{[2]} \\ L_3^{[2]} \\ 0 \end{bmatrix} \tag{92}$$

The Adams-Moulton implicit integration method combined with the Adam-Bashforth explicit scheme is used for the time-domain-integration method so that stable and time-efficient numerical integration can be done without iteration (Ran, 2000). This proposed integration method is identical for both floating structures and mooring lines.

Spring Coupling between the Structure and Mooring Lines

In this section, the dynamic model to couple a floating structure with mooring lines is reviewed. The structure-mooring-line interaction is realized by using linear and rotational springs. Linear springs are adopted to define the translational motions between a connection point of the floating structure and the top of the mooring line, and rotational springs define the rotations of the structure and the tangential direction of the line. It is recalled that the resultant forces and moments, which are given in Equation (76), are expressed in the vector form given in Equation (92). In the Equation (92), the resultant force vector is $\mathbf{N} = \{N_1, N_2, N_3\}^T$ and the generalized resultant moment vector is $\mathbf{L} = \{L_1, L_2, L_3\}^T$; thus, the nodal moment is $\mathbf{M} = \mathbf{L} \times \mathbf{r}'$ where $\mathbf{r}'$ is the unit tangent vector of the rod (Ran, 2000). The resultant force and moment at each node are canceled out except for the last node connected to the structure by springs. The resultant force and moment are the same as the force and moment applied to the last node due to the existence of the springs. Under the assumption of the small angular motions of the structure, the force acting on the last node induced by linear springs can be expressed as (Ran, 2000):

$$\mathbf{N} = \left[\mathbf{K}^L\right](\mathbf{X} + \mathbf{p} + \theta \times \mathbf{p} - \mathbf{r}) \tag{93}$$

where $\left[\mathbf{K}^L\right]$ is a 3×3 diagonal stiffness matrix of the linear spring with the nontrivial diagonal terms, K_1^L, K_2^L, and K_3^L represent the spring stiffness in x, y, and z directions, respectively, $\mathbf{X}$ is the translational motion of the structure at its origin of the body coordinate system, θ is the angular motion of the structure, $\mathbf{p}$ is the position vector of the point on the structure where the springs are connected in the body coordinate system, and $\mathbf{r}$ denotes the position of line's end node attached to the structure by springs. The opposite force and moment acting on the structure from linear springs are as follows:

$$\mathbf{F}^L = -\mathbf{N} \tag{94}$$

$$\mathbf{M}^L = \mathbf{p} \times -\mathbf{N} \tag{95}$$

Moreover, the moment applied on the end node induced by the rotational spring proportionally increases with the angle between the direction vector of the spring and the tangent of the line at a connecting point. By assuming small angular motions of the structure, the generalized resultant moment $\mathbf{L}$ can be expressed as (Ran, 2000):

$$\mathbf{L} = K^\theta \left(\mathbf{E} - \frac{\mathbf{r}'}{|\mathbf{r}|} \right) = K^\theta \left(\mathbf{e} + \theta \times \mathbf{e} - \frac{\mathbf{r}'}{|\mathbf{r}|} \right) \tag{96}$$

where $\mathbf{E}$ represents a unit vector in the direction of the spring reference, $\mathbf{e}$ is $\mathbf{E}$ in the body coordinate, and K^θ is the rotational spring coefficient. The term $\mathbf{r}'/|\mathbf{r}'|$ is utilized to ensure the unity of the tangent (Ran, 2000).

The force and moment acting on the structure from the springs are:

$$\mathbf{F}^\theta = 0 \tag{97}$$

$$\mathbf{M}^\theta = \mathbf{L} \times \mathbf{r}' \approx \mathbf{L} \times \mathbf{e} \tag{98}$$

In addition, with subscript notation, the connector force on the end node of the line can be expressed as:

$$N_i = K_i^L \left(X_i + p_i + \theta_j C_{ji} - r_i \right) \tag{99}$$

$$L_i = K^\theta \left(e_i + \theta_j D_{ji} - \frac{r_i'}{\left(r_k' r_k' \right)^{0.5}} \right) \tag{100}$$

In the same way, the force and moment acting on the structure can be rewritten as:

$$F_i = -N_i = -K_i^L \left(X_i + p_i + \theta_j C_{ji} - r_i \right) \tag{101}$$

$$M_i = M^L + M^\theta = N_k C_{ki} + L_k D_{ki} \tag{102}$$

where

$$\left[C \right] = \begin{bmatrix} 0 & -p_3 & p_2 \\ p_3 & 0 & -p_1 \\ -p_2 & p_1 & 0 \end{bmatrix} \tag{103}$$

$$\left[D \right] = \begin{bmatrix} 0 & -e_3 & e_2 \\ e_3 & 0 & -e_1 \\ -e_2 & e_1 & 0 \end{bmatrix} \tag{104}$$

Dynamics of Linear Generator

Dynamics of the linear generator is an essential consideration in coupling the two-body SR WEC. As described before, the coiled armature assembly is attached in the outer cylinder while the magnet assembly is located to the inner cylinder. The magnet assembly slides along the center rod, and the relative velocity between armature and magnet assemblies induces the electromotive force (EMF) E_b, which is a unit in voltage.

According to Faraday's law of induction, the induced EMF proportionally increases with a change in flux linkage λ_{fl} and can be calculated as (Park et al., 2013; Rhinefrank et al., 2006):

$$E_b = \frac{d\lambda_{fl}}{dt} = \frac{d\zeta_{rel}}{dt}\frac{d\lambda_{fl}}{d\zeta_{rel}} = \dot{\zeta}_{rel}\frac{d\lambda_{fl}}{d\zeta_{rel}} \tag{105}$$

where

$$\lambda_{fl} = N_c \phi_m \tag{106}$$

N_c is the number of turns, ϕ_m is magnetic flux, and $\dot{\zeta}_{rel}$ and ζ_{rel} are the relative velocity and motion of the magnet assembly relative to the armature assembly. The motional EMF, which can be the equivalent form of the induced EMF from Faraday's law of induction, can be also expressed as (Fazal et al., 2010; Miles, 2017; Parthasarathy, 2012; Prudell, 2007):

$$E_b = \oint \left(\mathbf{v} \times \mathbf{B}\right) \cdot d\mathbf{l} = -\dot{\zeta}_{rel} B_m l_c \tag{107}$$

where $B_m = B\sin\left(\pi\zeta_{rel} / \tau_p\right)$ is the magnetic flux, τ_p is the pole pitch, and l_c is a length of coil that receives influences by the magnetic field at each time. In addition, the LR circuit is generally used for the permanent magnet linear generator as represented in Figure 3. Based on the resistor-inductor (RL) circuit, the induced current is computed from Kirchhoff's loop rule, and an equivalent circuit can be expressed as (Rhinefrank et al., 2006):

$$E_b = \left(R_L + R_C\right) \cdot i_c + L_P \frac{di_c}{dt} \tag{108}$$

where R_L and R_C are load and phase resistances, respectively, i_c is the induced current, and L_P is the phase inductance. A first-order ordinary differential equation (ODE) should be solved, and the fourth-order Runge-Kutta method is used to compute the induced current.

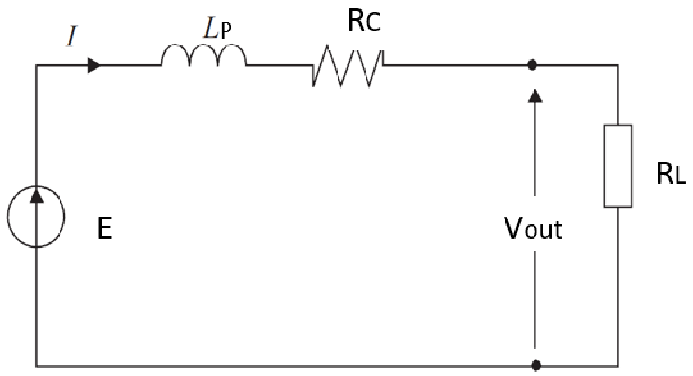

Figure 3. Equivalent circuit of the permanent magnet linear generator (Rhinefrank et al., 2006).

After calculating the induced current, the generator force can further be calculated by using the Lorentz-force equation. Electrons of electric current experience the magnetic force under the given magnetic field, which can be the interaction force between two bodies. The magnetic force acts both magnet and armature assemblies simultaneously. In particular, according to the Lorentz-force equation, the force on the coiled armature assembly in the sliding direction can be expressed as:

$$F_G = i_c \oint d\mathbf{l} \times \mathbf{B} = -B_m l_c i_c \tag{109}$$

According to Newton's 3rd law, the equal force acts on the magnet assembly in the opposite direction.

Coupled Dynamics of the Two-Body SR-WEC

In this section, the coupled dynamics of the two-body SR WEC is described. To couple the SR-WEC, the dynamic behavior of the magnet assembly should accurately be estimated. Figure 4 shows the sliding mechanism of the magnet assembly. As the inclination angle θ_s of the SR-WEC is higher than the designed minimum sliding angle, which is a function of a friction coefficient in the lubrication condition, the magnet assembly experiences the sliding force in the sliding direction F_S by gravity along the center rod, which can be expressed as:

$$F_S = m_i g\left(\sin\theta_s - \mu_f \cos\theta_s\right) \tag{110}$$

where μ_f is the friction coefficient, and m_i is mass of the magnet assembly.

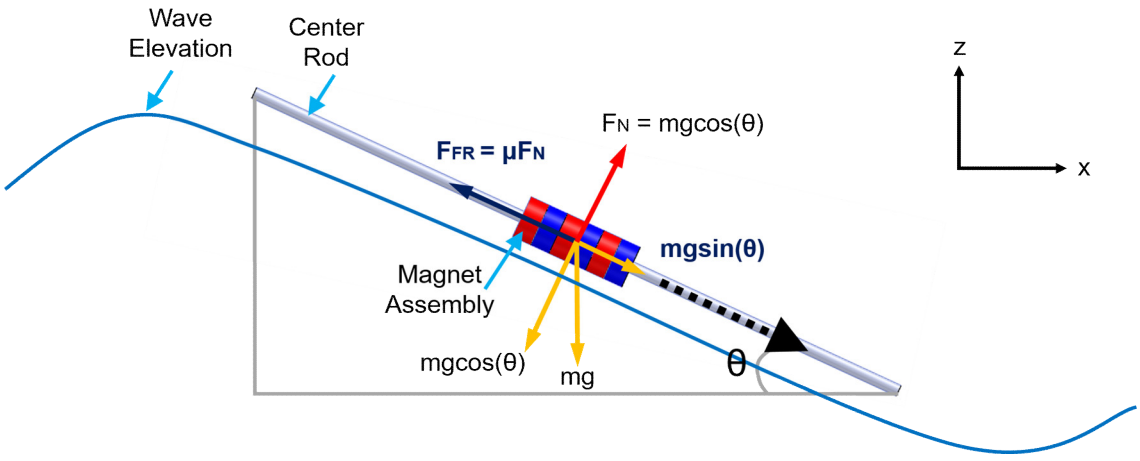

Figure 4. Sliding mechanism of the SR-WEC.

The dynamic equation of motion of the magnet assembly is solely solved in the sliding direction as:

$$m_i \ddot{\zeta}_{rel} = F_S(t) + F_G(t) \tag{111}$$

While 6 DOF motions are solved for the outer cylinder, the magnet assembly has only 1 DOF in the sliding direction. Moreover, the 1 DOF is defined in the body-fixed coordinate system located to the center of gravity of the outer cylinder. Since the coordinate center of the magnet assembly continuously moves with respect to the global coordinate system, because of motions of the outer cylinder, the non-inertia reference frame, i.e., the accelerated coordinate system is introduced to always keep the coordinate center in the center of gravity of the outer cylinder. The 1 DOF motion is, therefore, a motion of the magnet assembly relative to the body-fixed coordinate system of the outer cylinder in the sliding direction. In Equation (111), acceleration is also the relative acceleration with the same reason. In this coordinate system, the inertial forces, which is also knowns as the fictitious forces, should be added in the Equation (111) as external force terms. The inertial force is a function of the mass of the magnet assembly and acceleration of the outer cylinder. Therefore, the sliding force can further be modified. In this simulation, since the wave direction is parallel to the longitudinal direction of the SR-WEC as shown in Figure 4, sway and yaw motions are generally small; therefore, inertia forces from these motions are neglected.

$$\begin{aligned} F_S(t) = {} & m_i \left(g \sin\zeta_5 + \ddot{\zeta}_3 \sin\zeta_5 - \ddot{\zeta}_1 \cos\zeta_5 \right) \\ & - \operatorname{sgn}\left(\dot{\zeta}_{rel} \right) \mu m_i \left(g \cos\zeta_5 + \ddot{\zeta}_3 \cos\zeta_5 + \ddot{\zeta}_1 \sin\zeta_5 \right) \end{aligned} \tag{112}$$

In Equation (111), the equation of motion of the magnet assembly does not consider the contact mechanism between both bodies. To realize contact mechanism at both ends, conservation of momentum with consideration of the partially elastic condition

is used to calculate the displacement and velocity of the magnet assembly in the sliding direction when the magnet assembly contacts with the outer cylinder at both ends. A general form of the conservation of momentum and the coefficient of restitution are described as:

$$m_a v_{a1} + m_b v_{b1} = m_a v_{a2} + m_b v_{b2} \tag{113}$$

$$C_R = \frac{v_{b2} - v_{a2}}{v_{a1} - v_{b1}} \tag{114}$$

where v_a and v_b are velocities of the objects #1 and #2, m_a and m_b are masses of object #1 and #2, and C_R is the coefficient of restitution. By combining the above equations. The velocity of object #1 after the collision can be derived as:

$$v_{a2} = \frac{m_a v_{a1} + m_b v_{b1} + m_b C_R \left(v_{b1} - v_{a1} \right)}{m_a + m_b} \tag{115}$$

In the case of SR-WEC, because the mass of the outer cylinder is much heavier than that of the magnet assembly, terms related to the mass of the magnet assembly in Equation (115) can be neglected. Moreover, with the same reason, the influences of the collision on the dynamic motion of outer cylinder are minimal, which means that velocity of the outer cylinder is assumed to be identical before and after the collision. Furthermore, as mentioned before, the coordinate center is continuously changed, and the non-inertia frame of reference is applied to calculate the motion of the magnet assembly. In this case, the velocity of the outer cylinder with respect to the coordinate center of the magnet assembly is always zero, and the motion of the magnet assembly becomes the relative

motion. Based on the above considerations, the Equation (115) can further be simplified by changing the coefficients in terms of variables of SR-WEC system as:

$$\dot{\zeta}_{rel2} = C_{R'}\dot{\zeta}_{rel1} \tag{116}$$

where $C_{R'} = -C_R = \dot{\zeta}_{rel2} / \dot{\zeta}_{rel1}$.

When the magnet assembly does not contact with both ends, Equation (111) is used to solve the dynamic equation of motion. As the magnet assembly is about to contact with one of the ends within the designated time step, conservation of momentum with consideration of the coefficient of restitution is utilized define the displacement and velocity of the magnet assembly.

After considering every force components, the dynamic equation of motion of the SR-WEC, i.e., the outer cylinder based on the Cummins equation with a matrix size of 6 ×6 can be represented as:

$$\left[\mathbf{M} + \mathbf{M}^a(\infty)\right]\ddot{\boldsymbol{\xi}} + \mathbf{C}\dot{\boldsymbol{\xi}} + \mathbf{K}\boldsymbol{\zeta} = \mathbf{F}_I(t) + \mathbf{F}_C(t) + \mathbf{F}_m(t) + \mathbf{F}_G(t) + \mathbf{F}_{ml}(t) \tag{117}$$

where $\mathbf{F}_{ml}(t)$ is the mooring force, and $\mathbf{C}$ is the damping matrix. The moment acting on the outer cylinder due to the gravitational force of the magnet assembly is not considered due to the significant mass difference between two bodies. Also, a damping matrix is used to realize the damping effect of rotational motions of the outer cylinder, and the critical damping ratio estimates coefficients. The drag force term in Morison equation is utilized for the damping effect of translational motions assuming that drag forces are acting on the center of gravity.

Verification of Numerical Simulation

The verifications of the developed simulation program are summarized in this section. First of all, the sliding mechanism of the magnet assembly is verified between numerical results and results produced by 2 DOF actuator tests. In addition, the verification of the generator dynamic is performed by comparing the results of numerical simulations with experimental results conducted by Prudell et al. (2010).

Comparison with 2 DOF Actuator Test

Figure 5 shows the test setup of 2 DOF actuator test, and Table 2 presents the dimension and mass of cylinders. An acrylic hollow tube is used for inner and outer cylinders while stainless steel is used for the center rod. A linear ball bearing (produced by Thomson) is mounted in an inside of the inner cylinder to maximize the sliding performance. At both ends, Styrofoam is installed to minimize the impact force. There are two actuators (ZABER A-LST type) installed in both ends of the outer cylinder to simulate the heave-pitch coupled motion of the outer cylinder. As the outer cylinder moves with actuators, the inner cylinder slides along a center rod.

First, the minimum sliding angle of the inner cylinder is checked. After increasing the angle of the outer cylinder from 0.2 degrees with an interval of 0.05 degrees, the minimum sliding angle is around 0.45-0.5 degrees. A contact mechanism at the end is also identified at different inclination angles. Figures 6-7 show displacement comparison of the inner cylinder at sliding angles of 2 and 3 degrees. The minimum sliding angle is set to be 0.5 degrees by previous sliding tests, and a static friction coefficient μ_{fs} is calculated

accordingly. The dynamic friction coefficient is generally smaller than the static friction coefficient, and the dynamic friction coefficient is assumed to be 75 % of the static friction coefficient to match numerical results with experimental ones. The coefficient of restitution is mainly checked in this test. As shown in these figures, the displacements of the inner cylinder calculated by numerical simulations are well agreed with experiments, and the coefficients of restitution to match results with experiments of 2- and 3-degree cases are 0.35 and 0.39, respectively.

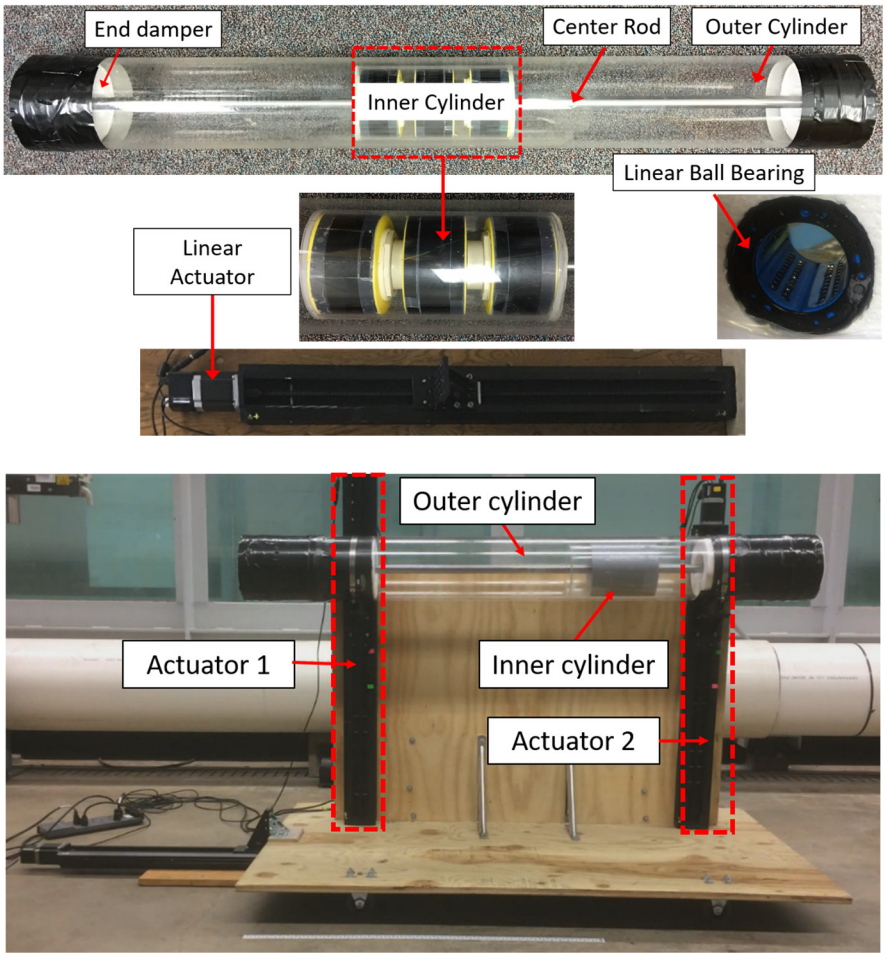

Figure 5. Test setup of 2 DOF actuator tests.

Table 2. WEC mass and dimension.

Item		Value
Outer cylinder	Length	1.52 m
	Mass	9.51 kg
Inner cylinder	Length	0.31 m
	Mass	2.1 kg
Center rod	Diameter	0.025 m

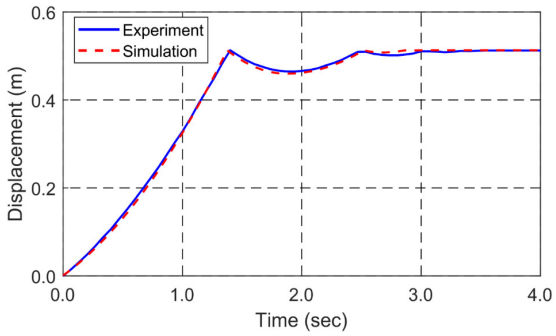

Figure 6. Time-history comparison of displacement of the inner cylinder at the sliding angle of 2 degrees.

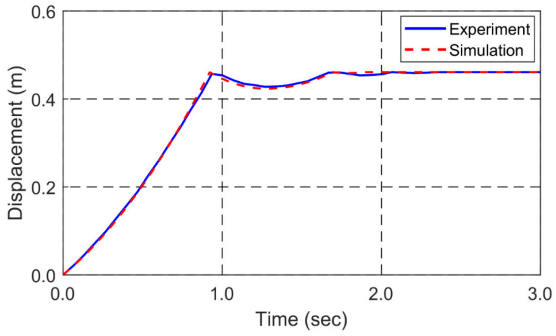

Figure 7. Time-history comparison of displacement of the inner cylinder at the sliding angle of 3 degrees.

Results of the heave-pitch coupled actuator test are further compared with previously obtained parameters. Figure 8 shows the time-history of input pitch and heave motions, and Figures 9-10 show the time-history comparison of displacement and velocity

of the inner cylinder for the heave-pitch coupled test. Same time histories of heave and pitch motions are inputted in the numerical simulation. The coefficient of restitution is set to be 0.39 in this case, which is obtained by previous tests. As shown in Figure 9, even if there is a small phase lag, displacement is well matched with the given coefficient of restitution. Also, the maximum velocity in the numerical simulation is approximately 10 % higher than the experiment. The general trend is, however, well matched.

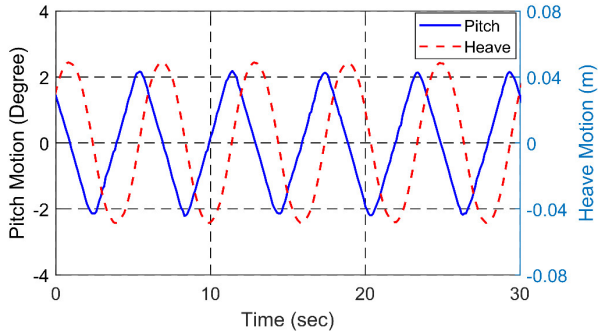

Figure 8. Time-history of input pitch and heave motions.

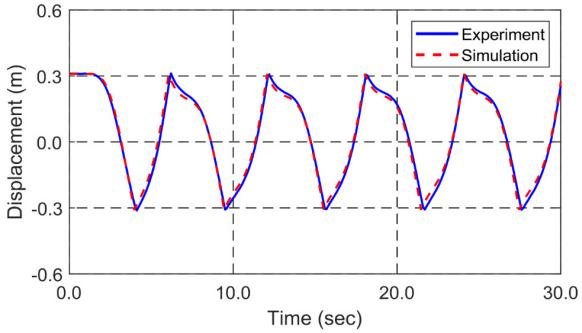

Figure 9. Time-history comparison of displacement of the inner cylinder for the heave-pitch coupled test.

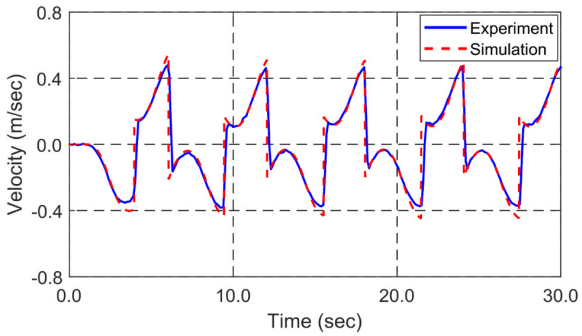

Figure 10. Time-history comparison of the velocity of the inner cylinder for the heave-pitch coupled test.

Validation of Generator dynamics

Generator dynamics is verified by comparing numerical results with experimental data produced by Prudell et al. (2010). They considered a heave-type WEC, which consists of inner and outer buoys. Armature and magnet assemblies are installed at inner and outer buoys, respectively. 960 neodymium iron boron (NdFeB) rare earth magnets were used to construct magnet assembly, and the three-phase Y connection was designed in the armature assembly. A single point mooring system was connected to the inner cylinder for a station-keeping purpose. Their target power output was 1 kW under the summer ocean condition in Newport, OR, USA, which has a significant wave height of 1.5 m. Major parameters to calculate power output are given in Table 3.

In their power output calculation, dynamics of floating bodies was not solved by assuming that the inner buoy is stationary while the outer buoy follows wave elevation. Therefore, the heave motion of the outer buoy determines relative motion between two buoys. The mooring-line dynamics is also not solved. Eight different wave conditions are simulated for 900 sec, and power output results are compared with experiments. Figures

11-14 show the time histories of wave elevation, the EMF, the induced current, and power output obtained by a numerical simulation at the significant wave height H_s of 0.44 m, the zero crossing period T_z of 6.4 sec, and the load resistance R_L of 3.9 Ω. Compared with wave elevation, high-frequency oscillations occur for the EMF and the induced current; thus, the time step should be small enough for generator dynamics. A phase difference of 60 degrees for the three-phase system is also confirmed in time histories. As shown in Figure 14, efficiency can be calculated by dividing power input by power output and optimized by changing generator parameters. Table 4 presents the comparison results of power output in 8 different wave conditions. Wave height varies from 0.44 m to 3.04 m. Since the measured wave time histories were utilized for power output calculations in experiments, a direct comparison is unrealistic. However, the calculated average power output is generally well matched with experiments, and the maximum different is -5.3 % in the significant wave height of 3.04 m. Table 4 demonstrates that the developed generator scheme can further be applied for SR-WEC simulations.

Table 3. Major parameters to calculate power output (Prudell et al., 2010).

Parameter	Value	Units
Number of magnetic poles	4	-
Magnetic flux density	0.9037	T
Average circumference of the winding	1.81	m
Number of turns per slot	77	-
Reduction factor due to armature reduction	0.904	-
EMF magnitude at unit velocity	455.43	V
Phase resistance	4.58	Ω
Phase inductance	0.19	H

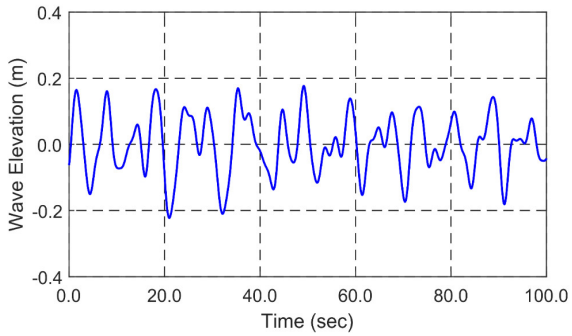

Figure 11. Time history of wave elevation for significant wave height of 0.44 m, zero crossing period of 6.4 sec, and a load resistance of 3.9 Ω.

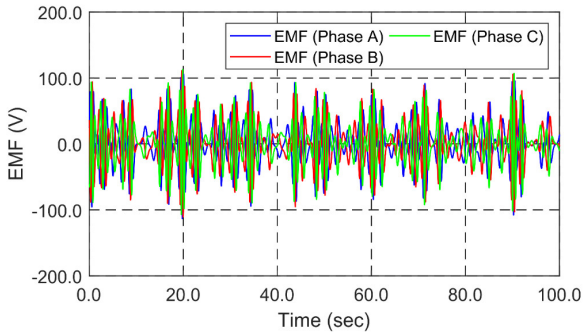

Figure 12. Time histories of EMF for significant wave height of 0.44 m, zero crossing period of 6.4 sec, and a load resistance of 3.9 Ω.

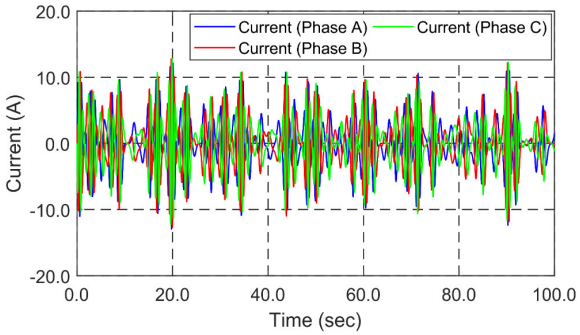

Figure 13. Time histories of induced current for significant wave height of 0.44 m, zero crossing period of 6.4 sec, and a load resistance of 3.9 Ω.

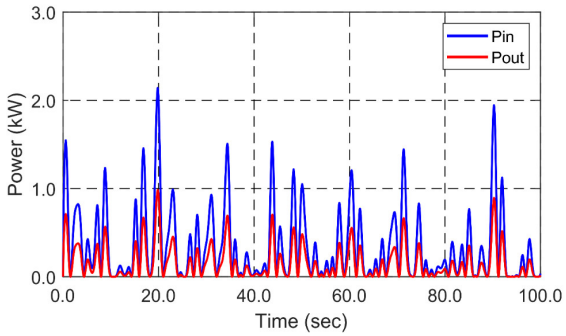

Figure 14. Time history of power input and output for significant wave height of 0.44m, zero crossing period of 6.4 sec, and a load resistance of 3.9 Ω.

Table 4. Comparison of average power output in different sea conditions (Prudell et al., 2010).

Sea condition	H_s	T_z	R_L	Average power output (experiment)	Average power output (Numerical)	Difference
1	0.44 m	6.4 sec	3.9 Ω	0.177 kW	0.179 kW	1.2 %
2	0.64 m	6.2 sec	4.1 Ω	0.368 kW	0.387 kW	5.2 %
3	1.02 m	7.6 sec	4.3 Ω	0.669 kW	0.658 kW	-1.7 %
4	1.25 m	7.6 sec	4.4 Ω	0.920 kW	0.917 kW	-0.3 %
5	1.52 m	7.6 sec	4.7 Ω	1.237 kW	1.224 kW	-1.1 %
6	2.03 m	7.6 sec	5.2 Ω	1.758 kW	1.734 kW	-1.4 %
7	2.54 m	7.6 sec	5.8 Ω	2.207 kW	2.141 kW	-3.1 %
8	3.04 m	7.6 sec	6.4 Ω	2.587 kW	2.455 kW	-5.3 %

Configuration of the Designed SR-WEC

The basic configuration of the SR-WEC, which is shown in Figure 15, is described in this section. A length and a diameter of the outer cylinder of the SR-WEC is 8.0 m and 2.6 m, respectively. To match the pitch natural frequency of the structure to the wave-frequency band, heavy ring masses are implemented at both ends of the outer shell, which significantly increases the pitch inertia of moment.

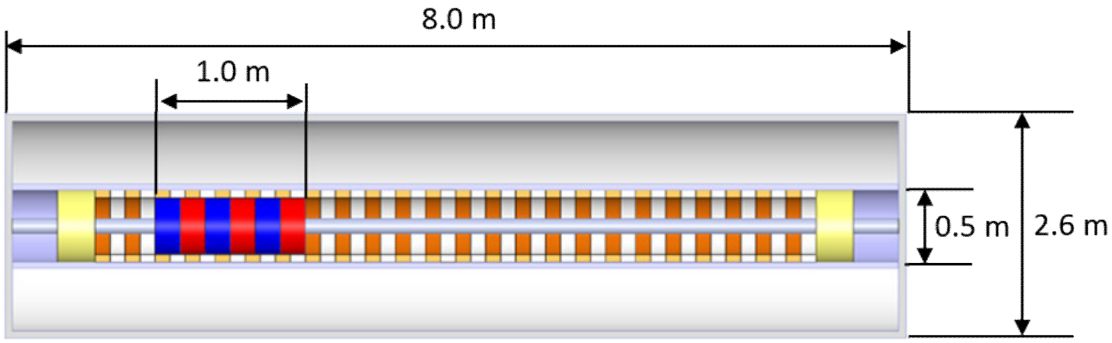

Figure 15. 2D view of the SR-WEC.

The armature assembly mainly consists of the lamination steels made of silicon steel and the coil made of copper. These components are located inside the hollow tube with a diameter of 0.5 m. The magnet assembly, which is a combination of neodymium iron boron (NdFeB) rare earth magnets and the lamination steels, has a length of 1.0 m and slides along the strong center rod that can fully support the magnet assembly. The generator design can be completed by using the electromagnetic simulation program such as ANSYS Maxwell. In this study, the magnitude of EMF and the load resistance are determined through the parametric study, and other vital parameters, e.g., phase resistance

and inductance are adopted from previous research (Prudell, 2007). After the parametric study, the system can be designed and optimized by means of the electromagnetic simulation program. As mentioned before, at both ends, rubber springs and dampers are installed to mitigate the strong hitting force by the magnet assembly.

A SPM is implemented, which is connected to the middle bottom point (0, 0, -1.3m) of the SR-WEC, as represented in Figure 16. The x, y, and z coordinates of the anchor location are -75 m, 0 m, and -50. Since the SPM is used for the minimum station keeping, a slack mooring made by a studlink chain is designed, which has a length of 100 m and a bar diameter of 1.5 cm. The primary parameters of the SR-WEC including the generator and the mooring line are presented in Table 5.

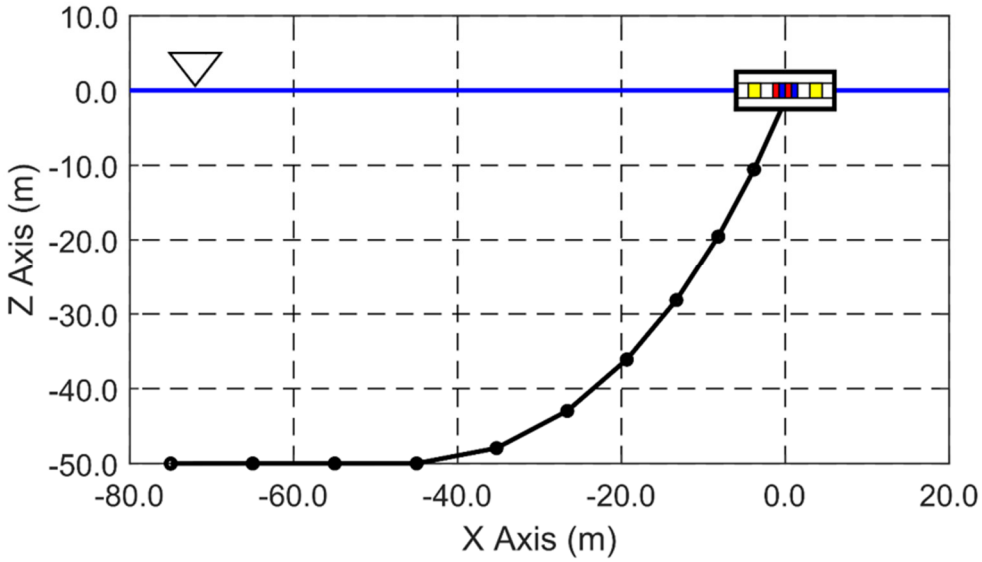

Figure 16. 2D view of the initial configuration of the SR-WEC with a mooring line.

Table 5. The basic configuration of the SR WEC.

Component	Item	Value	Unit
Buoyancy can (equipped with armature assembly)	Length	8.0	m
	Diameter	2.6	m
	Mass	21,365	kg
Magnet assembly (NdFeB magnet with lamination steels)	Length	1.0	m
	Diameter	0.38	m
	Mass	403	kg
	Air gap	0.5	cm
Generator	Phase resistance	4.58	Ω
	Phase inductance	190	mH
	Pole pitch	72	mm
	Coil pitch	72	mm
Mooring line (Studlink Chain)	Nominal diameter	1.5	cm
	Length	100	m
	Mass/unit length	4.9	kg/m

Frequency-Domain Analysis for Wave-Force Estimation

A frequency-domain analysis is firstly done to compute the hydrodynamic forces on the outer cylinder. A widely used diffraction-radiation program, WAMIT, is used to estimate the added mass, the radiation damping, and hydrostatic restoring coefficients, and the 1st order wave forces and moments. The x, y, and z coordinates of a center of gravity are 0 m, 0 m, and 0 m, and a half volume of the cylinder is submerged. As shown in Figure 17, the submerged surface panels are modeled, which are used for the WAMIT. Convergence tests are carried out to check whether the hydrodynamic-force estimation is reasonable. 330-panel, 468-panel, 1029-panel models are utilized for comparison. Thirty wave frequencies are selected from 0.1 rad/s to 5.0 rad/s, and a wave direction is parallel to the longitudinal direction of the SR-WEC, i.e., the positive x-axis (0 degrees). Since the mass of the magnet assembly is much smaller compared with the entire SR-WEC, it is assumed that the mass moments of inertia do not change regardless of the magnet-assembly location sliding along the center rod. Therefore, the mass matrix for the WAMIT input is based on the configuration of the entire SR-WEC including the magnet assembly, assuming that the magnet assembly is located to the center of gravity of the SR-WEC. The SolidWorks program is utilized to the estimation of the mass matrix as presented in Table 6.

Figures 18-20 show the undamped surge, heave, and pitch response amplitude operators (RAOs). Other RAOs are much smaller compared with these three RAOs due to the input wave direction. Convergence tests prove that even if the panel number increase by about three times, their responses are almost identical. In this case, the 468-panel model

is further employed for time-domain analyses. In the cases of surge and heave motions, RAOs are large at low-frequency ranges. The pitch natural frequency is 1.65 rad/s, and highly amplified pitch motions are expected even in mild sea conditions; therefore, high sliding performance can be achieved in mild wave conditions. Besides, computed added masses and moment, and radiation damping coefficients for 3 DOF motions are represented in Figures 21-22.

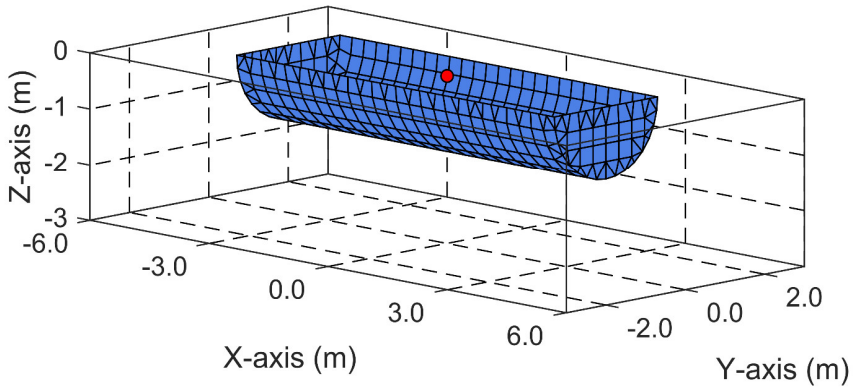

Figure 17. Panel model with 468 panels.

Table 6. Mass matrix of the Entire SR-WEC.

Component	Value	Unit
M (1,1)	21,768	kg
M (2, 2)	21,768	kg
M (3, 3)	21,768	kg
M (4, 4)	18,343	kg-m²
M (5, 5)	273,508	Kg-m²
M (6, 6)	273,508	Kg-m²

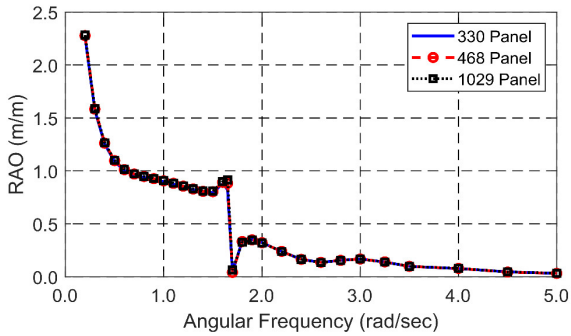

Figure 18. Surge RAO.

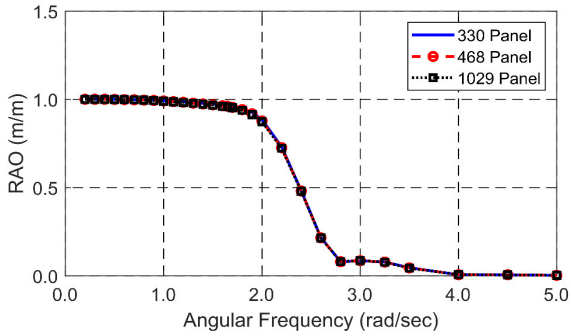

Figure 19. Heave RAO.

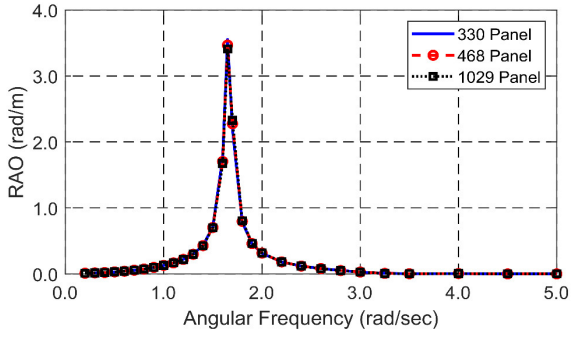

Figure 20. Pitch RAO.

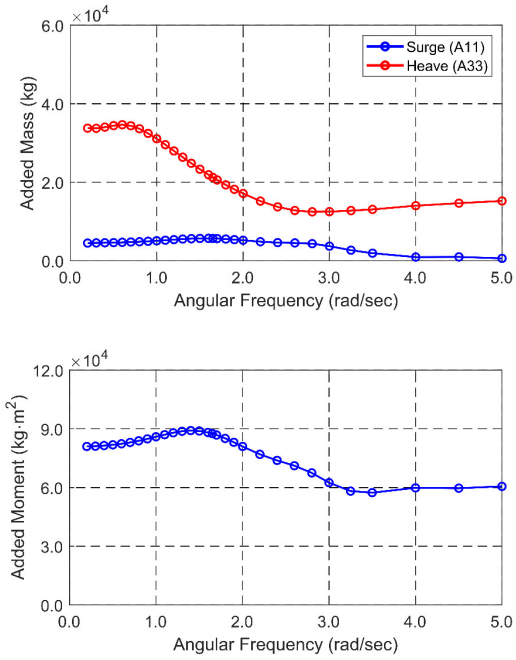

Figure 21. Added masses and moment for surge/heave (top) and pitch (bottom) motions.

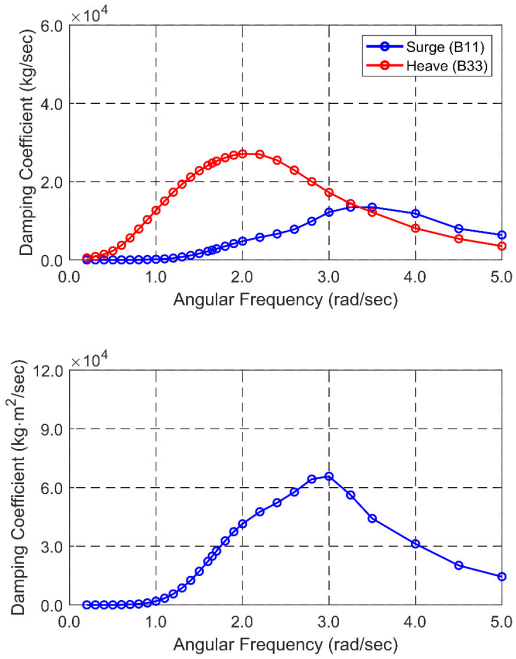

Figure 22. Radiation damping coefficients for surge/heave (top) and pitch (bottom) motions.

Parametric Study of the SR-WEC in the Time-Domain

The results of time-domain analyses are systematically explained in this section. Time-domain analyses are further carried out. Added masses and moments, radiation damping coefficients, hydrostatic restoring coefficients, and wave forces and moments, which are calculated in the frequency domain, are also utilized for time-domain analyses. A SPM is modeled in the time-domain and coupled with the SR-WEC using linear springs.

Consideration of Viscous Drag Force

In the time-domain, viscous drag forces and moments are additionally considered on the outer cylinder of the SR-WEC. For translational motions, drag forces are added by the drag-force term in Morison equation. A drag coefficient of 0.5 is utilized for the surge and heave motions of the WEC assuming that the drag force acts on the center of gravity. Besides, viscous damping moments are calculated for rotational motions, and critical damping ratio of 0.03 is assumed in this study.

In the case of the mooring line, drag and inertia forces are considered based on the Morison equation. Inertia and drag coefficients are 2.0 and 2.6, respectively. A nominal diameter of 1.5 cm is used for the drag force calculation while the inertia force calculation is based on an equivalent diameter of 2.8 cm.

Environmental Condition and Parameters for the Parametric Study

Several parameters are selected for the parametric study. In the case of the wave condition, the significant wave height varies from 1.0 m to 3.5 m, and the peak period is

from 5.0 sec to 11.0 sec. JONSWAP wave spectrum is chosen for wave-elevation generations. Time histories of wave elevation are generated by superposition of 100 regular wave components, and randomly perturbed intervals are used to avoid signal repetition. A 15-minute simulation, which excludes the ramping time, is conducted for each case with a time step of 0.005 sec. This small time is to accurately estimate EMF, the induced current, and power input and output due to high-frequency variations of these parameters. The ramping time is 300 sec to prevent divergence of the results during time integration by slowly increasing wave elevation. Since it is hard to estimate the enhancement parameter in JONSWAP wave spectrum, a suggested equation is used for the estimation of the enhancement parameter, which is a function of significant wave height and peak period (Veritas, 2000).

$$\begin{aligned} &\gamma = 5.0 && for \quad T_P / \sqrt{H_S} \le 3.6 \\ &\gamma = \exp\left(5.75 - 1.15 T_P / \sqrt{H_S}\right) && for \quad 3.6 \le T_P / \sqrt{H_S} \le 5.0 \\ &\gamma = 1.0 && for \quad 5.0 \le T_P / \sqrt{H_S} \end{aligned}$$

(118)

The magnitude of EMF, which is the same as the magnitude of the magnetic force, and the load resistance are first chosen as initial parameters for optimization of PTO damping. Moreover, a sliding length of the magnet assembly, the coefficient of restitution at both ends, and the mass of the magnet assembly are chosen for optimization of the SR-WEC to maximize power output. After each parametric study, the optimized parameter is continuous to be used as the fixed parameter for next parametric study.

Effect of the Load Resistance and the Magnitude of EMF

The load resistance and magnitude of EMF (i.e., the magnitude of the magnetic force) are firstly considered to optimize PTO damping of the SR-WEC. The magnetic force acting on both the magnet and armature assemblies is a function of current as given in Equation (109), and current is also related to the magnitude of EMF, phase/load resistance, and phase inductance. Whereas the phase resistance and the phase inductance are generally difficult to adjust a lot, the magnitude of EMF and the load resistance can be changed relatively easily. For this reason, the magnitude of EMF and the load resistance are, therefore, selected as initial parameters for PTO-damping optimization.

It is required to identify the relationship between these parameters and power output. As the load resistance is too small at the fixed magnitude of EMF, the high magnetic force is generated even at a low speed of the magnet assembly. The high magnetic force acts as the significant damping force on the magnet assembly and the outer cylinder, reducing not only sliding performance but also power input and output. On the other hands, the high load resistance induces low power input due to system characteristics of the linear generator; therefore, generated power output is also low. Similarly, as the magnitude of EMF is too small, high power output cannot be generated at the fixed load resistance even if the sliding performance is excellent. On the other hand, power output is also low at the large magnitude of EMF since it induces larger damping force even at the low velocity of the magnet assembly. Therefore, both excellent sliding performance and high power output with small PTO damping can be obtained by the parametric study. In this parametric study, the load resistance varies from 10 Ω to 200 Ω with a 10-Ω interval

while the magnitude of the magnetic force is from 100 T·m to 500 T·m. 3 wave-height conditions, which are summarized in Table 7, are used for optimization. These wave conditions are also utilized for other parametric studies.

Table 7. Wave conditions for the parametric study.

Significant wave Height (H_S)	Peak Period (T_P)	Enhancement parameter (γ)
1.0	5.0	1.0
2.0	6.0	2.4
3.0	7.0	3.0

Figures 23-27 show the time histories of displacement and velocity of the magnet assembly in the sliding direction, EMF, the induced current, and power output at the different load resistances and identical significant wave height of 2.0 m. In this simulation, the sliding length, the coefficient of restitution obtained by previous experiments, and the mass of the magnet assembly are fixed to be 3 m, 0.38, and 403 kg, respectively. Moreover, the magnitude of EMF is set to be 300 T·m. As shown in Figure 23, at different load resistances, the sliding performance is somewhat different, and the maximum sliding performance can be obtained at the load resistance of 80 Ω, which can be further confirmed in the time history of the velocity of the magnet assembly as shown in Figure 24. As shown in Figure 25, since the velocity of the magnet assembly directly influences on EMF, the EMF is highest at the load resistance of 80 Ω. Even though the EMF at the load resistance of 80 Ω is much higher than other conditions, the induced current is a little smaller than other cases as represented in Figure 26, which consequently contributes to a reduction of

the magnetic force resulting in the maximized motion of the magnet assembly. Due to the fact that the maximized EMF is obtained at the load resistance of 80 Ω while the induced currents are similar, the power output is, therefore, highest at that load resistance as shown in Figure 27.

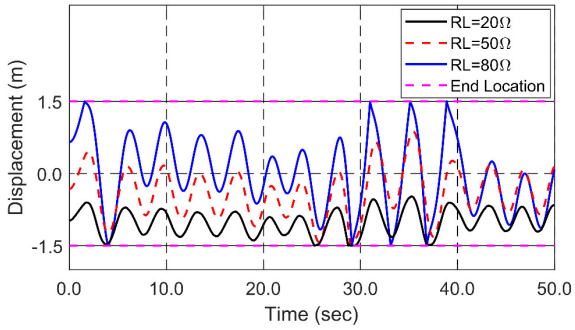

Figure 23. Time histories of displacement of the magnet assembly at different load resistances and the identical wave condition (H_S = 2.0, T_P = 6.0).

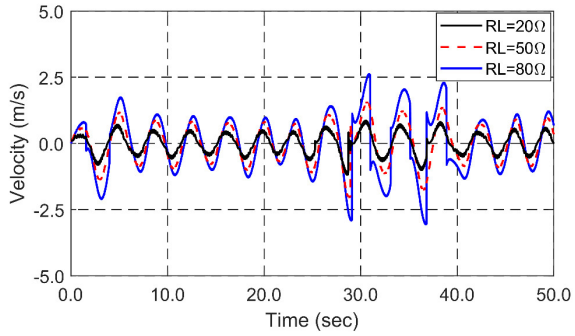

Figure 24. Time histories of the velocity of the magnet assembly at different load resistances and the identical wave condition (H_S = 2.0, T_P = 6.0).

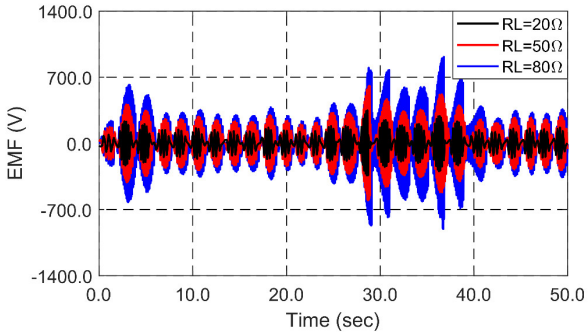

Figure 25. Time histories of EMF at different load resistances and the identical wave condition (H_S = 2.0, T_P = 6.0).

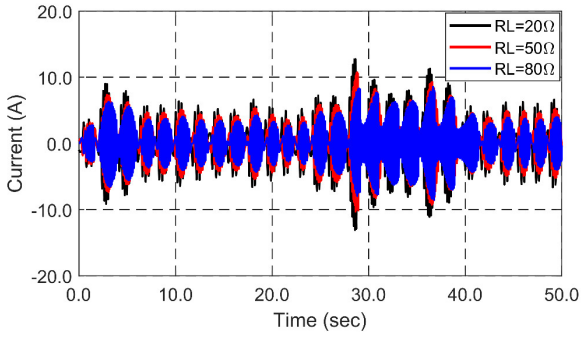

Figure 26. Time histories of the induced current at different load resistances and the identical wave condition (H_S = 2.0, T_P = 6.0).

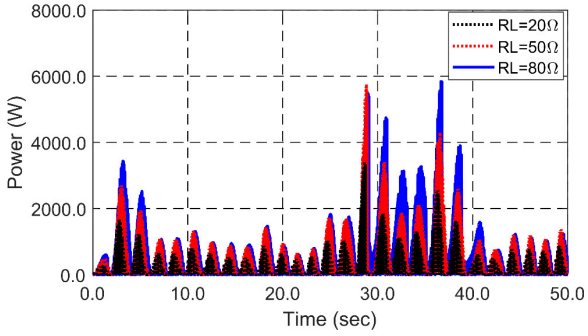

Figure 27. Time histories of power output at different load resistances and the identical wave condition (H_S = 2.0, T_P = 6.0).

Figure 28 summarizes average power output at different wave conditions. The optimum load resistance is the same regardless of the wave condition. Besides, as the magnitude of the magnetic force increases, the optimum load resistance to produce the highest power output also increases. As the magnitude of the magnetic force is higher than 300 T·m, there is no significant difference in the average power output. After averaging power output of three wave conditions, the maximum average power output can be obtained at the magnitude of 300 T·m and the load resistance of 80 Ω. As a result, these optimized values are fixed for the next parametric study.

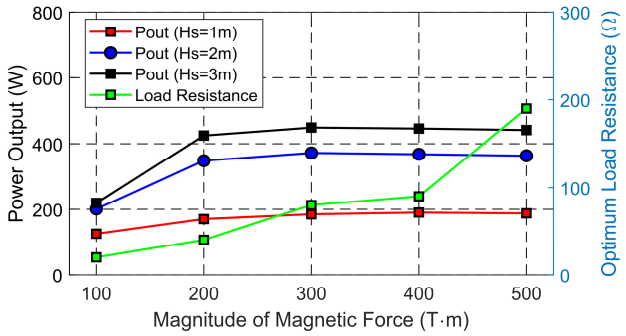

Figure 28. Average power outputs and optimum load resistances at different load resistances and wave conditions.

Figures 29-31 show the time history of the surge, heave and pitch motions of the SR-WEC. Since the direction of the magnetic force, which is same as the sliding direction of the magnet assembly, is close to the surge motion, there are minor differences in the surge motion due to the magnetic force. There are no significant differences in heave motions with the same reason. These are almost no effects of the magnetic force and the mooring tension on the pitch motion of the SR-WEC. Due to the existence of the mooring

line, the slow-varying surge motion can be also found in the time history. Figure 32 shows the time history of the mooring tension. Since the slack SPM is modeled, the mooring tension is not significant, and the maximum tension is much smaller than the minimum breaking load (MBL) of 263.8 kN for R4 chains (Veritas, 2009) with consideration of the safety factor (SF) of 1.67 (API, 1996). In storm-induced survival condition, there should be a safety plan to avoid the high mooring tension.

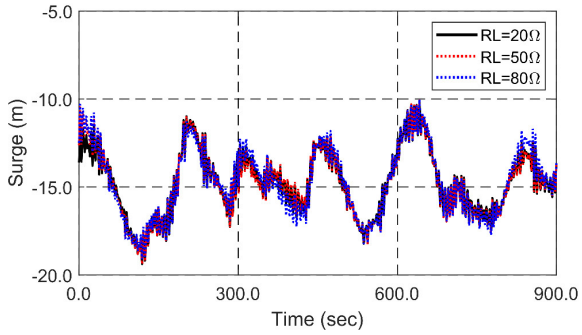

Figure 29. Time histories of surge at different load resistances and the identical wave condition (H_S = 2.0, T_P = 6.0).

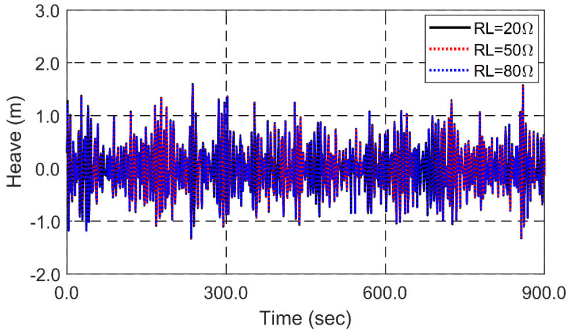

Figure 30. Time histories of the heave motion at different load resistances and the identical wave condition (H_S = 2.0, T_P = 6.0).

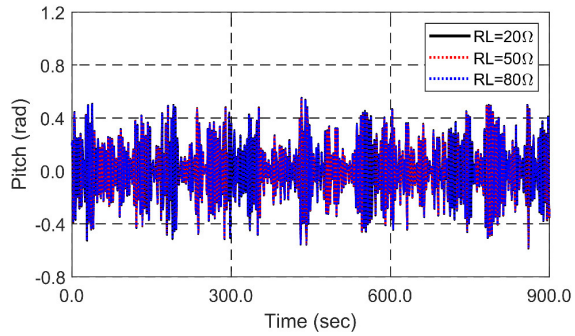

Figure 31. Time histories of the pitch motion at different load resistances and the identical wave condition (H_S = 2.0, T_P = 6.0).

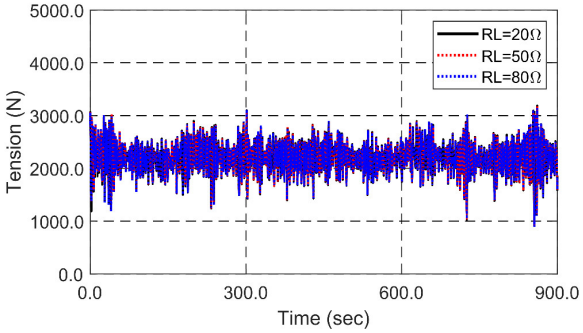

Figure 32. Time histories of the mooring tension at different load resistances and the identical wave condition (H_S = 2.0, T_P = 6.0).

Effect of the Sliding Length

The sliding length of the magnet assembly can improve the sliding performance. The sliding length, which is defined as the length between two ends minus the length of the magnet assembly, for the parametric study varies from 2.0 m to 6.0 m with an interval of 1.0 m.

Figures 33-35 show the time histories of not only displacement and velocity of the magnet assembly in the sliding direction but also power output at the different sliding lengths and significant wave height of 2.0 m. As the magnet assembly does not contact

with the end locations, the motion trend is almost the same, which can be confirmed in the time histories of velocity as shown in Figure 34. As the magnet assembly contacts with the end locations, the trends are significantly different. As the length of the magnet assembly is 2.0 m, the magnet assembly stops even before it reaches the maximum velocity. On the other hands, the long travel length of 6.0 m also leads to low sliding performance since the magnet assembly gradually stops after the pitch motions of the SR-WEC turn to another direction and miss the best chance to well slide at the maximum pitch motion. In this case, the optimum length of the magnet assembly is 4.0 m to provide the maximum power output as shown in Figure 35.

Figure 36 presents average power output at different lengths of the magnet assembly and wave conditions. The optimum length increases with increases in significant wave height and peak period. More considerable significant wave height induces greater pitch motions and increases the sliding performance. More substantial wave period also increases travel time. Thus, these factors increase the optimum sliding length as significant wave height and peak period increase. After obtaining average results in three wave conditions, the optimal sliding length is 4.0 m. For the next parametric study, the optimum sliding length is fixed to be 4.0 m.

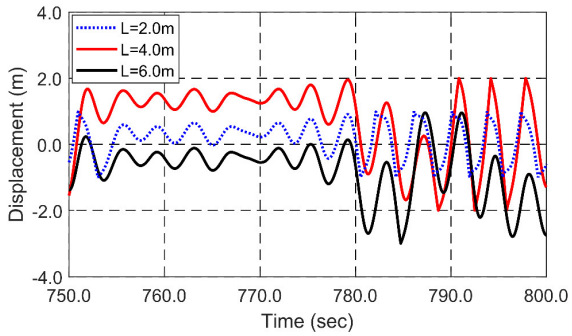

Figure 33. Time histories of displacement of the magnet assembly at different lengths of the magnet assembly and the identical wave condition (H_S = 2.0, T_P = 6.0).

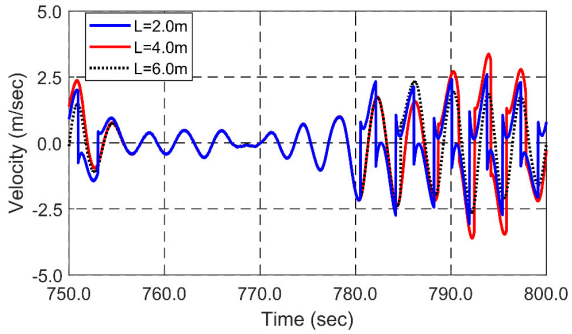

Figure 34. Time histories of the velocity of the magnet assembly at different lengths of the magnet assembly and the identical wave condition (H_S = 2.0, T_P = 6.0).

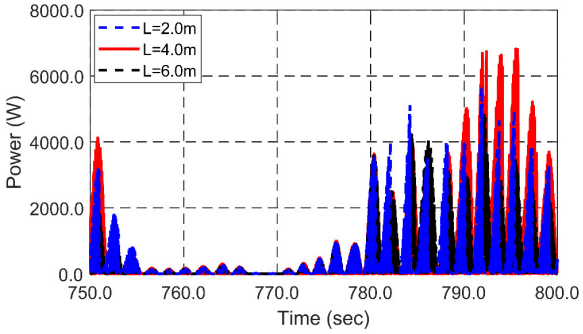

Figure 35. Time histories of power output at different lengths of the magnet assembly and the identical wave condition (H_S = 2.0, T_P = 6.0).

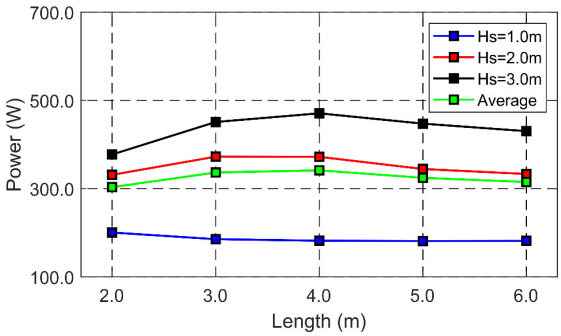

Figure 36. Average power outputs at different sliding lengths of the magnet assembly and wave conditions.

Effect of the Coefficient of Restitution

From previous parametric studies, it is proven that end locations can play an important role in improving the sliding performance as it is properly modeled. In this section, the effects of the coefficient of restitution are investigated. The selected coefficients of restitution are 0.01, 0.38, and 0.80. Figures 37-39 show the time histories of not only the displacement and velocity of the magnet assembly in the sliding direction but also power output at the different coefficients of restitution and identical significant wave height of 2.0 m. The same sliding performance is observed before the magnet assembly contacts with the end locations as shown in Figures 37-38. However, the sliding performance significantly improves as the coefficient of restitution increases from 0.01 to 0.8 after the magnet assembly contacts with the end locations. Figure 40 presents the average power output at different coefficients of restitution and wave conditions, and the above trends can further be observed. For the next parametric study, the coefficient of restitution is set to be 0.8, which provide the best performance. Feasibility of such a system with the high coefficients of restitution should be confirmed.

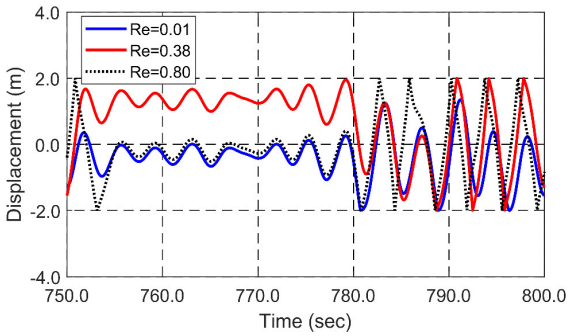

Figure 37. Time histories of displacement of the magnet assembly at different coefficients of restitution and the identical wave condition (H_S = 2.0, T_P = 6.0).

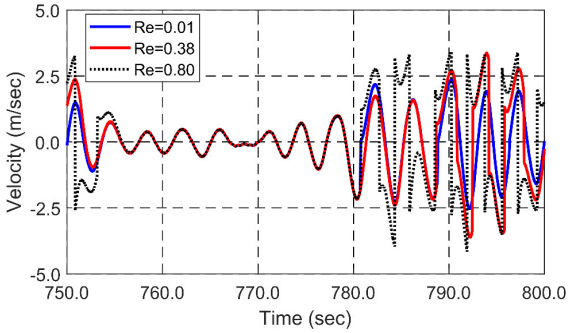

Figure 38. Time histories of the velocity of the magnet assembly at different coefficients of restitution and the identical wave condition (H_S = 2.0, T_P = 6.0).

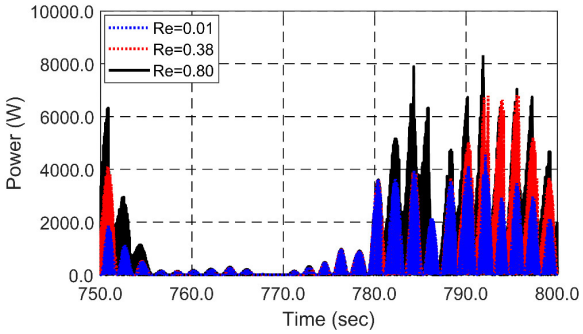

Figure 39. Time histories of power output at different coefficients of restitution and the identical wave condition (H_S = 2.0, T_P = 6.0).

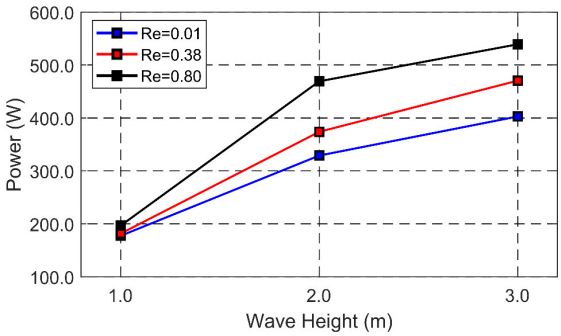

Figure 40. Average power output under different coefficients of restitution and wave conditions.

Effect of Mass of the Magnet Assembly

The mass of the magnet assembly can have a significant influence on the sliding performance since SR-WEC mainly takes advantage of the gravitational force of the magnet assembly, which means that the magnitude of the magnet assembly can be significant during the optimization process. Therefore, in this section, the effect of the magnet assembly's mass on the sliding performance is evaluated by changing the mass of the magnet assembly from 200 kg to 400 kg with a 100 kg interval.

Figures 41-43 show the time histories of not only displacement and velocity of the magnet assembly in the sliding direction but also power output at the different masses of the magnet assembly and identical significant wave height of 2.0 m. As shown in Figures 41-42, the higher mass of the magnet assembly results in the higher sliding performance. Notably, the sliding performance is significantly improved as the magnet assembly contacts with the end locations. This high sliding performance at the large mass results in high power output as shown in Figure 43. This phenomenon is further confirmed in the results of average power output as shown in Figure 44. At different wave conditions,

higher mass of the magnet assembly results in higher power output due to the same reason. As a result, the mass of the magnet assembly is fixed to be 400 kg, which provides the best performance. Feasibility of such a system with the heavy mass of the magnet assembly must be verified. In particular, the center rod should be strong enough to support the magnet assembly without bending and provide high fatigue life. Besides, the design of the end locations should be carefully completed to prevent fatigue and crack of these locations.

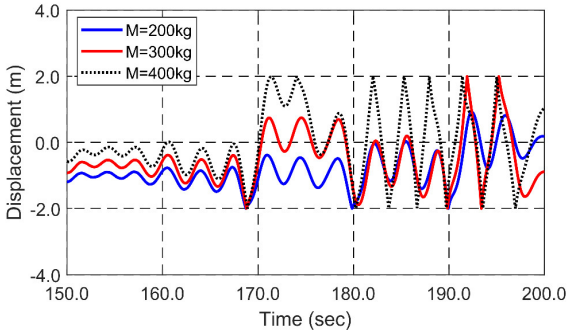

Figure 41. Time histories of displacement of the magnet assembly at different masses of the magnet assembly and the identical wave condition (H_S = 2.0, T_P = 6.0).

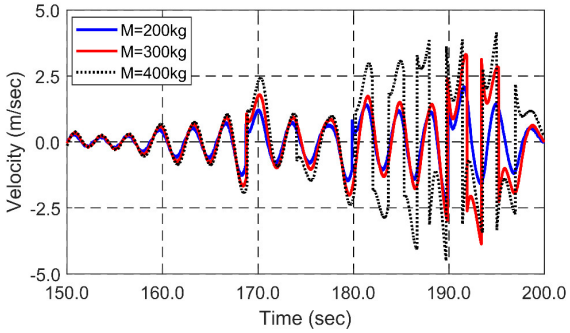

Figure 42. Time histories of the velocity of the magnet assembly at different masses of the magnet assembly and the identical wave condition (H_S = 2.0, T_P = 6.0).

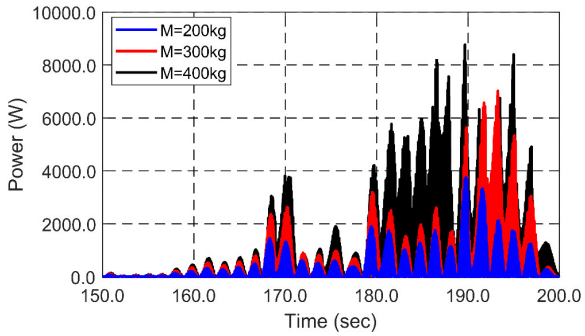

Figure 43. Time histories of power output at different masses of the magnet assembly and the identical wave condition (H_S = 2.0, T_P = 6.0).

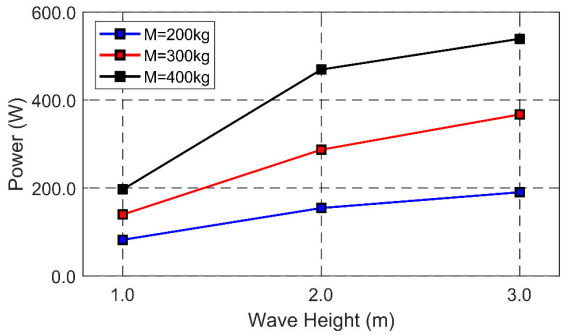

Figure 44. Average power output at different masses of the magnet assembly and wave conditions.

Power Output for Various Wave Conditions

From the previous parametric study, it is demonstrated that the load resistance, the magnitude of the magnetic force, the sliding length, the coefficient of restitution, and the mass of the magnet assembly have significant effects on the sliding performance of the magnet assembly and power output. Combining these parameters will eventually provide the maximum power output and good sliding performance. In this section, based on the best sliding condition, numerical results obtained by time-domain simulations at different significant wave heights and peak periods are analyzed. Simulation time for each case is

15 minutes. The load resistance, the magnitude of the magnetic force, the sliding length, the coefficient of restitution, and the mass of the magnet assembly are set to be 80 Ω, 300 T·m, 4.0 m, 0.8, and 400 kg, respectively. Figure 45 well summarizes the trends of the average power output at different significant wave heights from 1.0 m to 3.5 m and peak periods from 5.0 sec to 11.0 sec. Recall that the pitch natural frequency is 1.65 rad/s. In this case, large pitch motions usually occur at a low peak period. Also, it is also true that large wave height enables to large pitch motion under the identical peak period. Combining these two factors, the largest average power output occurs at a significant wave height of 3.5 m and peak period of 5.0 sec, and in this wave condition, the average power output is 1.31 kW. Even though the significant wave height is 3.5 m, the small power output of 0.14 kW is acquired at the peak period is 11.0 sec since the peak period is far away from the pitch natural frequency. In order to maximize power output, the pitch natural frequency can be rearranged, and a control system to adjust the natural frequency can be used such as the movable ring mass.

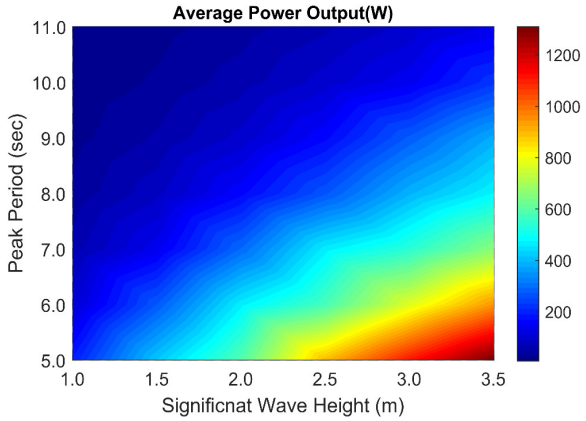

Figure 45. Average power output at different wave conditions.

CHAPTER III

GLOBAL-PERFORMANCE ANALYSIS OF A SUBMERGED FLOATING TUNNEL AND TUNNEL-MOORING-LINE-VEHICLE INTERACTION UNDER WAVE AND SEISMIC EXCITATIONS

Theory and Formulation of the Submerged Floating Tunnel for Global-Performance Analysis and Tunnel-Mooring-Line-Vehicle Coupled Analysis in the Time-Domain

Dynamic Model of the Submerged Floating Tunnel

In this section, the dynamic model of the SFT is explained with a simple example. Figure 46 shows the 3-dimensional example of the SFT model. Tunnel and mooring lines are modeled by line elements, and the rod theory described in Chapter I is utilized. A dummy rigid body is introduced to connect tunnel sections with mooring lines conveniently. The dummy rigid bodies are located wherever tunnel sections are needed to be connected with mooring lines, and their connection is realized by using linear and rotational springs with high stiffness values. As a result, their interaction forces and moments are transferred from the tunnel section to mooring lines or vice versa through the rigid body.

Figure 47 shows the coupled stiffness matrix based on a configuration presented in Figure 46 to create the SFT structure. In Figure 46, for example, each tunnel section and mooring line are assumed to have two elements. Then, in each line, matrix size will

be 23 × 23, i.e., 8 n +7, where n is element number. Moreover, the coupled stiffness matrix, which is expressed with green color in Figure 47, is positioned to couple tunnel sections with mooring lines through the rigid body.

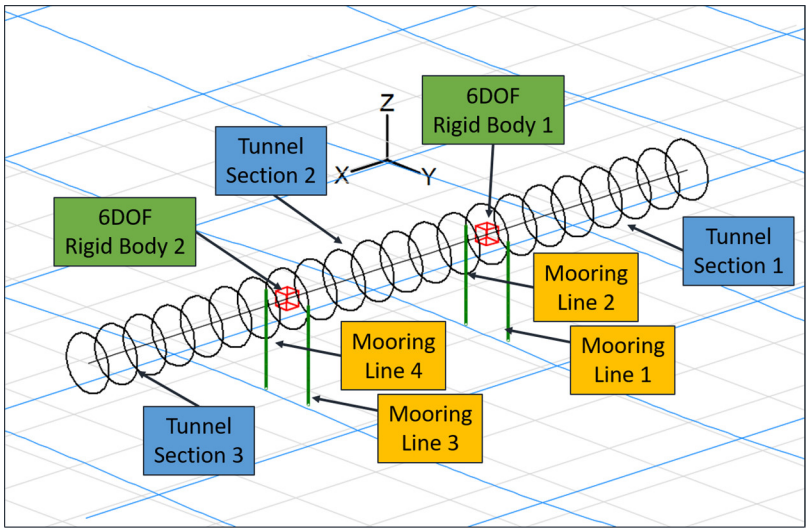

Figure 46. A 3-dimensional SFT model with three tunnel sections, four mooring lines, and two 6 DOF rigid bodies.

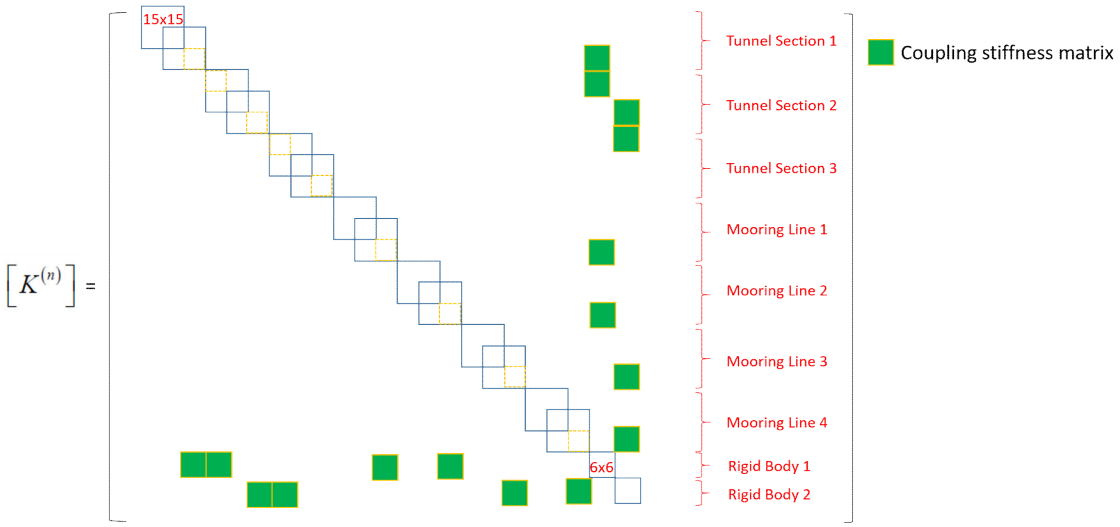

Figure 47. Coupled stiffness matrix for the example case (each line has two elements, which has a matrix size of 23 × 23).

Dynamic Model of a Vehicle Element

The rigid-body dynamic method is used to model a vehicle element (Xia and Zhang, 2005; Xia et al., 2017; ZHANG et al., 2010), and the vehicle model is coupled with the developed SFT model. Figure 48 shows the 2D drawings of the vehicle model used in this study. A vehicle element primarily consists of seven components, i.e., a car-body, two bogies, and four wheel-sets. The seven components are regarded as rigid bodies, and their elastic responses are neglected. All rigid bodies are connected by using linear springs and dampers. Each vehicle element passes through the tunnel at the same speed where their interaction in the surge direction, i.e., the vehicle-moving direction, is not considered. From the given design in Figure 48, a general form of the equations of motion for a vehicle element is expressed as:

$$\mathbf{M}_E\ddot{\mathbf{X}}_E + \mathbf{C}_E\dot{\mathbf{X}}_E + \mathbf{K}_E\mathbf{X}_E = \mathbf{F}_E \tag{119}$$

where a subscript E denotes the vehicle element, $\mathbf{M}$, $\mathbf{C}$, and $\mathbf{K}$ are mass, damping, and stiffness matrices, respectively, $\mathbf{F}$ is the external load vector, $\mathbf{X}$ is the displacement vector, and $\dot{\mathbf{X}}$ and $\ddot{\mathbf{X}}$ are the velocity and acceleration vectors. Since the surge motion of a vehicle is pre-defined by the vehicle speed, each car-body and bogie have 5 DOF. Moreover, each wheel-set has 3 DOF. The heave and roll motions of a wheel-set are assumed to be the same as that of the tunnel plus the track irregularity based on the corresponding assumption; thus, the sway motion is only solved for every wheel-set. As a

result, each vehicle element has 19 unknown DOF where other DOF are known values. A displacement vector to solve the dynamic equation is presented as:

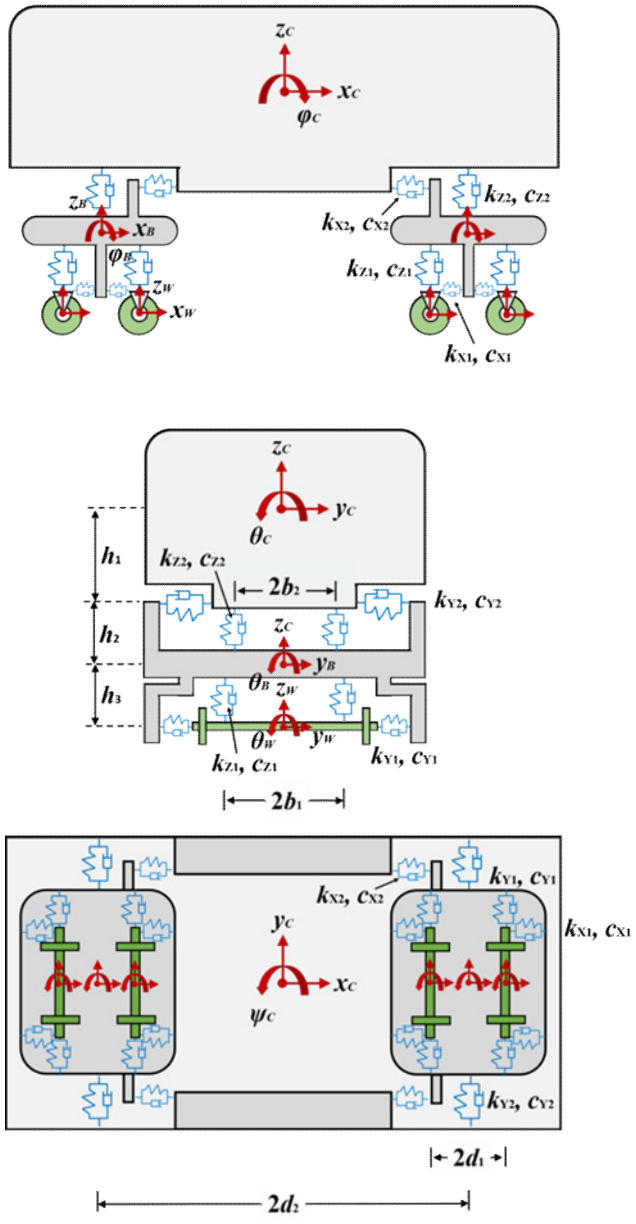

Figure 48. 2-dimensional drawing of the vehicle model using linear springs and dampers.

$$\mathbf{X}_E = \left[y_C,\ z_C,\ \theta_C,\ \varphi_C,\ \psi_C,\ y_{B1},\ z_{B1},\ \theta_{B1},\ \varphi_{B1},\ \psi_{B1},\right.$$
$$\left. y_{B2},\ z_{B2},\ \theta_{B2},\ \varphi_{B2},\ \psi_{B2},\ y_{W1},\ y_{W2},\ y_{W3},\ y_{W4} \right]^T \tag{120}$$

where subscripts, C, $B1$, and $B2$ represent car-body, front and rear bogies, $W1$ and $W2$ are wheel-sets connected to the front bogie, $W3$ and $W4$ are wheel-sets attached to the rear bogie, and y, z, θ, φ, and ψ represent sway, heave, roll, pitch, and yaw motions, respectively. Based on the given configuration in Figure 48, the governing equations of motion for a vehicle element can be derived as follows:

a. A car-body.

$$2k_{Y2}\left[\sum_{j=1}^{2}\left(y_{Bj} - h_2\theta_{Bj}\right) - 2y_C - 2h_1\theta_C\right] + 2c_{Y2}\left[\sum_{j=1}^{2}\left(\dot{y}_{Bj} - h_2\dot{\theta}_{Bj}\right) - 2\dot{y}_C - 2h_1\dot{\theta}_C\right] = m_C\ddot{y}_C \tag{121}$$

$$2k_{Z2}\left(\sum_{j=1}^{2} z_{Bj} - 2z_C\right) + 2c_{Z2}\left(\sum_{j=1}^{2}\dot{z}_{Bj} - 2\dot{z}_C\right) = m_C\ddot{z}_C \tag{122}$$

$$2k_{Y2}h_1\left[\sum_{j=1}^{2}\left(y_{Bj} - h_2\theta_{Bj}\right) - 2y_C - 2h_1\theta_C\right] + 2k_{Z2}b_2^2\left(\sum_{j=1}^{2}\theta_{Bj} - 2\theta_C\right)$$
$$+ 2c_{Y2}h_1\left[\sum_{j=1}^{2}\left(\dot{y}_{Bj} - h_2\dot{\theta}_{Bj}\right) - 2\dot{y}_C - 2h_1\dot{\theta}_C\right] + 2c_{Z2}b_2^2\left(\sum_{j=1}^{2}\dot{\theta}_{Bj} - 2\dot{\theta}_C\right) = I_{XC}\ddot{\theta}_C \tag{123}$$

$$2k_{X2}h_1\left(-\sum_{j=1}^{2}h_2\varphi_{Bj} - 2h_1\varphi_C\right) + 2k_{Z2}d_2\left(-\sum_{j=1}^{2}\zeta_j z_{Bj} - 2d_2\varphi_C\right)$$
$$+ 2c_{X2}h_1\left(-\sum_{j=1}^{2}h_2\dot{\varphi}_{Bj} - 2h_1\dot{\varphi}_C\right) + 2c_{Z2}d_2\left(-\sum_{j=1}^{2}\zeta_j\dot{z}_{Bj} - 2d_2\dot{\varphi}_C\right) = I_{YC}\ddot{\varphi}_C \tag{124}$$

$$2k_{X2}b_2^2\left(\sum_{j=1}^{2}\psi_{Bj} - 2\psi_C\right) + 2k_{Y2}d_2\left[\sum_{j=1}^{2}\zeta_j\left(y_{Bj} - h_2\theta_{Bj}\right) - 2d_2\psi_C\right]$$
$$+ 2c_{X2}b_2^2\left(\sum_{j=1}^{2}\dot{\psi}_{Bj} - 2\dot{\psi}_C\right) + 2c_{Y2}d_2\left[\sum_{j=1}^{2}\zeta_j\left(\dot{y}_{Bj} - h_2\dot{\theta}_{Bj}\right) - 2d_2\dot{\psi}_C\right] = I_{ZC}\ddot{\psi}_C \tag{125}$$

where $\zeta_1 = 1$ for the front bogie and $\zeta_2 = -1$ for the rear bogie.

b. Bogies

$$\begin{aligned}
&2k_{Y1}\left(-2y_{Bj} - 2h_3\theta_{Bj} + \sum_{k=2j-1}^{2j} y_{Wk}\right) + 2k_{Y2}\left(y_C + h_1\theta_C + \zeta_j d_2\psi_C - y_{Bj} + h_2\theta_{Bj}\right) \\
&\quad + 2c_{Y1}\left(-2\dot{y}_{Bj} - 2h_3\dot{\theta}_{Bj} + \sum_{k=2j-1}^{2j} \dot{y}_{Wk}\right) + 2c_{Y2}\left(\dot{y}_C + h_1\dot{\theta}_C + \zeta_j d_2\dot{\psi}_C - \dot{y}_{Bj} + h_2\dot{\theta}_{Bj}\right) \\
&\quad = m_B\ddot{y}_{Bj}
\end{aligned} \tag{126}$$

$$\begin{aligned}
&2k_{Z1}\left(-2z_{Bj} + \sum_{k=2j-1}^{2j} z_{Wk}\right) + 2k_{Z2}\left(z_C - \zeta_j d_2\varphi_C - z_{Bj}\right) \\
&\quad + 2c_{Z1}\left(-2\dot{z}_{Bj} + \sum_{k=2j-1}^{2j} \dot{z}_{Wk}\right) + 2c_{Z2}\left(\dot{z}_C - \zeta_j d_2\dot{\varphi}_C - \dot{z}_{Bj}\right) = m_B\ddot{z}_{Bj}
\end{aligned} \tag{127}$$

$$\begin{aligned}
&2k_{Y1}h_3\left(-2y_{Bj} - 2h_3\theta_{Bj} + \sum_{k=2j-1}^{2j} y_{Wk}\right) + 2k_{Z1}b_1^2\left(-2\theta_{Bj} + \sum_{k=2j-1}^{2j} \theta_{Wk}\right) \\
&\quad + 2k_{Y2}h_2\left(-y_C - h_1\theta_C - \zeta_j d_2\psi_C + y_{Bj} - h_2\theta_{Bj}\right) + 2k_{Z2}b_2^2\left(\theta_C - \theta_{Bj}\right) \\
&\quad + 2c_{Y1}h_3\left(-2\dot{y}_{Bj} - 2h_3\dot{\theta}_{Bj} + \sum_{k=2j-1}^{2j} \dot{y}_{Wk}\right) + 2c_{Z1}b_1^2\left(-2\dot{\theta}_{Bj} + \sum_{k=2j-1}^{2j} \dot{\theta}_{Wk}\right) \\
&\quad + 2c_{Y2}h_2\left(-\dot{y}_C - h_1\dot{\theta}_C - \zeta_j d_2\dot{\psi}_C + \dot{y}_{Bj} - h_2\dot{\theta}_{Bj}\right) + 2c_{Z2}b_2^2\left(\dot{\theta}_C - \dot{\theta}_{Bj}\right) \\
&\quad = I_{XB}\ddot{\theta}_{Bj}
\end{aligned} \tag{128}$$

$$\begin{aligned}
&-4k_{X1}h_3^2\varphi_{Bj} + 2k_{Z1}d_1\left(-2d_1\varphi_{Bj} - \sum_{k=2j-1}^{2j} \eta_k z_{Wk}\right) \\
&\quad + 2k_{X2}h_2\left(-h_1\varphi_C - h_2\varphi_{Bj}\right) - 4c_{X1}h_3^2\dot{\varphi}_{Bj} \\
&\quad + 2c_{Z1}d_1\left(-2d_1\dot{\varphi}_{Bj} - \sum_{k=2j-1}^{2j} \eta_k \dot{z}_{Wk}\right) + 2c_{X2}h_2\left(-h_1\dot{\varphi}_C - h_2\dot{\varphi}_{Bj}\right) = I_{YB}\ddot{\varphi}_{Bj}
\end{aligned} \tag{129}$$

$$
\begin{aligned}
&-4k_{X1}b_1^2\psi_{Bj}+2k_{Y1}d_1\left(-2d_1\psi_{Bj}+\sum_{k=2j-1}^{2j}\eta_k y_{Wk}\right)+2k_{X2}b_2^2\left(\psi_C-\psi_{Bj}\right)\\
&-4c_{X1}b_1^2\dot{\psi}_{Bj}+2c_{Y1}d_1\left(-2d_1\dot{\psi}_{Bj}+\sum_{k=2j-1}^{2j}\eta_k \dot{y}_{Wk}\right)+2c_{X2}b_2^2\left(\dot{\psi}_C-\dot{\psi}_{Bj}\right)=I_{ZB}\ddot{\psi}_{Bj}
\end{aligned}
\tag{130}
$$

where $\eta_1=\eta_3=1$ for the wheel-set in the front bogie and $\eta_2=\eta_4=-1$ for the wheel-set in the rear bogie. Also, $j=1$ for front bogie, and $j=2$ for rear bogie.

c. The k th wheel-set

$$
2k_{Y1}\left(y_{Bj}+h_3\theta_{Bj}+\eta_k d_1\psi_{Bj}-y_{Wk}\right)+2c_{Y1}\left(\dot{y}_{Bj}+h_3\dot{\theta}_{Bj}+\eta_k d_1\dot{\psi}_{Bj}-\dot{y}_{Wk}\right)=m_W\ddot{y}_{Wk} \tag{131}
$$

$$
2k_{Z1}\left(z_{Bj}-\eta_k d_1\varphi_{Bj}-z_{Wk}\right)+2c_{Z1}\left(\dot{z}_{Bj}-\eta_k d_1\dot{\varphi}_{Bj}-\dot{z}_{Wk}\right)=m_W\ddot{z}_{Wk} \tag{132}
$$

$$
2k_{Z1}b_1^2\left(\theta_{Bj}-\theta_{Wk}\right)+2c_{Z1}b_1^2\left(\dot{\theta}_{Bj}-\dot{\theta}_{Wk}\right)=I_{XW}\ddot{\theta}_{Wk} \tag{133}
$$

Track Irregularity

Dynamic responses of a vehicle are affected by geometrical uncertainty of tracks known as the track irregularity. Track irregularities are an important source of vehicle vibrations during operation and should be considered in numerical simulations (Dinh et al., 2009; Song et al., 2003). In this study, the German track irregularity spectra are utilized, which can apply to high-speed trains faster than 250 km/h (Xia et al., 2017). The used PSD functions are expressed as (Salcher et al., 2016):

$$
\begin{aligned}
S_n\left(\Omega_m\right)&=\frac{A_n\Omega_c^2}{\left(\Omega_m^2+\Omega_r^2\right)\left(\Omega_m^2+\Omega_c^2\right)},\qquad n=\{y,z\}\\
S_c\left(\Omega_m\right)&=\frac{A_z b^{-2}\Omega_c^2\Omega_m^2}{\left(\Omega_m^2+\Omega_r^2\right)\left(\Omega_m^2+\Omega_c^2\right)\left(\Omega_m^2+\Omega_s^2\right)}
\end{aligned}
\tag{134}
$$

where S_y, S_z, and S_c is the PSD function of alignment (horizontal), vertical, and cross-level irregularities, respectively, A is the roughness coefficient, Ω_c, Ω_r, and Ω_s, are the cutoff frequencies, and b is half of the distance between the left and right rail centers. The spatial distribution of track irregularities as a function of the longitudinal location of the tunnel is generated by superposition of a certain number of harmonic functions (Salcher et al., 2016).

$$I_{r,k}(x) = \sqrt{2}\sum_{m=1}^{M} A_{k,m}\cos\left(\Omega_m x + \varepsilon_{k,m}\right), \quad k = \{y, z, c\} \tag{135}$$

where $A_{k,m}$ is m th amplitude of harmonic functions, $\varepsilon_{k,m}$ is a uniformly distributed random-phase angle between 0 to 2π. $A_{k,m}$ is calculated by the following equation (Salcher et al., 2016):

$$A_{k,m} = \sqrt{\left(S_k(\Omega_m)/\pi + S_k(0)a/(6\pi)\right)\Delta\Omega}, \quad k = \{y, z, c\} \tag{136}$$

where $a = 4$ for $m = 1$, $a = 1$ for $m = 2$, and $a = 0$ for $m \geq 3$. The torsional Irregularity is calculated by dividing the cross-level irregularity by a distance between the left and right rail centers. The generated track irregularities are superposed to tunnel responses to solve tunnel-vehicle interaction.

Tunnel-Vehicle Interaction

Solving the tunnel-vehicle interaction is an important issue to couple a tunnel and a vehicle (ZHANG et al., 2010). Especially, there is the rail installed in the tunnel, and wheels interact with the rail. In this study, the wheel-rail correspondence assumption,

which assumes that there is no relative motion between the rail and the wheel, is used to solve the tunnel-vehicle interaction in vertical and torsional (roll) directions. Therefore, these motions are treated as pre-defined boundary conditions. These terms move to the right side of the equation, and the related DOFs are eliminated in the equation of motion. If rearranging Equation (119) into known displacement terms (i.e., wheel heave and roll (torsional) motions) and unknown displacement terms (i.e., other DOF motions), the governing equation of motion in a matrix form can be further expressed as:

$$\begin{bmatrix} \mathbf{M}_{FF} & \mathbf{0} \\ \mathbf{0} & \mathbf{M}_{SS} \end{bmatrix} \begin{Bmatrix} \ddot{\mathbf{X}}_F \\ \ddot{\mathbf{X}}_S \end{Bmatrix} + \begin{bmatrix} \mathbf{C}_{FF} & \mathbf{C}_{FS} \\ \mathbf{C}_{SF} & \mathbf{C}_{SS} \end{bmatrix} \begin{Bmatrix} \dot{\mathbf{X}}_F \\ \dot{\mathbf{X}}_S \end{Bmatrix} + \begin{bmatrix} \mathbf{K}_{FF} & \mathbf{K}_{FS} \\ \mathbf{K}_{SF} & \mathbf{K}_{SS} \end{bmatrix} \begin{Bmatrix} \mathbf{X}_F \\ \mathbf{X}_S \end{Bmatrix} = \begin{Bmatrix} \mathbf{F}_F \\ \mathbf{0} \end{Bmatrix} \tag{137}$$

where

$$\begin{aligned} \mathbf{X}_F &= \{\mathbf{X}_C \;\; \mathbf{X}_{B1} \;\; \mathbf{X}_{B2} \;\; y_{W1} \;\; y_{W2} \;\; y_{W3} \;\; y_{W4}\}^T \\ \mathbf{X}_S &= \{z_{W1} \;\; \theta_{W1} \;\; z_{W2} \;\; \theta_{W2} \;\; z_{W3} \;\; \theta_{W3} \;\; z_{W4} \;\; \theta_{W4}\}^T \end{aligned} \tag{138}$$

$\mathbf{X}_F$ is the displacement vector of unknown DOFs, and $\mathbf{X}_S$ is the displacement vector of known DOFs. After eliminating the known DOFs in the above equation, the following equations of motion can be derived:

$$\mathbf{M}_{FF}\ddot{\mathbf{X}}_F + \mathbf{C}_{FF}\dot{\mathbf{X}}_F + \mathbf{K}_{FF}\mathbf{X}_F = \mathbf{F}_F - \mathbf{C}_{FS}\dot{\mathbf{X}}_S - \mathbf{K}_{FS}\mathbf{X}_S \tag{139}$$

Lateral wheel-rail interaction is based on the simplified Kalker creep theory (Zhang and Xia, 2013). To be specific, the horizontal interaction force $\mathbf{F}_F$ can be calculated and arranged in terms of vehicle and tunnel velocities in the left- and right-hand sides, respectively:

$$\mathbf{F}_F = \frac{2f_{22}}{V}\begin{Bmatrix} \mathbf{0}_{15\times1} \\ \dot{y}_{R1} - \dot{y}_{W1} \\ \dot{y}_{R2} - \dot{y}_{W2} \\ \dot{y}_{R3} - \dot{y}_{W3} \\ \dot{y}_{R4} - \dot{y}_{W4} \end{Bmatrix} = \frac{2f_{22}}{V}\begin{Bmatrix} \mathbf{0}_{15\times1} \\ \dot{y}_{R1} \\ \dot{y}_{R2} \\ \dot{y}_{R3} \\ \dot{y}_{R4} \end{Bmatrix} - \frac{2f_{22}}{V}\begin{Bmatrix} \mathbf{0}_{15\times1} \\ \dot{y}_{W1} \\ \dot{y}_{W2} \\ \dot{y}_{W3} \\ \dot{y}_{W4} \end{Bmatrix} \tag{140}$$

where

$$\mathbf{F}_F = \mathbf{F}_{FR} - \mathbf{C}_C\dot{\mathbf{X}}_F \tag{141}$$

$$\mathbf{F}_{FR} = \frac{2f_{22}}{V}\left\{\mathbf{0}_{1\times15} \quad \dot{y}_{R1} \quad \dot{y}_{R2} \quad \dot{y}_{R3} \quad \dot{y}_{R4}\right\}^T \tag{142}$$

$$\mathbf{C}_C = \frac{2f_{22}}{V}\begin{Bmatrix} \mathbf{0}_{15\times15} & \\ & \mathbf{1}_{4\times4} \end{Bmatrix} \tag{143}$$

y_R is a horizontal displacement of the tunnel with consideration of track irregularity, i.e., $y_R = y_T + I_{r,y}$ at an instantaneous position of a wheel-set of a vehicle element, y_T is a lateral displacement of a tunnel element contacting with a wheel-set, and f_{22} is the Kalker coefficient.

Therefore, the final form of the equation of motion for the vehicle element is expressed as follows:

$$\mathbf{M}_{FF}\ddot{\mathbf{X}}_F + \left(\mathbf{C}_{FF} + \mathbf{C}_C\right)\dot{\mathbf{X}}_F + \mathbf{K}_{FF}\mathbf{X}_F = \mathbf{F}_{FR} - \mathbf{C}_{FS}\dot{\mathbf{X}}_S - \mathbf{K}_{FS}\mathbf{X}_S = \mathbf{F}_{FE} \tag{144}$$

where

$$\mathbf{M}_{FF} = diag\left[\mathbf{M}_C \quad \mathbf{M}_{B1} \quad \mathbf{M}_{B2} \quad \mathbf{M}_W\right] \tag{145}$$

$$\mathbf{M}_C = diag\left[m_C \quad m_C \quad I_{XC} \quad I_{YC} \quad I_{ZC}\right] \tag{146}$$

$$\mathbf{M}_{B1} = \mathbf{M}_{B2} = diag\left[m_B \quad m_B \quad I_{XB} \quad I_{YB} \quad I_{ZB}\right] \tag{147}$$

$$\mathbf{M}_W = diag\begin{bmatrix} m_W & m_W & m_W & m_W \end{bmatrix} \tag{148}$$

$$\mathbf{K}_{FF} = \begin{bmatrix} \mathbf{K}_{CC} & & & & sym. \\ \mathbf{K}_{TC}(1) & \mathbf{K}_{TT1}+\mathbf{K}_{TT2} & & & \\ \mathbf{K}_{TC}(-1) & \mathbf{0} & \mathbf{K}_{TT1}+\mathbf{K}_{TT2} & & \\ \mathbf{0} & \mathbf{K}_{WT} & \mathbf{0} & \mathbf{K}_{WW} & \\ \mathbf{0} & \mathbf{0} & \mathbf{K}_{WT} & \mathbf{0} & \mathbf{K}_{WW} \end{bmatrix} \tag{149}$$

$$\mathbf{K}_{CC} = \begin{bmatrix} 4k_{Y2} & & & & sym. \\ 0 & 4k_{Z2} & & & \\ 4k_{Y2}h_1 & 0 & 4k_{Y2}h_1^2+4k_{Z2}b_2^2 & & \\ 0 & 0 & 0 & 4k_{X2}h_1^2+4k_{Z2}d_2^2 & \\ 0 & 0 & 0 & 0 & 4k_{X2}b_2^2+4k_{Y2}d_2^2 \end{bmatrix} \tag{150}$$

$$\mathbf{K}_{TC}(i) = \begin{bmatrix} -2k_{Y2} & 0 & -2k_{Y2}h_1 & 0 & -2ik_{Y2}d_2 \\ 0 & -2k_{Z2} & 0 & 2ik_{Z2}d_2 & 0 \\ 2k_{Y2}h_2 & 0 & 2k_{Y2}h_1h_2-2k_{Z2}b_2^2 & 0 & 2ik_{Y2}d_2h_2 \\ 0 & 0 & 0 & 2k_{X2}h_1h_2 & 0 \\ 0 & 0 & 0 & 0 & -2k_{X2}b_2^2 \end{bmatrix} \tag{151}$$

$$\mathbf{K}_{TT1} = \begin{bmatrix} 4k_{Y1} & & & & sym. \\ 0 & 4k_{Z1} & & & \\ 4k_{Y1}h_3 & 0 & 4k_{Y1}h_3^2+4k_{Z1}b_1^2 & & \\ 0 & 0 & 0 & 4k_{X1}h_3^2+4k_{Z1}d_1^2 & \\ 0 & 0 & 0 & 0 & 4k_{X1}b_1^2+4k_{Y1}d_1^2 \end{bmatrix} \tag{152}$$

$$\mathbf{K}_{TT2} = \begin{bmatrix} 2k_{Y2} & & & & sym. \\ 0 & 2k_{Z2} & & & \\ -2k_{Y2}h_2 & 0 & 2k_{Y2}h_2^2+2k_{Z2}b_2^2 & & \\ 0 & 0 & 0 & 2k_{X2}h_2^2 & \\ 0 & 0 & 0 & 0 & 2k_{X2}b_2^2 \end{bmatrix} \tag{153}$$

$$\mathbf{K}_{WT} = \begin{bmatrix} -2k_{Y1} & 0 & -2k_{Y1}h_3 & 0 & -2k_{Y1}d_1 \\ -2k_{Y1} & 0 & -2k_{Y1}h_3 & 0 & 2k_{Y1}d_1 \end{bmatrix} \tag{154}$$

$$\mathbf{K}_{WW} = \begin{bmatrix} 2k_{Y1} & 0 \\ 0 & 2k_{Y1} \end{bmatrix} \tag{155}$$

Note that a damping matrix $\mathbf{C}_{FF}$ can be obtained by simply replacing spring coefficients given in $\mathbf{K}_{FF}$ with damping coefficients. Besides, with the rail displacements of y_{Rk}, z_{Rk}, and θ_{Rk} at the position of k th wheel-set, the external force vector $\mathbf{F}_{FE}$ is represented as follows:

$$\begin{Bmatrix} F_7 \\ F_8 \\ F_9 \end{Bmatrix} = 2k_{Z1} \begin{Bmatrix} z_{R1} + z_{R2} \\ b_1^2 \left(\theta_{R1} + \theta_{R2} \right) \\ -d_1 \left(z_{R1} - z_{R2} \right) \end{Bmatrix} + 2c_{Z1} \begin{Bmatrix} \dot{z}_{R1} + \dot{z}_{R2} \\ b_1^2 \left(\dot{\theta}_{R1} + \dot{\theta}_{R2} \right) \\ -d_1 \left(\dot{z}_{R1} - \dot{z}_{R2} \right) \end{Bmatrix}$$

$$\begin{Bmatrix} F_{12} \\ F_{13} \\ F_{14} \end{Bmatrix} = 2k_{Z1} \begin{Bmatrix} z_{R3} + z_{R4} \\ b_1^2 \left(\theta_{R3} + \theta_{R4} \right) \\ -d_1 \left(z_{R3} - z_{R4} \right) \end{Bmatrix} + 2c_{Z1} \begin{Bmatrix} \dot{z}_{R3} + \dot{z}_{R4} \\ b_1^2 \left(\dot{\theta}_{R3} + \dot{\theta}_{R4} \right) \\ -d_1 \left(\dot{z}_{R3} - \dot{z}_{R4} \right) \end{Bmatrix} \tag{156}$$

$$\begin{Bmatrix} F_{16} \\ F_{17} \\ F_{18} \\ F_{19} \end{Bmatrix} = \frac{2f_{22}}{V} \begin{Bmatrix} \dot{y}_{R1} \\ \dot{y}_{R2} \\ \dot{y}_{R3} \\ \dot{y}_{R4} \end{Bmatrix}$$

From the derived equations of motion, the force vector acting on the floating tunnel from k th wheel-set by the vehicle-rail interaction can be expressed.

$$F_Y = 2f_{22} \frac{\left(\dot{y}_{Wk} - \dot{y}_{Rk} \right)}{V} = 2f_{22} \frac{\dot{y}_{Wk} - \dot{I}_{r,y} - \dot{y}_{Tk}}{V} \tag{157}$$

$$F_Z = 2k_{Z1} \left(z_{Bj} - \eta_k d_1 \varphi_{Bj} - z_{Rk} \right) + 2c_{Z1} \left(\dot{z}_{Bj} - \eta_k d_1 \dot{\varphi}_{Bj} - \dot{z}_{Rk} \right) - \frac{m_E}{4} g - m_W \ddot{z}_{Rk} \tag{158}$$

$$F_\theta = 2k_{Z1} b_1^2 \left(\theta_{Bj} - \theta_{Rk} \right) + 2c_{Z1} b_1^2 \left(\dot{\theta}_{Bj} - \dot{\theta}_{Rk} \right) - I_{Xw} \ddot{\theta}_{Rk} \tag{159}$$

where m_E and m_W are the masses of a vehicle element and a wheel-set, $\dot{y}_W$ is the

horizontal velocity of a wheel-set, $\dot{I}_{r,y}$ is the velocity associated with alignment (horizontal) track irregularity, $\dot{y}_T$ is the horizontal velocity of a tunnel, and g is gravity acceleration. The vehicle-SFT interaction is, therefore, simulated by adding external force from a vehicle to tunnel or vice versa. The static gravity force by a vehicle is only exerted on the tunnel while the force is not considered in the reverse direction.

In addition, to calculate derailment and offload factors, interaction forces on the left and right wheels should be calculated. From the correspondence assumption, vertical forces acting on the tunnel from left and right wheels are presented as (Zhang and Xia, 2013):

$$\begin{aligned} F_{TL} = &-\frac{m_E g}{8} - \frac{m_W \ddot{z}_W}{2} - \frac{I_{XW}\ddot{\theta}_W}{g_0} + \left(\frac{1}{2} + \frac{b_1}{g_0}\right)\left[k_{Z1}\left(z_{BL} - z_{WL}\right) + c_{Z1}\left(\dot{z}_{BL} - \dot{z}_{WL}\right)\right] \\ &+ \left(\frac{1}{2} - \frac{b_1}{g_0}\right)\left[k_{Z1}\left(z_{BR} - z_{WR}\right) + c_{Z1}\left(\dot{z}_{BR} - \dot{z}_{WR}\right)\right] \end{aligned} \tag{160}$$

$$\begin{aligned} F_{TR} = &-\frac{m_E g}{8} - \frac{m_W \ddot{z}_W}{2} + \frac{I_{XW}\ddot{\theta}_W}{g_0} + \left(\frac{1}{2} - \frac{b_1}{g_0}\right)\left[k_{Z1}\left(z_{BL} - z_{WL}\right) + c_{Z1}\left(\dot{z}_{BL} - \dot{z}_{WL}\right)\right] \\ &+ \left(\frac{1}{2} + \frac{b_1}{g_0}\right)\left[k_{Z1}\left(z_{BR} - z_{WR}\right) + c_{Z1}\left(\dot{z}_{BR} - \dot{z}_{WR}\right)\right] \end{aligned} \tag{161}$$

where I_{XW} is X-moment of inertia of a wheel-set, g_0 is track gauge, and subscripts, B, W, L, and R denote bogie, wheel-set, left, and right, respectively. It is assumed that summation of both loads acts in the center of gravity along the longitudinal location; therefore, the roll motion of the vehicle is purely induced by the torsional track irregularity. Also, the vertical displacements of the left and right locations of the bogie and the wheel-set are defined as follows:

$$
\begin{aligned}
z_{BL} &= z_B - \eta d_1 \varphi_B - b_1 \theta_B \\
z_{BR} &= z_B - \eta d_1 \varphi_B + b_1 \theta_B \\
z_{WL} &= z_W - b_1 \theta_W \\
z_{WR} &= z_W + b_1 \theta_W
\end{aligned} \tag{162}
$$

where $\eta = 1$ for the front bogie and $\eta = -1$ for the rear bogie.

To obtain the creep coefficient, the wheel-rail normal contact force is assumed to be same as static load acting on the tunnel, i.e., $m_E g / 8$, and the LM wheel tread and 60 kg/m standard rail surface are utilized (Xia et al., 2017).

Previous equations are mathematical expressions for a vehicle element. Based on the previous assumption that several independent vehicle elements model a train, a vehicle can be modeled by expanding the matrices and vectors corresponding to the number of the vehicle element. Therefore, the equation of motion for a vehicle is represented by the following equation.

$$
\mathbf{M}_V \ddot{\mathbf{X}}_V + \mathbf{C}_V \dot{\mathbf{X}}_V + \mathbf{K}_V \mathbf{X}_V = \mathbf{F}_V \tag{163}
$$

where

$$
\mathbf{M}_V = diag\left\{ \mathbf{M}_{FF1} \quad \mathbf{M}_{FF2} \quad \mathbf{M}_{FF3} \quad \cdots \quad \mathbf{M}_{FFN} \right\}^T \tag{164}
$$

$$
\mathbf{C}_V = diag\left\{ \mathbf{C}_{FF1} + \mathbf{C}_{C1} \quad \mathbf{C}_{FF2} + \mathbf{C}_{F2} \quad \mathbf{C}_{FF3} + \mathbf{C}_{C3} \quad \cdots \quad \mathbf{C}_{FFN} + \mathbf{C}_{CN} \right\}^T \tag{165}
$$

$$
\mathbf{K}_V = diag\left\{ \mathbf{K}_{FF1} \quad \mathbf{K}_{FF2} \quad \mathbf{K}_{FF3} \quad \cdots \quad \mathbf{K}_{FFN} \right\}^T \tag{166}
$$

$$
\mathbf{X}_V = diag\left\{ \mathbf{X}_{F1} \quad \mathbf{X}_{F2} \quad \mathbf{X}_{F3} \quad \cdots \quad \mathbf{X}_{FN} \right\}^T \tag{167}
$$

$$
\mathbf{F}_V = diag\left\{ \mathbf{F}_{FF1} \quad \mathbf{F}_{FF2} \quad \mathbf{F}_{FF3} \quad \cdots \quad \mathbf{F}_{FFN} \right\}^T \tag{168}
$$

Overall procedures of the tunnel-vehicle interaction model are presented in Figure 49. Firstly, the initial position of the SFT and vehicles are calculated at a time step, $T = t0$. Track irregularities are superposed on responses of the tunnel, which are used for boundary conditions of the wheel-sets. Interaction forces are calculated. Equations of motion of the tunnel and the vehicle are separately solved while their interactions are considered by providing the interaction forces, and dynamic procedures are repeated at the next time step, $T = t0 + \Delta t$.

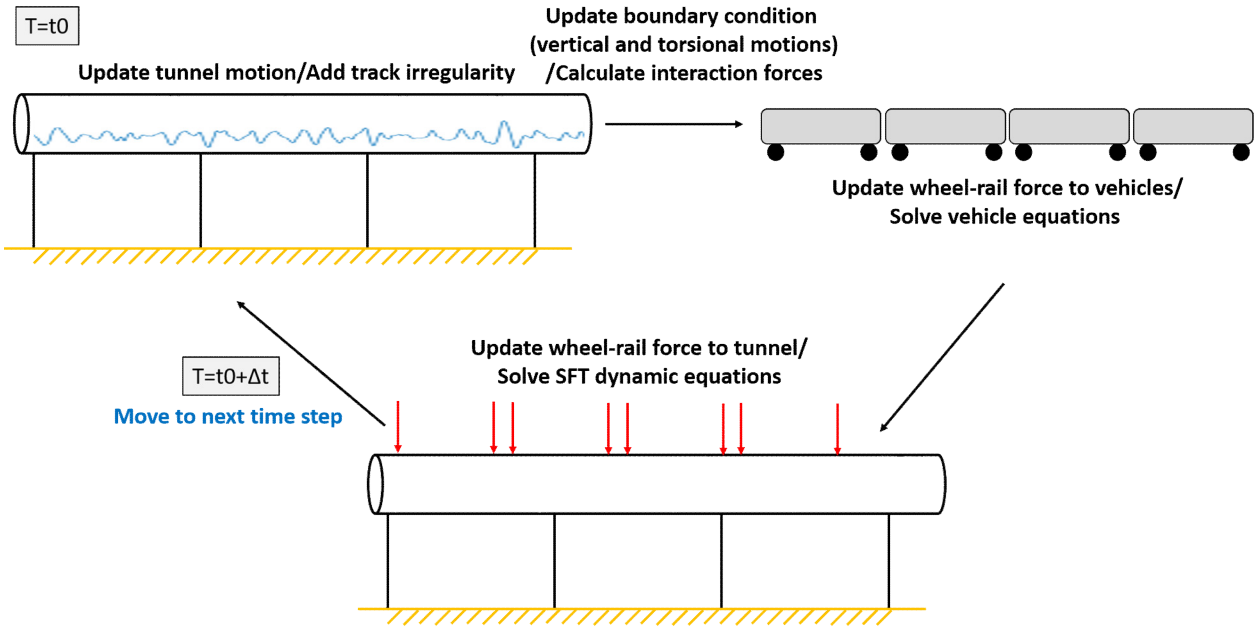

Figure 49. Numerical procedure of the tunnel-vehicle interaction model.

Hydrodynamic Force Computation

The hydrodynamic force is estimated by the Morison equation for a moving object, which consists of linear wave inertia and nonlinear wave drag forces. Thus, the Morison equation, which is given in Equation (63), enables to compute the wave force per unit

length at instantaneous rod-element positions at each time step. A general form of the Morison equation is recalled as follows:

$$\mathbf{F_d} = -C_A \rho A_E \ddot{\mathbf{r}}^n + C_M \rho A_E \dot{\mathbf{V}}^n + \frac{1}{2} C_D \rho D \left| \mathbf{V}^n - \dot{\mathbf{r}}^n \right| \left(\mathbf{V}^n - \dot{\mathbf{r}}^n \right) \tag{169}$$

where C_M , C_A , and C_D are the inertia, added mass, and drag coefficients, ρ is the density of water, A_E is the cross-sectional area for the element, D is the outer diameter, and $\mathbf{V}^n$ and $\dot{\mathbf{V}}^n$ represent velocity and acceleration of a fluid particle normal to the rod centerline. It was shown in Cifuentes et al. (2015) that the use of the Morison equation for SFT dynamics is good enough compared to the case by using the 3D diffraction-radiation-panel program. The Morison equation is further modified to include the hydrodynamic force induced by vertical pressure variations during earthquake excitations, i.e., the seaquake effect, as supported by Islam and Ahrnad (2003), Martinelli et al. (2016), Mousavi et al. (2013), and Wu et al. (2018). In the equation, inertia and drag force terms are modified by introducing the seismic velocity $\mathbf{v}_g^n$ and acceleration $\dot{\mathbf{v}}_g^n$, and the vertical component of seismic velocity and acceleration is considered only for the seaquake simulations as:

$$\mathbf{F_d} = -C_A \rho A_E \ddot{\mathbf{r}}^n + C_M \rho A_E \left(\dot{\mathbf{V}}^n + \dot{\mathbf{v}}_g^n \right) + \frac{1}{2} C_D \rho D \left| \mathbf{V}^n + \mathbf{v}_g^n - \dot{\mathbf{r}}^n \right| \left(\mathbf{V}^n + \mathbf{v}_g^n - \dot{\mathbf{r}}^n \right) \tag{170}$$

Theory of OrcaFlex

A similar approach is used to model the whole structure in OrcaFlex, a well-known commercial program. The tunnel and mooring lines are modeled by line elements, and the

line-element theory is based on the lumped mass method. The line-element consists of a series of nodes and segments. Force properties are lumped in the node, which includes weight, buoyancy, and drag, etc. Stiffness components, i.e., axial, bending, and torsional stiffness, are represented by massless springs (Orcina, 2018). The equation of motion is expressed as:

$$\mathbf{M}(\mathbf{p},\mathbf{a})+\mathbf{C}(\mathbf{p},\mathbf{v})+\mathbf{K}(\mathbf{p})=\mathbf{F}(\mathbf{p},\mathbf{v},t) \tag{171}$$

where $\mathbf{M}(\mathbf{p},\mathbf{a})$, $\mathbf{C}(\mathbf{p},\mathbf{v})$, and $\mathbf{K}(\mathbf{p})$ are mass, damping, and stiffness matrices, $\mathbf{F}(\mathbf{p},\mathbf{v},t)$ is the external force vector, which is the hydrodynamic force in this case, and symbols, $\mathbf{p}$, $\mathbf{v}$, $\mathbf{a}$, and t denote position, velocity, acceleration vectors, and time, respectively. The same Morison equation also computes the hydrodynamic force for a moving object with consideration of the relative velocity and acceleration. The advantage of the developed program compared to OrcaFlex for the present application can be summarized as follows: (i) In OrcaFlex, the hydrodynamic force generated from the seaquake effects is not included. (ii) In CHARM3D, higher-order rod FE elements are used compared to lumped-mass-based OrcaFlex. (iii) The seabed movements can be directly imputed in the developed program. (iv) In CHARM3D, the detailed tunnel-mooring-line-vehicle model is simulated while a simplified model, which changes of tunnel mass at each time, is used for OrcaFlex.

Case Study I: Time-Domain Hydro Elastic Analysis of a Submerged Floating Tunnel with Mooring Lines under Extreme Wave and Seismic Excitations.

Introduction

Global dynamic analysis of a 700-m-long SFT section considered in the South Sea of Korea is carried out under survival random wave and seismic excitations. Hydrodynamic forces on a SFT are evaluated by the modified Morison equation for a moving object so that the hydrodynamic forces by wave or seismic excitations can be computed at its instantaneous positions at every time step. In the case of seabed earthquake, both the dynamic effect transferred through mooring lines and the seawater-fluctuation-induced seaquake effect are considered. For validation purposes, the hydro-elastic analysis results by the developed numerical simulation code are compared with those by a commercial program, OrcaFlex. For the given design condition, dynamic responses of the tunnel and mooring tension are evaluated.

Configuration of the System

Figure 50 shows 2D and 3D views of the entire structure, and Table 8 summarizes major design parameters of the tunnel and mooring lines. The tunnel, which has a diameter of 23 m and a length of 700 m, is made of high-density concrete. Since the structure in this study is a section of the 30-km-long SFT, the fixed-fixed boundary condition at both ends are applied, assuming that strong fixtures (or towers) will be built at 700-m intervals, as shown in Figure 50. Considering that the water depth of the planned site is 100 m, the

submergence depth, a vertical distance between the free surface and the tunnel centerline, is set to be 61.5 m. The BWR is fixed at 1.3, and the tunnel thickness is 2.3 m. The tunnel thickness is actually greater than the real value to have the equivalent tunnel bending stiffness including inner compartment structures. The axial and bending stiffnesses are calculated based on the given data in Table 8.

Chain mooring lines with a nominal diameter of 180 mm are used. High static and dynamic mooring tensions are expected based on the given BWR and wave condition (Jin and Kim, 2017). Also, the maximum mooring tension should be smaller than the minimum breaking load (MBL) divided by the safety factor (SF). Thus, a chain might be the best choice considering high MBL of 30,689 kN for Grade R5. As shown in Figure 50, four 60-degree-inclined mooring lines are installed for every 25-m interval toward the center locations. The lengths of mooring lines are 51.1 m for line #1 and #2 and 37.8 m for line #3 and #4.

The inertia coefficient of the tunnel and mooring lines is 2.0 considering that the added mass is the same as displaced mass (Faltinsen, 1993). The drag coefficient of the tunnel is a function of Reynolds number, KC (Keulegan-Carpenter) number, and relative surface roughness, and the representative value of 0.55 is used here based on the experimental results (e.g., (Thompson, 1980)). The drag coefficient of mooring lines is 2.4 for the stud-less chain (Veritas, 2010).

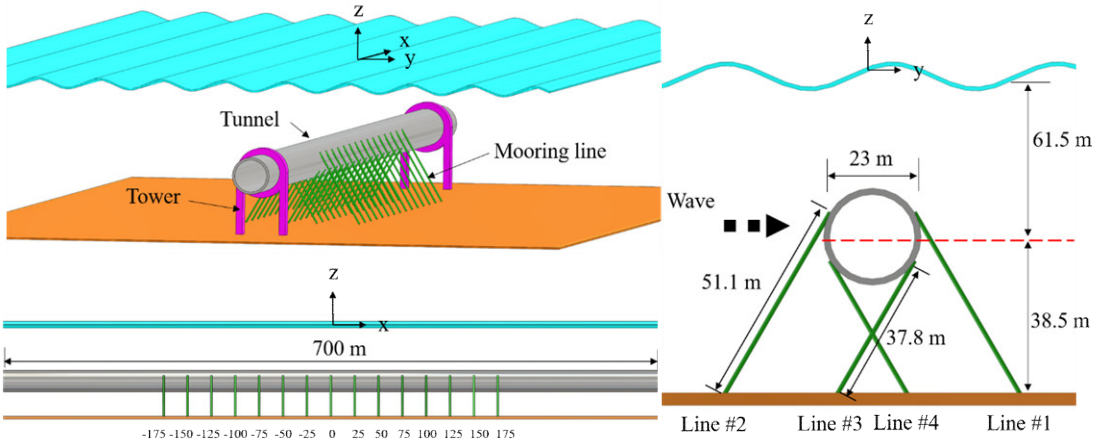

Figure 50. 2 and 3 dimensional views of the entire structure.

Table 8. Major parameters of the tunnel and mooring lines.

Component	Parameter	Value	Unit
Tunnel	Length	700	m
	Outer diameter	23	m
	End boundary condition	Fixed-fixed condition	-
	Material	High-density concrete	-
	Young's modulus	30	GPa
	Bending stiffness (EI)	2.34×10^{11}	kN·m^2
	Axial stiffness (EA)	4.27×10^{9}	kN
	Buoyancy-weight ratio (BWR)	1.3	-
	Added mass coefficient	1.0	-
	Drag coefficient	0.55 (Thompson, 1980)	-
Mooring lines (Chain, Stud-less type)	Length	51.1 (Line # 1 and 2), 37.8 (Line # 3 and 4)	m
	Mass/unit length	644.7	kg/m
	Nominal diameter (d) for wave drag force calculation	0.18	m
	Equivalent outer diameter (D_E) for wave inertia force calculation	0.324 ($D_E = 1.8d$)	m
	Bending stiffness (EI)	0	kN·m^2
	Axial stiffness (EA)	2.77×10^{6}	kN
	Added mass coefficient	1.0	
	Drag coefficient	2.4 (Veritas, 2010)	
	Minimum breaking load (MBL)	30,689 (Grade R5) (Veritas, 2009)	kN

The wet natural frequencies of the tunnel hydro-elastic responses coupled with mooring lines are calculated and presented in Table 9. A stiffness matrix for this specific example presented in Figure 50 is shown in Figure 51. Total 76 lines are used to model the SFT where lines #1~#16 are for tunnel sections, lines # 17~#76 are for mooring lines, and 15 6 DOF rigid bodies are for connection.

Table 9. Wet natural frequencies of the tunnel hydro-elastic responses coupled with mooring lines.

Component	Wet Natural Frequency (rad/s)	Mode Number
Tunnel (Horizontal direction)	1.92	1st mode
	2.70	2nd mode
	4.53	3rd mode
Tunnel (Vertical direction)	3.12	1st mode
	3.45	2nd mode
	4.89	3rd mode
Mooring lines #1 and #2 (Center)	5.78	1st mode
Mooring lines #3 and #4 (Center)	9.04	1st mode

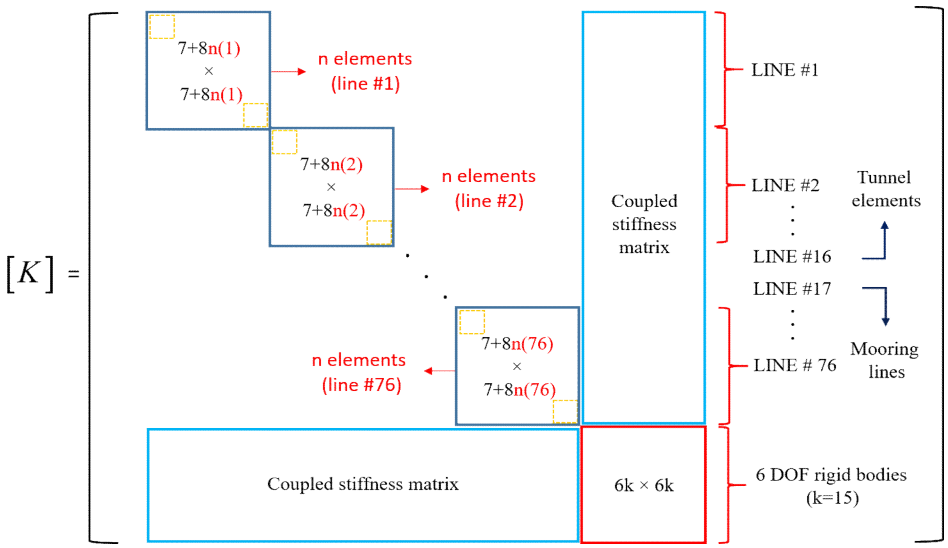

Figure 51. Stiffness matrix for the simulated SFT (line #1~#16 are for a tunnel, and line #17~#76 are for mooring lines, n(1) means the number of sub-elements of line #1, k=15 is the number of the 6 DOF rigid body).

Environmental Conditions

Simultaneous random-wave and seismic excitations are considered for global performance analysis. The same wave and seismic time histories are inputted in both programs for cross-checking. JONSWAP wave spectrum is used to generate time histories of random waves. Significant wave height and peak period for the 100-year-storm condition are 11.7 m and 13.0 s. Enhancement parameter is 2.14 that is the average value in Korea (Suh et al., 2010). Random waves are generated by superposing 100 component waves with randomly perturbed frequency intervals to avoid signal repetition. The lowest and highest cut-off frequencies of the input spectrum are 0.3 rad/s and 2.3 rad/s, respectively. The wave direction is perpendicular to a longitudinal direction of the tunnel. A 3-hour simulation is carried out to analyze the statistics of dynamic behaviors and mooring tensions under the storm condition. Figures 52-53 show theoretical JONSWAP wave spectrum and the reproduced spectrum from the time histories of wave elevation. It also shows the time histories of wave elevation produced by the JONSWAP wave spectrum.

Regular (sinusoidal) and recorded irregular seismic excitations data are also employed. The amplitude of regular seismic motion in the vertical direction is 0.01 m at various frequencies from 0.781 rad/s to 7.805 rad/s. Figures 54-59 show the time histories of seismic displacements and corresponding spectra for recorded irregular seismic excitations in three directions, which are obtained by USGS (USGS, 2018). The earthquake occurred in 78 km WNW of Ferndale, California, USA in 2014, and the magnitude of this earthquake is 6.8 in Richter scale. Seismic displacements in three

directions are inputted for each anchor point of mooring lines and two ends of the tunnel fixture at every time step. The hydrodynamic force from the seaquake effect is also computed for the tunnel and mooring lines, and time histories of the measured seismic velocity and acceleration in the vertical direction are shown in Figures 60-61.

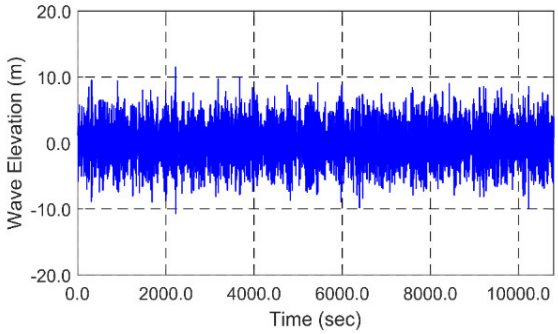

Figure 52. Wave time histories produced by JONSWAP wave spectrum (*Hs*=11.7m, *Tp*=13 sec).

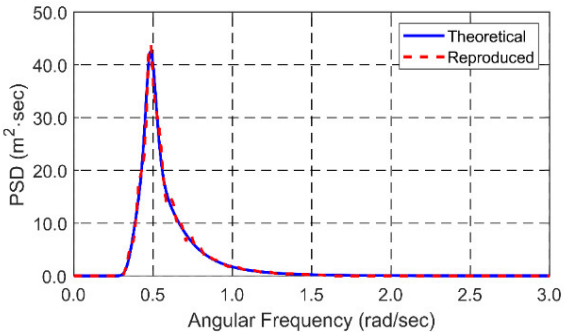

Figure 53. Theoretical JONSWAP wave spectrum and reproduced spectrum for wave time histories using FFT (fast Fourier transform) for validation.

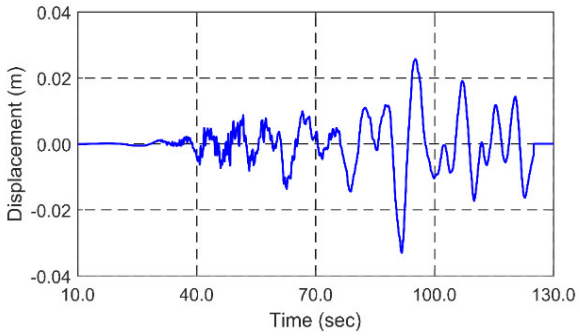

Figure 54. Time history of the measured, real seismic displacement in a longitudinal (x) direction.

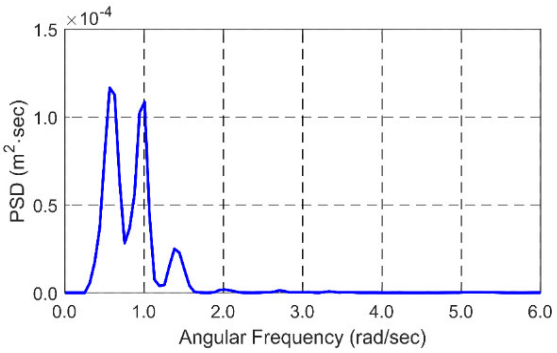

Figure 55. Spectrum of the time history of the measured, real seismic displacement in a longitudinal (x) direction using FFT.

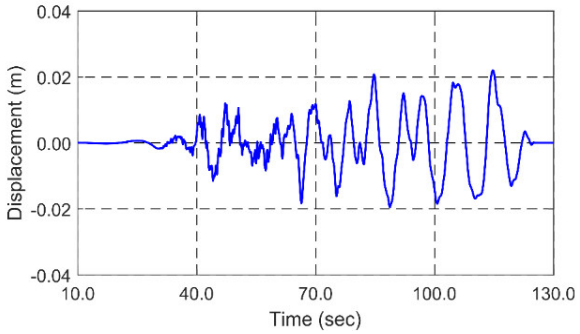

Figure 56. Time history of the measured, real seismic displacement in a transverse (y) direction.

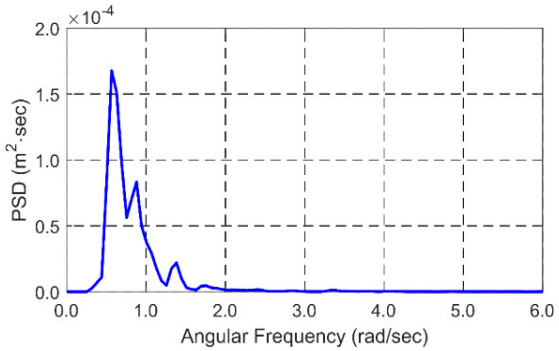

Figure 57. Spectrum of the time history of the measured, real seismic displacement in a transverse (y) direction using FFT.

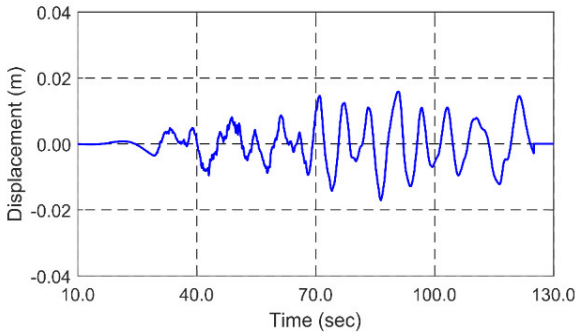

Figure 58. Time history of the measured, real seismic displacement in a vertical (z) direction.

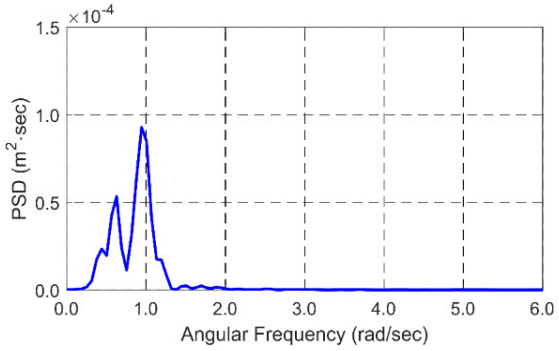

Figure 59. Spectrum of the time history of the measured, real seismic displacement in a vertical (z) direction using FFT.

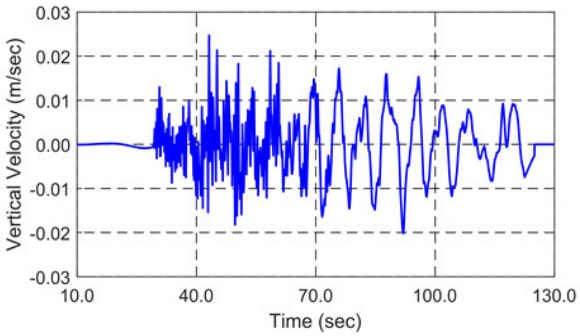

Figure 60. Time history of measured, real seismic velocity in a vertical (z) direction.

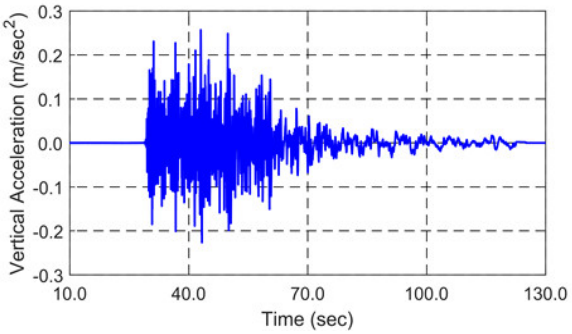

Figure 61. Time history of measured, real seismic acceleration in a vertical (z) direction.

Results and Discussions

Static Analysis

The developed code is first cross-checked with OrcaFlex in the static condition before dynamic simulations. Because static displacements of the tunnel are only affected by weight, buoyancy, and stiffness components of tunnel and mooring lines, a direct comparison can be made after initial modeling of the entire SFT system. Figures 62-63 show the vertical displacements of tunnel and mooring tensions in the static condition.

The results produced by the developed program coincide well with OrcaFelx's results. The reference dashed line in the tension figure indicates the allowable tension (minimum break load divided by safety factor).

In the static condition, the tunnel is slightly curved upward because of excessive net buoyancy and the boundary condition at both ends. It will be true that the higher BWR results in the higher vertical displacement and mooring tension in the static condition at the center location of the tunnel. Since the maximum vertical displacement occurs at middle locations, the maximum mooring tension is also observed in those locations.

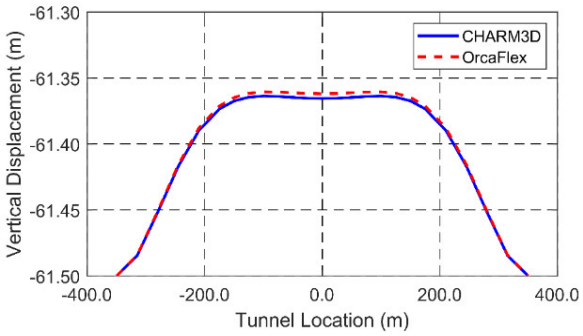

Figure 62. Envelope of the vertical displacement of the tunnel in the static condition.

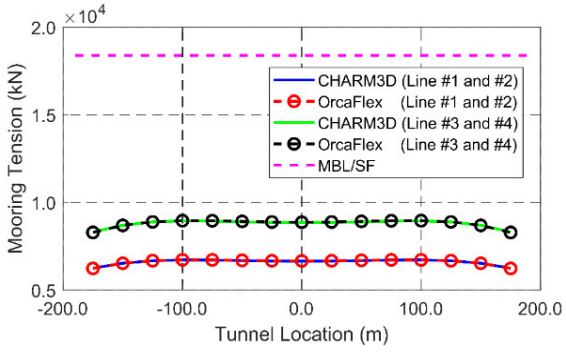

Figure 63. Envelope of the mooring tension in the static condition (The reference dashed line in the tension figure indicates the allowable tension).

Dynamic Behaviors under Extreme Wave Excitations

Dynamic simulations under the 100-year-storm condition (Hs = 11.7 m and Tp = 13.0 s) are performed for three hours. Dynamic loads under the wave excitations can be significant in long waves especially as the submergence depth of the SFT is not enough. Therefore, to confirm its survivability, an extreme wave condition is applied. Not only horizontal and vertical motions of the tunnel but also dynamic mooring tensions are included. Both time histories, corresponding spectra, and envelopes are presented and analyzed.

Figures 64-65 show the envelopes of the maximum and minimum displacements of the tunnel and the maximum mooring tension. As mentioned before, the same wave time histories are inputted to both programs to compare the dynamics results directly; therefore, both computer programs produce almost identical results. The maximum horizontal and vertical responses and mooring tension occur in the middle location. The horizontal responses are larger than the vertical responses since the 1st natural frequency of horizontal motion is closer to the input wave spectrum than that of vertical motion. Mooring-tension results show that shorter mooring lines (Line #3) have higher mooring tension than longer mooring lines (Line #1). The maximum mooring tension in the middle section is smaller than the MBL (minimum breaking load) divided by the SF (safety factor), which is presented in Figure 65 as a pink line. Recall that the MBL is 30,689 kN for Grade R5, which is obtained by DNV regulation (Veritas, 2009). The SF 1.67 is used as recommended by API RP 2SK (API, 1996). Even if the extreme 100-year-storm

condition is considered, the maximum mooring tension is still smaller than the allowable tension.

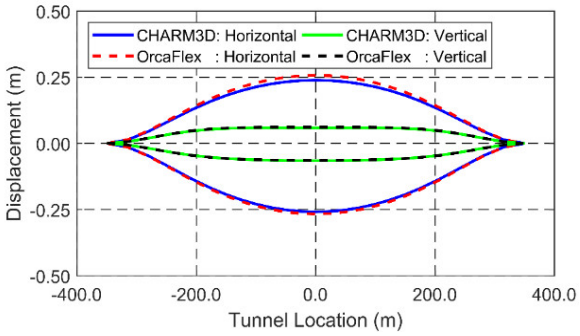

Figure 64. Envelopes of the maximum and minimum displacements of the tunnel in the 100-year-storm condition.

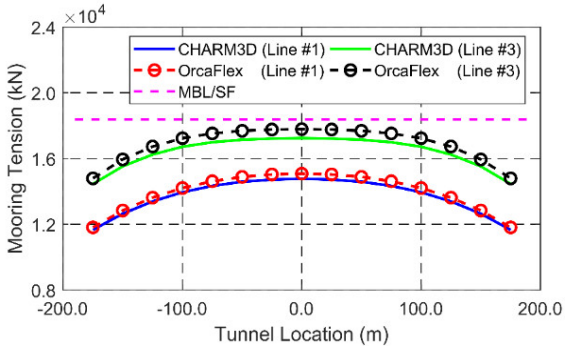

Figure 65. Envelopes of the maximum mooring tension in the 100-year condition (The reference dashed line in the tension figure indicates the allowable tension i.e., minimum break load divided by safety factor of 1.67).

Figures 66-69 show the time histories and corresponding spectra of horizontal/vertical responses of the tunnel in the middle section. The spectra of responses indicate that wave-induced motions are dominant since the lowest natural frequencies in both directional motions (1.92 and 3.12 rad/s for horizontal and vertical directions) are

away from the dominant input-wave spectral range. It means that there is a negligible contribution from the structural elastic resonances. It is also true that horizontal and vertical motions of the tunnel are smaller, as the higher mooring stiffness is used or mass of the tunnel decreases by reducing the size of the tunnel because of increased higher natural frequencies.

Figures 70-71 show the time histories and corresponding spectrum of mooring tension in the middle section. Jin and Kim (2017) evaluated the snap-loadings as a function of the BWR. In their research, it was found that mooring lines can be slack as the tunnel experiences large downward motion. Shortly after that, the mooring lines undergoes largely increased snap-loading with the tunnel bounces back and reaches the maximum upward motion. However, it should be noted that the snap-loadings tend to occur at lower BWRs based on their results. In case of mooring tension, under the given BWR = 1.3, snap-loadings characterized by extraordinary high peaks do not occur, as shown in the time series; therefore, the maximum mooring tension remains smaller than the MBL/SF. In addition, obviously, smaller dynamic motions and mooring tensions can be obtained by further increasing submergence depth (Jin and Kim, 2017). The relevant statistics obtained from the time series are summarized in Table 10.

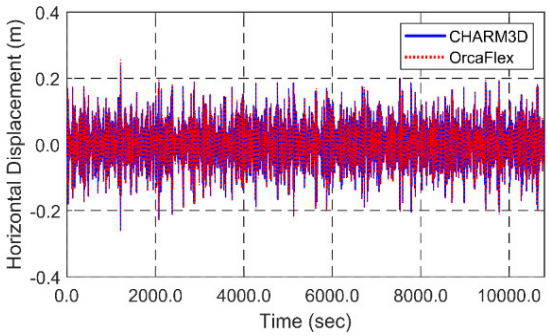

Figure 66. Time histories of horizontal displacement of the tunnel in the middle location under the 100-year-storm waves.

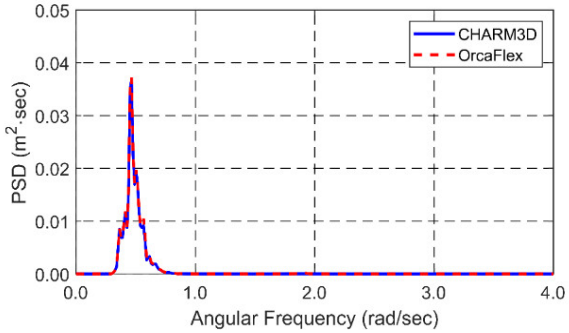

Figure 67. Spectra of horizontal displacement of the tunnel in the middle location under the 100-year-storm waves.

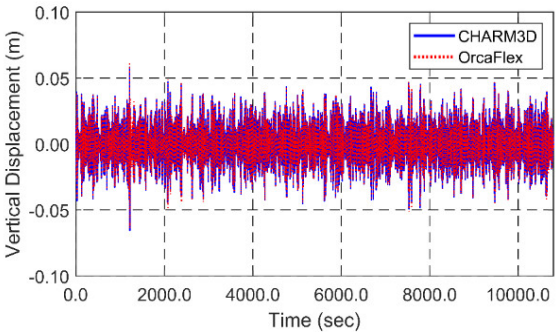

Figure 68. Time histories of vertical displacement of the tunnel in the middle location under the 100-year-storm waves.

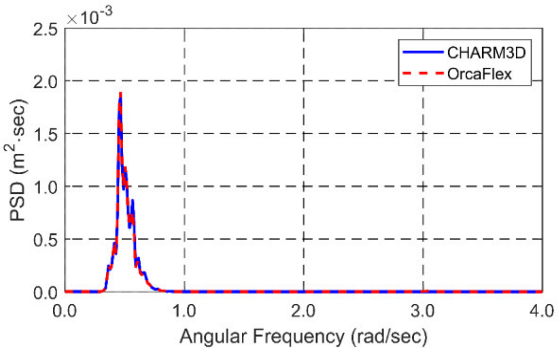

Figure 69. Spectra of vertical displacement of the tunnel in the middle location under the 100-year-storm waves.

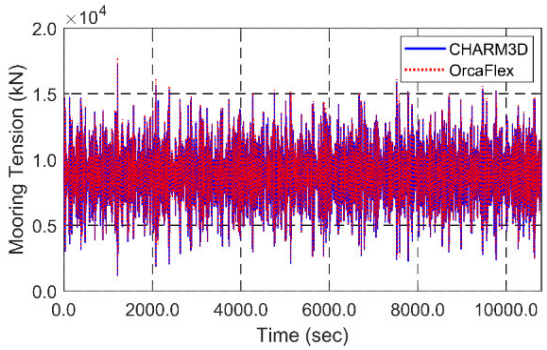

Figure 70. Time histories of mooring tension (#3) in the middle location under the 100-year-storm waves.

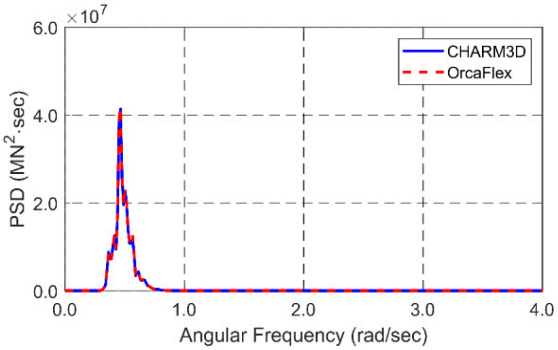

Figure 71. Spectra of mooring tension (#3) in the middle location under the 100-year-storm waves.

Table 10. Statistics of the SFT motions and mooring tensions at the middle location under 100-yr irregular wave excitations (from the time histories).

Parameter	Numerical Model	Maximum	Minimum	Standard Deviation	Unit
Horizontal displacement	OrcaFlex	0.257	-0.267	0.060	m
	CHARM3D	0.243	-0.261	0.059	
Vertical displacement	OrcaFlex	0.060	-0.064	0.014	
	CHARM3D	0.058	-0.066	0.014	
Mooring tension (line #1)	OrcaFlex	15075.76	777.02	1942.91	kN
	CHARM3D	14765.75	885.56	1917.55	
Mooring tension (line #2)	OrcaFlex	15866.39	856.17	1937.59	
	CHARM3D	15276.12	902.94	1919.01	
Mooring tension (line #3)	OrcaFlex	17781.23	1118.96	2032.91	
	CHARM3D	17334.93	1206.64	2015.53	
Mooring tension (line #4)	OrcaFlex	16808.51	1009.08	2039.87	
	CHARM3D	16542.11	953.24	2014.32	

Dynamic Behaviors under Severe Seismic Excitations

Regular and irregular seismic excitations are utilized for SFT dynamic analysis. Since the fixed-fixed boundary condition is applied at both ends of the tunnel, both ends of the tunnel, as well as all anchoring points are assumed to move together with seismic motions. As a result, seismic time histories are inputted to every anchor location of mooring lines and both ends of the tunnel. The hydrodynamic forces generated by sea-water fluctuations under vertical seismic motions are computed by using modified Morison equation (e.g., Islam and Ahrnad (2003), Martinelli et al. (2016), Mousavi et al. (2013), and Wu et al. (2018)). The effect is well known and called seaquake. As a result, there are two mechanisms causing SFT dynamics under seabed seismic motions. First, the seismic motions are transferred through mooring lines. Second, sea-water fluctuations in the vertical direction. In this study, the former will be called earthquake effect (Eq in the legend of figures) and the latter will be called seaquake effect (Sq in the legend of figures). In figures, if both effects are considered, it is indicated as Eq+Sq. To investigate the seaquake effect, regular seismic cases only in the vertical direction are simulated and the resulting SFT dynamics are analyzed. Subsequently, strong real seismic displacements are applied to the SFT system to check the global performance and structural robustness.

Figures 72-73 show tunnel's vertical motion amplitudes at the mid-section and the corresponding vertical responses of mooring line #1 at its center under regular (sinusoidal) seismic excitations. Vertical motions of the tunnel are largely amplified at 3.12 rad/s and 4.89 rad/s, the 1st and 3rd natural frequencies. The amplified tunnel motions at those frequencies directly influence high mooring dynamics, as shown in Figure 73. A small

peak can also be observed at 5.78 rad/s, the lowest natural frequency of mooring lines #1 itself.

The hydrodynamic force by seaquake directly acts on the tunnel with earthquake frequencies. Whereas, the seismic excitations are delivered to the tunnel through mooring lines, as discussed earlier. Then, the resulting tunnel response also causes the hydrodynamic force on the tunnel. Therefore, there exist phase effects between the two components. We can see that the tunnel dynamics are significantly reduced after including the seaquake effect when compared to the earthquake-only case. The reason can be found from Figures 74-76 by plotting the contribution of each constituent component separately. In the figures, the phase of the tunnel response induced by earthquakes is opposite to that induced by seaquake at the tunnel's natural frequencies, 3.12 rad/s and 4.89 rad/s. Therefore, there is a cancellation effect between the two components so that the total vertical response amplitude can be reduced compared to the earthquake-only case. On the other hand, when earthquake frequency is greater than 5.7 rad/s, the two components become in phase, so the tunnel vertical responses are increased compared to the earthquake-only case although the resulting increment is small. The horizontal seismic motions do not generate the seaquake effects if the seabed is flat since the horizontal seabed motions do not influence seawater fluctuating motions.

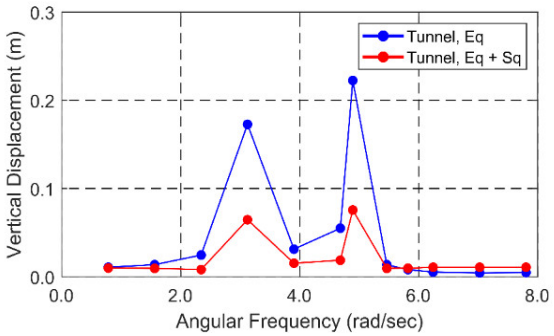

Figure 72. Amplitudes of vertical displacements of the tunnel in the middle location under regular seismic excitations of various frequencies.

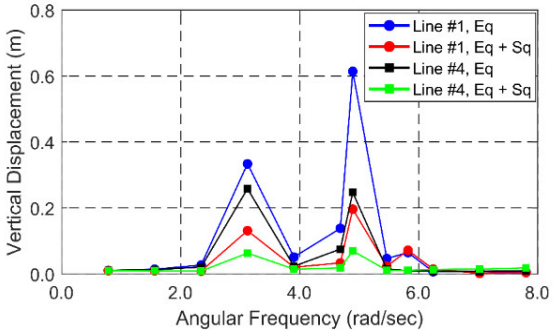

Figure 73. Amplitudes of vertical displacement of mooring line #1 in the middle location under regular seismic excitations of various frequencies.

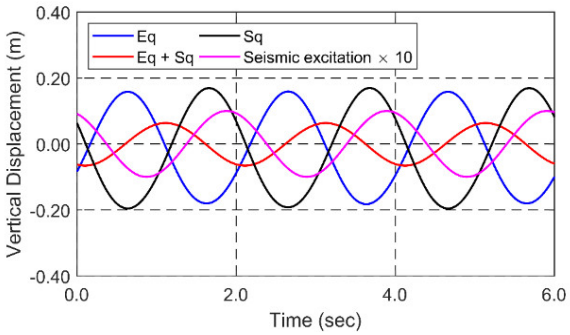

Figure 74. Time histories of vertical displacement of the tunnel in the middle section by respective force components under regular seismic excitations of 3.12 rad/s (time histories of seismic excitations are multiplied by 10).

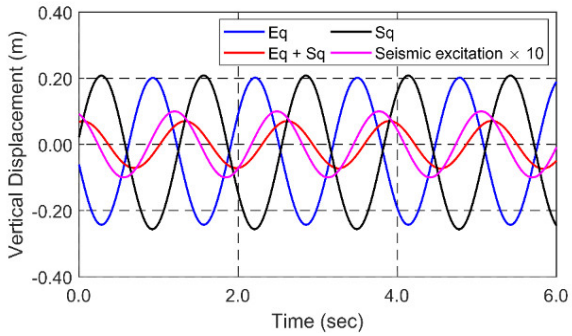

Figure 75. Time histories of vertical displacement of the tunnel in the middle section by respective force components under regular seismic excitations of 4.89 rad/s (time histories of seismic excitations are multiplied by 10).

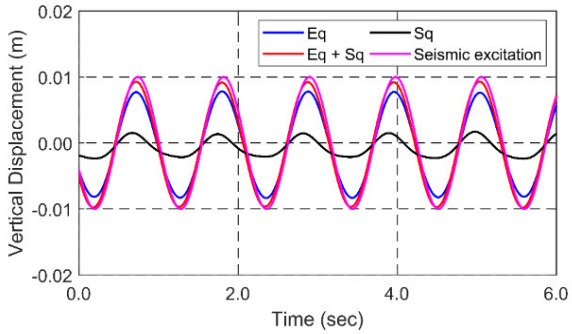

Figure 76. Time histories of vertical displacement of the tunnel in the middle section by respective force components under regular seismic excitations of 5.78 rad/s.

Figures 77-82 show the time histories and corresponding spectra of horizontal and vertical responses of the tunnel and the mooring tensions in the tunnel's middle section under the real seismic excitations, as given in Figures 54-59. The case of earthquake effect only is compared with that of earthquake plus seaquake. First, in the earthquake-only case, the tunnel responses are more significant than the input seismic motions, horizontally about three times and vertically about twice larger. The horizontal responses are more amplified because its lowest natural frequency is closer to the dominant frequency range

of seismic excitations than that of vertical response. The corresponding tunnel-response spectra show that they have the first small peak at the seismic frequency, the next highest peak at the lowest natural frequency, and the next small peak at the third-lowest natural frequency. Mooring tensions are mostly influenced by the SFT horizontal and vertical motions at their lowest natural frequencies, while there is virtually little contribution near seismic frequencies. The maximum tensions for this earthquake case are much smaller than those caused by extreme wave excitations, as previously considered. However, the earthquake-induced tunnel dynamics can be significantly more amplified when the lowest natural frequencies of the tunnel's elastic responses are closer to dominant seismic frequencies. In these figures, the same dynamic simulation results by OrcaFlex are also given for cross-checking. The two independent computer programs produced almost identical results.

In the spectral plots, the spectra of tunnel responses and mooring tensions after adding seaquake effects are also given. In Figure 78, there is little change in the case of SFT horizontal motions since the seaquake mainly influences only the vertical responses, as was pointed out earlier. In Figure 80, there is a significant reduction in the vertical-response spectrum at its lowest natural frequency (3.12 rad/s) after including the seaquake effect. It is due to the phase-cancellation effects, as discussed in the previous regular-earthquake case of Figures 74-75. Thus, this reduction effect directly reflects the reduction in the mooring tension, i.e., in Figure 82, the tension spectral amplitude is greatly reduced near 3.12 rad/s but remains the same at the lowest natural frequency of the horizontal response, 1.92 rad/s. This trend can also be seen in the corresponding time-series

comparisons (Figures 83-84) for the two cases (with and without considering the seaquake effect) regarding vertical tunnel responses and mooring tensions. The relevant statistics obtained from the time series are summarized in Table 11. It is seen that the inclusion of the seaquake effect reduces both vertical SFT responses and mooring tensions, as discussed earlier.

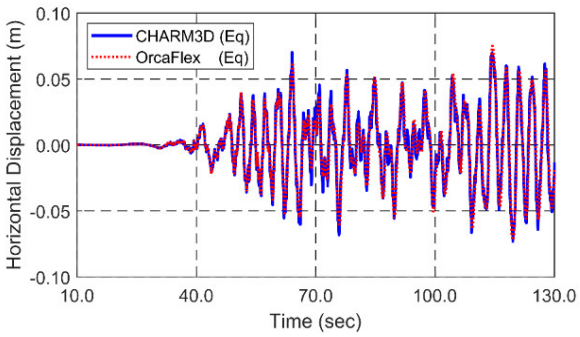

Figure 77. Time histories (without seaquake) of the horizontal tunnel response in the middle location under seismic excitations.

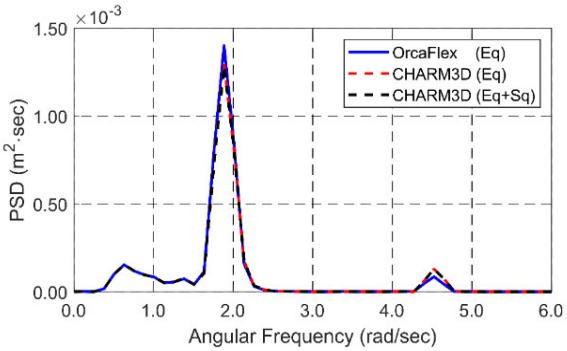

Figure 78. Spectra of the horizontal tunnel response in the middle location under seismic excitations.

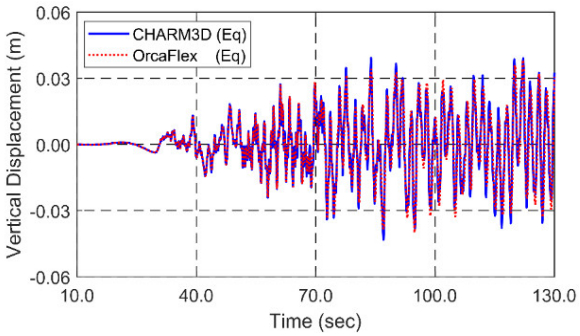

Figure 79. Time histories (without seaquake) of the vertical tunnel response in the middle location under seismic excitations.

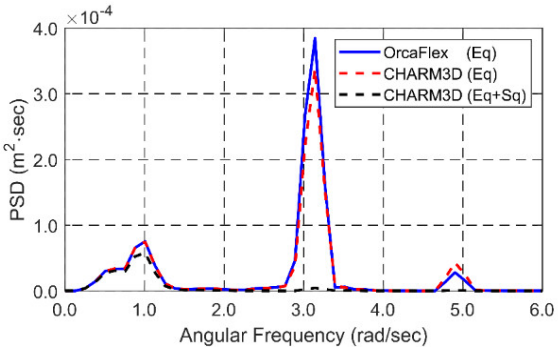

Figure 80. Spectra of the vertical tunnel response in the middle location under seismic excitations.

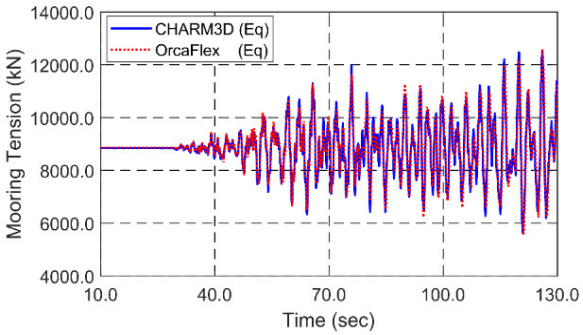

Figure 81. Time histories (without seaquake) of the mooring tension #4 in the middle location under seismic excitations.

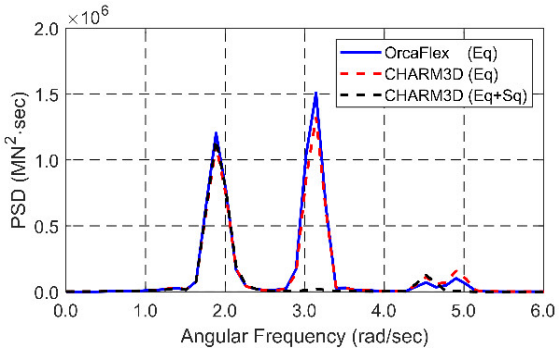

Figure 82. Spectra of the mooring tension #4 in the middle location under seismic excitations.

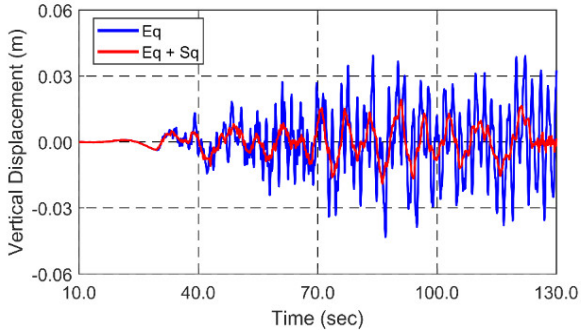

Figure 83. Time histories of the vertical response of the tunnel in the middle location under seismic excitations with and without the seaquake effect.

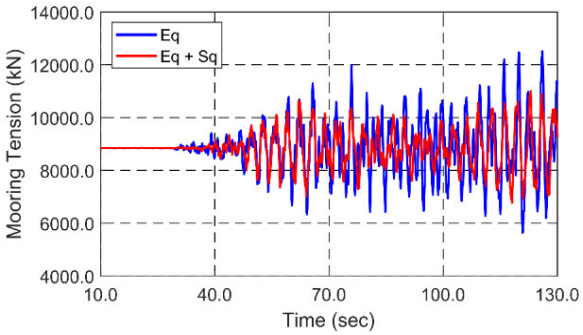

Figure 84. Time histories of mooring tension #4 in the middle location under seismic excitations with and without the seaquake effect.

Table 11. Statistics of the SFT motions and mooring tensions at the middle location under irregular seismic excitations.

Parameter	Numerical Model	Maximum	Minimum	Standard Deviation	Unit
Horizontal displacement	OrcaFlex (Eq)	0.075	-0.072	0.023	m
	CHARM3D (Eq)	0.070	-0.073	0.023	
	CHARM3D (Eq + Sq)	0.070	-0.072	0.023	
Vertical displacement	OrcaFlex (Eq)	0.038	-0.040	0.013	
	CHARM3D (Eq)	0.039	-0.042	0.013	
	CHARM3D (Eq + Sq)	0.019	-0.019	0.006	
Mooring tension (line #1)	OrcaFlex (Eq)	9880.02	3749.05	816.30	kN
	CHARM3D (Eq)	9872.22	3783.56	801.58	
	CHARM3D (Eq + Sq)	8728.01	4631.84	649.80	
Mooring tension (line #2)	OrcaFlex (Eq)	9547.95	3607.73	839.49	
	CHARM3D (Eq)	9722.09	3291.79	829.07	
	CHARM3D (Eq + Sq)	8778.38	4491.79	649.33	
Mooring tension (line #3)	OrcaFlex (Eq)	12147.71	5312.68	969.62	
	CHARM3D (Eq)	12295.18	4918.66	958.46	
	CHARM3D (Eq + Sq)	11009.40	6691.91	649.58	
Mooring tension (line #4)	OrcaFlex (Eq)	12582.40	5543.84	941.84	
	CHARM3D (Eq)	12512.53	5633.35	925.67	
	CHARM3D (Eq + Sq)	11001.66	6772.99	652.55	

Case Study II: Tunnel-Mooring-Vehicle Time-Domain Coupled Dynamic Analysis for a Submerged Floating Tunnel under Wave and Seismic Excitations

Introduction

In this section, a time-domain dynamic model has been developed so that it can solve the interactions between the SFT and a moving train with wave or earthquake excitations. The equations of motion for the tunnel and mooring lines are based on the finite-element rod theory, which is same as the Case Study I, and the computer program is further developed to be applicable to the tunnel-mooring-train coupled dynamic simulations. The vehicle motion is modeled by using the rigid-body dynamic method. Then, the interaction between the tunnel and the vehicle is solved by using the correspondence assumption and Kalker's linear creep theory. To validate the numerical model, the dynamic responses and mooring tensions are compared with those generated by a commercial program, OrcaFlex, for a moving train in the still-water condition. Subsequently, it is checked whether the designed structure satisfies the tunnel-motion and mooring-tension criteria under the applied wave or seismic loads. Finally, safety and passengers' comfort criteria are checked by looking at the dynamics of moving vehicles.

Configuration of the vehicle

A vehicle model used in the present case study is acquired from previous research. This vehicle consists of a total of six cars, and thus total unknown DOFs of the entire vehicle are 114. In particular, trailer cars are located in the 2nd and the 5th, and the rest are

motor cars. The length of each car is 25.5 m. The static wheel-set loads of motor and trailer cars are 142.2 kN and 134.9 kN, respectively. The vehicle parameters, natural frequencies, and mode descriptions are summarized in Tables 12-13.

Table 12. Vehicles parameters (ZHANG et al., 2010).

Item	Motor car	Trailer car	Unit
Distance between wheel-sets, $2d_1$	2.50	2.50	m
Distance between bogies, $2d_2$	18.0	18.0	m
Transverse distance between primary suspensions, $2b_1$	2.05	2.05	m
Transverse distance between secondary suspensions, $2b_2$	2.05	2.05	m
Vertical distance between car-body and secondary suspension, h_1	0.36	0.83	m
Vertical distance between secondary suspension and bogie, h_2	0.24	0.15	m
Vertical distance between bogie and wheel-set, h_3	0.33	0.34	m
Mass of wheel-set, m_W	2,200	1,900	kg
X moment of inertia of wheel-set, I_{XW}	1,630	1,067	kg·m^2
Mass of bogie, m_B	3,400	1,700	kg
X moment of inertia of bogie, I_{XB}	3,200	1,600	kg·m^2
Y moment of inertia of bogie, I_{YB}	7,200	1,700	kg·m^2
Z moment of inertia of bogie, I_{ZB}	6,800	1,700	kg·m^2
Mass of car-body, m_C	42,400	44,000	kg
X moment of inertia of car-body, I_{XC}	101,500	74,000	kg·m^2
Y moment of inertia of car-body, I_{YC}	1,064,400	2,740,000	kg·m^2
Z moment of inertia of car-body, I_{ZC}	867,200	2,740,000	kg·m^2
X spring coefficient of primary suspension, k_{X1}	9.00	15.00	MN/m
Y spring coefficient of primary suspension, k_{Y1}	1.32	5.00	MN/m
Z spring coefficient of primary suspension, k_{Z1}	1.04	0.70	MN/m
X spring coefficient of secondary suspension, k_{X2}	0.24	0.21	MN/m

Table 12. Continued

Item	Motor car	Trailer car	Unit
Y spring coefficient of secondary suspension, k_{Y2}	0.24	0.21	MN/m
Z spring coefficient of secondary suspension, k_{Z2}	0.40	0.35	MN/m
X damping coefficient of primary suspension, c_{X1}	0	0	kNs/m
Y damping coefficient of primary suspension, c_{Y1}	0	0	kNs/m
Z damping coefficient of primary suspension, c_{Z1}	30	38	kNs/m
X damping coefficient of secondary suspension, c_{X2}	120	300	kNs/m
Y damping coefficient of secondary suspension, c_{Y2}	30	15	kNs/m
Z damping coefficient of secondary suspension, c_{Z2}	33	40	kNs/m

Table 13. Natural frequencies and mode descriptions of the vehicle.

Motor-car		Trailer-car	
Frequency (rad/s)	Mode description	Frequency (rad/s)	Mode description
3.40	Lower-center sway and roll motion	2.87	Lower-center sway and roll motion
4.92	Upper-center sway and roll motion	4.90	Car-body yaw motion
5.61	Car-body heave motion	5.04	Car-body heave motion
8.97	Car-body yaw motion	5.76	Car-body pitch motion
10.04	Car-body pitch motion	5.93	Upper-center sway and roll motion

Time History of Track Irregularity

The parameters of the Germany track irregularity spectra are based on the low disturbance condition normally applicable for high-speed trains faster than 250 km/h. The assigned values of Ω_c, Ω_r, and Ω_s are 0.8246, 0.0206, and 0.4380 rad/m, respectively. Besides, the roughness coefficients, A_y and A_z, are 2.119×10^{-7} and 4.032×10^{-7} m^2·rad/m. The spatial angular frequency, Ω_m, ranges from 0.0785 rad/m to 3.14 rad/m

corresponding to the wavelengths of a track irregularity from 2 m to 80 m. 1024 regular wave components are superposed to generated irregular spatial histories of track irregularities along the longitudinal direction of the tunnel. The generated track irregularity has a ramping length of 350 m before and after the tunnel. Therefore, entire vehicle dynamics are not influenced by the sudden variations of track irregularities. The spatial histories of generated track irregularities are shown in Figures 85-86.

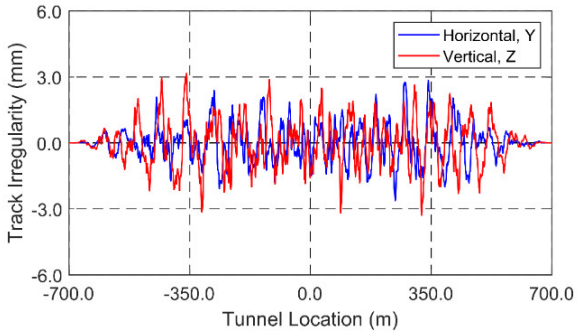

Figure 85. Generated horizontal and vertical track irregularities (Ramping lengths of 350 m are added before and after the tunnel location).

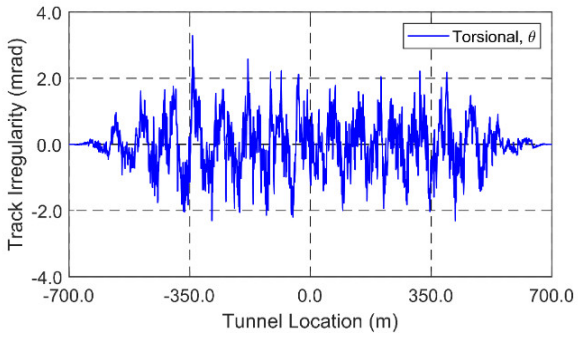

Figure 86. Generated torsional track irregularity (Ramping lengths of 350 m are added before and after the tunnel location).

Environmental Conditions

Random wave and seismic excitations are selected as environmental conditions. The Pierson-Moskowitz (PM) wave spectrum is utilized for the random wave generation. In case of wave excitations, operation conditions are considered since vehicles do not operate during the survival condition. Significant wave height and peak period for the operating condition are set to be 2.0 m and 8.3 sec, respectively. The superposition of 100 regular-component waves produces the corresponding random waves, and randomly perturbed intervals are additionally applied to prevent signal repetition. The lowest and highest cut-off frequencies of the input spectrum are 0.4 rad/s and 2.3 rad/s, respectively. A wave direction is perpendicular to the longitudinal direction of the tunnel. Then, 20-minute simulations are performed with the vehicle time interval of 5 minutes. Figure 87 shows the time history of the random wave, and Figure 88 shows input PM and reproduced wave spectra for validation of the produced time history. As for earthquake input, it is same as the Cast Study I, and the seaquake effect is also considered.

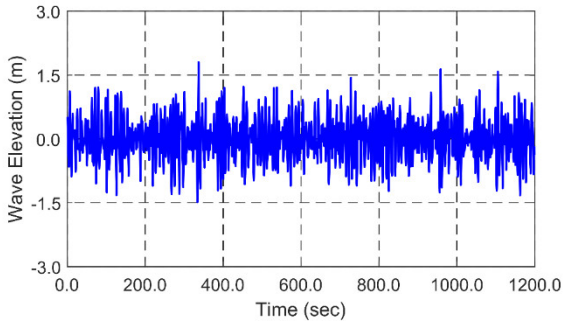

Figure 87. Time history of wave elevation produced by the PM wave spectrum.

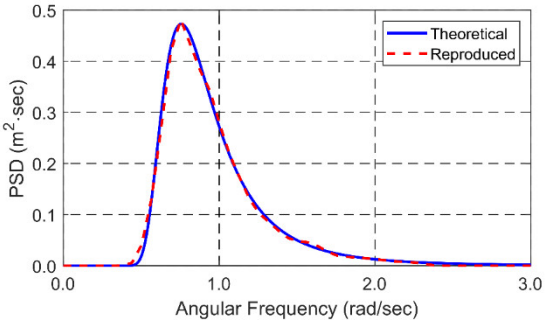

Figure 88. Input PM wave spectrum and the reproduced spectrum from the wave time history for validation.

Results and Discussions

Moving Train in Calm Water Condition

The numerical results generated by the developed program for a moving train are compared with those calculated from the commercial program, OrcaFlex, in a calm water condition. In OrcaFlex and the developed program, the same simplified approach has been devised to simulate the effect of the moving vehicle on the dynamic responses of the tunnel by adding the mass of the vehicle to the mass of the tunnel in the location through which the vehicle passes at each time step. The effects of the gravitational and inertial forces generated by the vehicle can be simulated using the simplified approach (Orcaflex and CHARM3D-V1). However, the full tunnel-mooring-vehicle interaction can only be calculated by the presently developed fully-coupled CHARM3D-V2 program. The vertical response of the tunnel and the mooring tension are analyzed at varying vehicle speeds.

Figure 89 shows the envelopes of tunnel's vertical displacements when the vehicle speed is 80m/s. The 3 results agree well, which means that the simplified approach can be used when calculating the effects of the moving vehicle on tunnel dynamics. Figures 90-91 show the time histories of tunnel's vertical responses and mooring tensions (Line #4) at different tunnel locations of ± 175 m and 0 m. As shown in Figure 89, the envelope shows that the vertical response of the tunnel is the largest at the tunnel locations of ± 175 m and generally large between them. In addition, as shown in Figure 90, the time histories of tunnel's vertical responses at 3 positions also coincide well between the present simulation program and OrcaFlex. In the case of mooring tension, there is a slight difference (less than 0.2% of total tension) in static-tension magnitude, but the general trend of the dynamic tension is the same. The slight difference in static mooring tension can be attributed to the slight different boundary conditions at both ends of the tunnel between the two computer programs. For the mooring program, Orcaflex used lumped mass method while CHARM3D used high-order rod FE elements

Figures 92-93 show tunnel's vertical responses and dynamic mooring tensions (Line #4) as a function of vehicle velocity in the tunnel's horizontal locations of -175 m and 0 m. As the vehicle velocity increases, tunnel's downward motions become larger. The corresponding negative dynamic tensions also slightly increase so that the total (static+dynamic) tensions become slightly decreased. While the vehicle's gravitational force is dominant in this case, the variation with speed is due to vehicle's different inertial forces. At the high train velocity, the vertical motions of the tunnel vary fast, which causes large acceleration of the vehicle, i.e., the large inertial force by the moving train.

Considering the magnitude of the downward motion of 2.1mm induced by the moving vehicle, it can be concluded that wave and seismic excitations are much more important when checking the safety and performance of SFT than moving train (Jin and Kim, 2018). The simplified interaction model also provides good results when considering the effects of moving train on SFT. However, when the coupled effects of the tunnel-mooring-train system on the vehicle's operation (passengers' safety and comfort), the present full interaction model is needed.

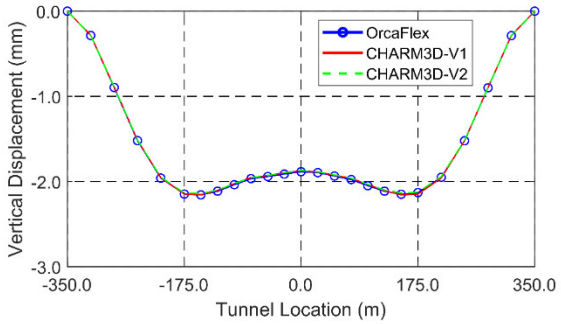

Figure 89. The envelope of tunnel's vertical displacements at vehicle velocity of 80 m/s (OrcaFlex: OrcaFlex results with the simplified approach, CHARM3D-V1: results by the developed program with the simplified approach, CHARM3D-V2: results by the developed program with the full tunnel-mooring-vehicle-interaction method).

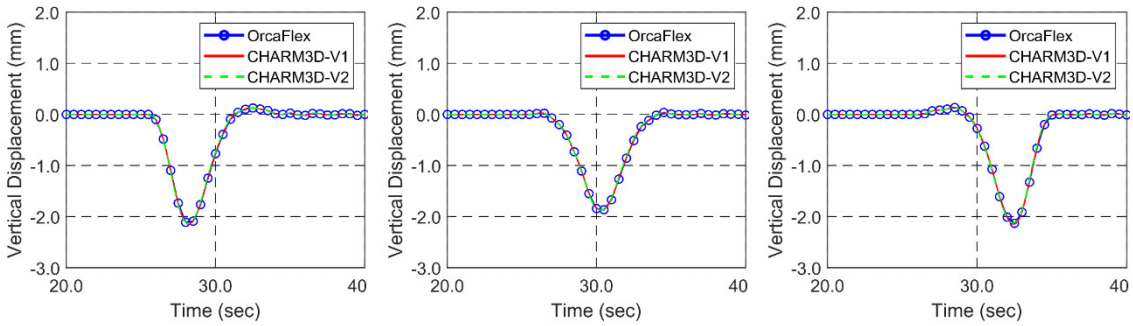

(a) (b) (c)

Figure 90. Time histories of tunnel's vertical displacements in the horizontal locations of -175 m (a), 0 m (b), and 175 m (c) at the vehicle velocity of 80 m/s.

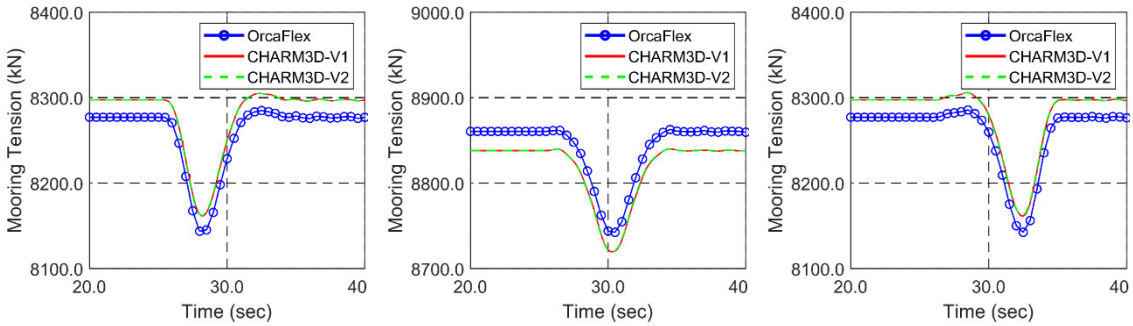

(a) (b) (c)

Figure 91. Time histories of mooring tensions (Line #4) in the horizontal locations of -175 m (a), 0 m (b), and 175 m (c) at the vehicle velocity of 80 m/s.

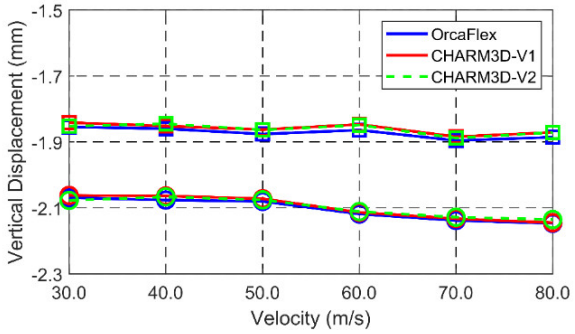

Figure 92. Tunnel's vertical displacements in two horizontal locations of -175 m (circle) and 0 m (square) with varying vehicle velocities.

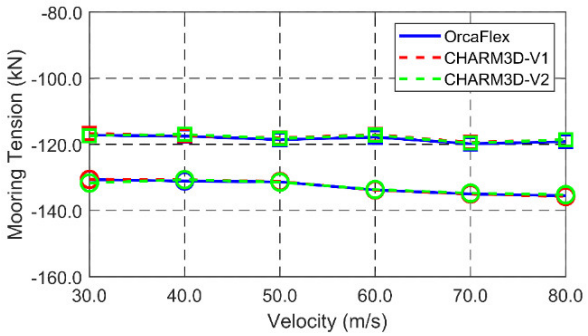

Figure 93. Dynamic mooring tensions (Line #4) in two horizontal locations of -175 m (circle) and 0 m (square) with varying vehicle velocities.

Dynamic Responses of the SFT under Wave or Seismic Excitations

As discussed in the previous section, moving vehicles can cause the dynamics of SFT, and thus it is necessary to understand their coupling effects under a given environmental condition. Figures 94-99 show the time histories of tunnel's horizontal/vertical responses and the mooring tension (Line #4) in the middle location under wave excitations with and without moving vehicles. The corresponding spectra are also given. The first train passes through the middle location of the tunnel in 150 sec, and a total of 4 trains pass through the tunnel with a 5-minute interval during the 20-minute simulation period. The time histories and spectra of tunnel's horizontal motions show no apparent effect by the moving trains, which means that horizontal interaction force is very small, as expected. On the other hand, in the vertical direction, the repeating downward motions of the tunnel occur by the moving vehicles. Its effect can more clearly be seen in the corresponding spectrum, where the train operation additionally induces the low-frequency motions while the wave-frequency part remains the same, as shown in Figure

97. The above effect also slightly increases the mooring tension in the low-frequency region, as shown in Figures 98-99. Since fixture towers fix both ends of the tunnel, the horizontal and vertical tunnel responses given in Figures 94-97 are tunnel's hydro-elastic responses.

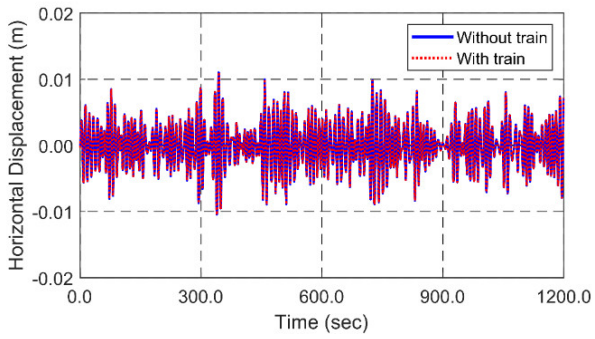

Figure 94. Time histories of tunnel's horizontal displacement in the middle location under wave excitations with (dashed line) and without (solid line) moving vehicles.

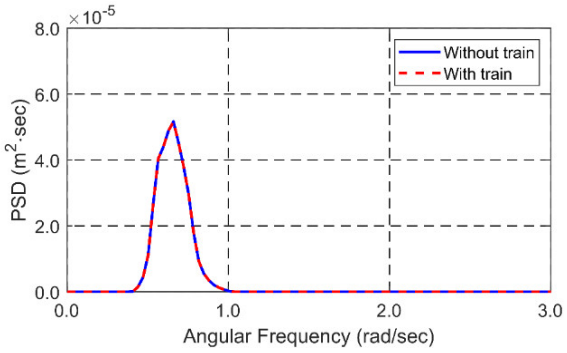

Figure 95. Spectra of tunnel's horizontal displacement in the middle location under wave excitations with (dashed line) and without (solid line) moving vehicles.

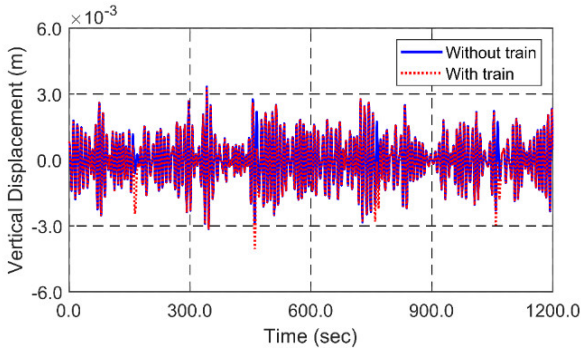

Figure 96. Time histories of tunnel's vertical displacement in the middle location under wave excitations with (dashed line) and without (solid line) moving vehicles.

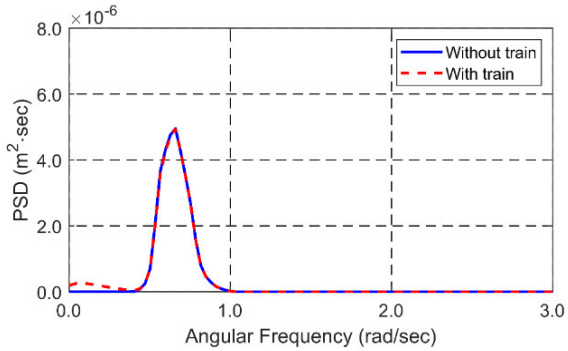

Figure 97. Spectra of tunnel's vertical displacement in the middle location under wave excitations with (dashed line) and without (solid line) moving vehicles.

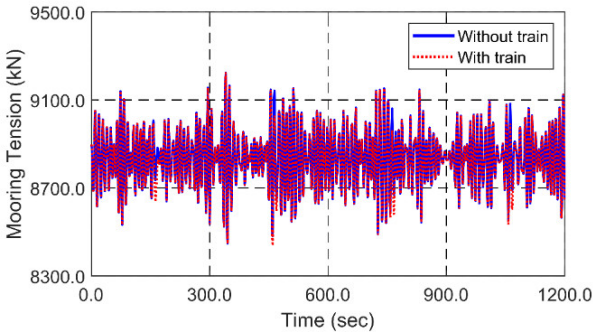

Figure 98. Time histories of mooring tension in the middle location under wave excitations with (dashed line) and without (solid line) moving vehicles.

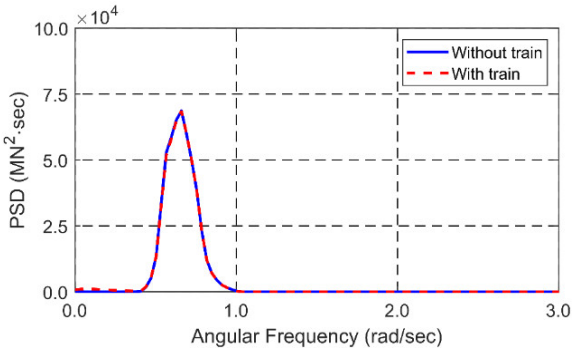

Figure 99. Spectra of mooring tension in the middle location under wave excitations with (dashed line) and without (solid line) moving vehicles.

Figures 100-105 show the time histories and spectra of tunnel's horizontal/vertical responses and mooring tension (Line #4) in the seismic-excitation condition. Since the earthquake occurs only for 140 seconds, the simulation period of the seismic excitation case is 150 seconds. During that period, it is set that only a moving train passes through the middle location of the tunnel in 78 sec. As shown in Figures 100-101, the horizontal responses of the tunnel with and without moving vehicle are the same since the horizontal interaction force is much smaller than the seismic-induced horizontal force transmitted through mooring lines. As shown in Figures 100-105, the horizontal/vertical responses of the tunnel and the mooring tension under the seismic excitations are larger than those in the previous wave condition. Therefore, the relative importance of the downward motion induced by the moving vehicle is relatively small even in the vertical direction as compared to the previous wave case, as shown in Figures 102-103. The mooring tension reflects the results of horizontal/vertical motions of the tunnel; thus, there is little difference whether the train is operated or not. In Figures 100-101, a large peak in the horizontal tunnel motion at its lowest wet natural frequency (1.92 rad/s) is noticed since

the earthquake excitation is more like a sudden transient loading. Minor peaks in the high-frequency region of Figures 100-105 are due to higher wet natural frequencies (see Table 9). The horizontal and vertical tunnel responses given in Figures 100-103 are the sum of tunnel's hydro-elastic responses and seismic movements.

As mentioned before, the safety of mooring lines is determined by comparing the maximum tension with the MBL divided by SF. The MBL for R5 grade chain is 30,689 kN, and the safety factor is 1.67 (API, 1996). The maximum mooring tension under the seismic excitation is 11,000 kN and still smaller than the allowable tension (MBL/SF) of 18,400 kN. To sum up, the influence of moving trains on the design of the SFT system is very minor compared to wave and earthquake effects for the present case of large-size SFT. However, as the SFT size decreases, the relative importance of moving trains is expected to increase.

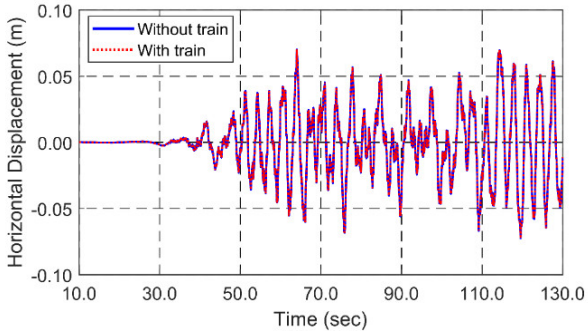

Figure 100. Time histories of tunnel's horizontal displacement in the middle location under seismic excitations with and without moving vehicles.

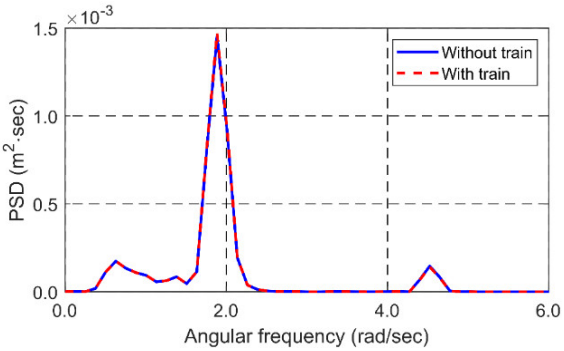

Figure 101. Spectra (b) of tunnel's horizontal displacement in the middle location under seismic excitations with and without moving vehicles.

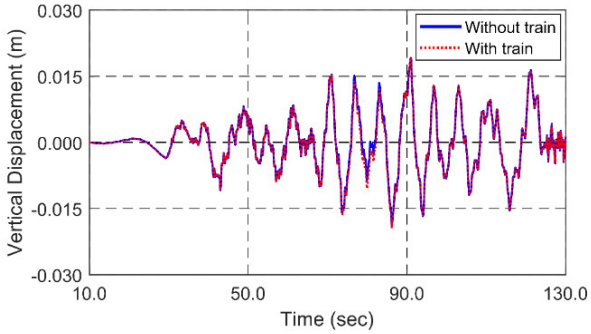

Figure 102. Time histories of tunnel's vertical displacement in the middle location under seismic excitations with and without moving vehicles.

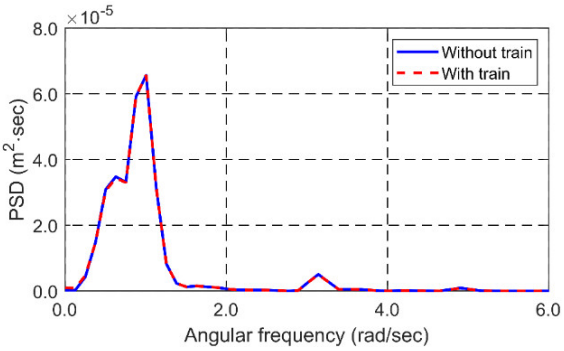

Figure 103. Spectra of tunnel's vertical displacement in the middle location under seismic excitations with and without moving vehicles.

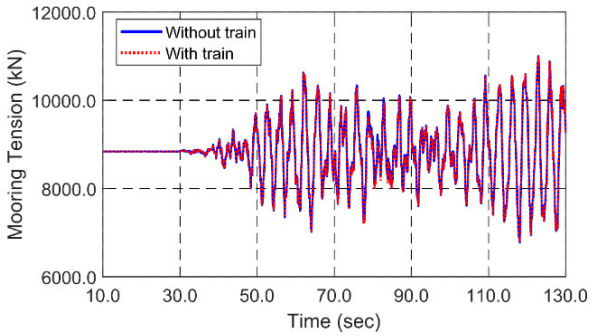

Figure 104. Time histories of mooring tension (Line #4) in the middle location under seismic excitations with and without moving vehicles.

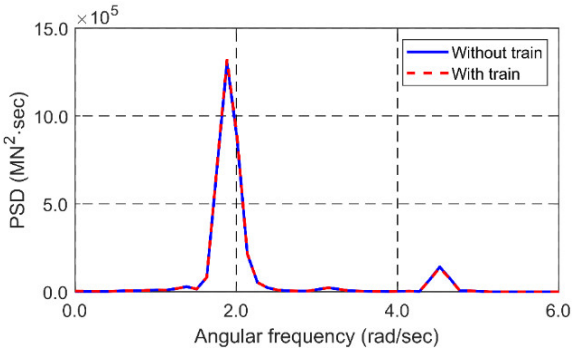

Figure 105. Spectra of mooring tension (Line #4) in the middle location under seismic excitations with and without moving vehicles.

Dynamic Responses of Vehicle under Wave or Seismic Excitations

In the previous sections, the simulation results clearly show that moving vehicles little influence the dynamic responses of the tunnel regardless of their speeds. Even if there are downward motions caused by vehicles, its magnitude is much smaller than the motions induced by waves or earthquakes. However, the effects of SFT motions on moving vehicles can be important in view of passengers' safety and comfort. Therefore, through the present fully-coupled dynamic analysis, the dynamics of the vehicle are further investigated in detail in this section. In particular, the derailment factor, offload factor, and

riding-comfort criterion are evaluated to determine the safety and comfort of passengers quantitatively.

Figures 106-107 show the time histories of the sway motion of the first wheel-set attached to the first car-body and the track under wave and seismic excitations. The horizontal interaction force, which is calculated by using the simplified Kalker creep theory, is a function of the relative velocity between the track and the vehicle. In this case, the vehicle should follow the track well under wave or seismic excitations, as represented in Figures 106-107. The high-frequency motion is largely affected by the track irregularity while wave and seismic excitations cause relatively lower-frequency motions.

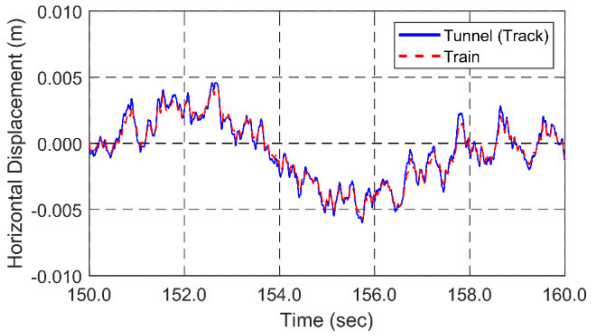

Figure 106. Time histories of the sway motion of the first wheel-set attached to the first car-body and the track under wave excitations (train speed= 80m/s).

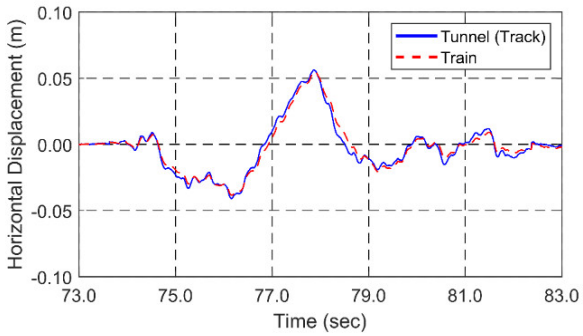

Figure 107. Time histories of the sway motion of the first wheel-set attached to the first car-body and the track under seismic excitations (train speed= 80m/s).

Figures 108-109 show the time histories of the horizontal and vertical wheel-rail forces of the first, left wheel attached to the first car-body under wave or seismic excitations. The horizontal and vertical wheel-rail forces in the high-frequency range are affected by track irregularity. Moreover, the vertical wheel-rail force is much larger than the horizontal one because the static wheel-rail force induced by the gravitational force of the vehicle is dominant. The vertical wheel-rail forces under wave or seismic excitations are similar by the same reason. On the other hand, the horizontal force on the vehicle induced by the seismic excitation is larger than that by wave excitations.

Two important factors are generally introduced to check the safety of the vehicle, i.e., the derailment factor and the offload factor. The derailment factor is defined as the horizontal wheel-rail force, Q_i, divided by the vertical wheel-rail force, P_i, acting on a left or right wheel as follows (Dimitrakopoulos and Zeng, 2015; Guo et al., 2013):

$$Derailment\ Factor = \frac{Q_i}{P_i}, \quad i = \{L, R\} \tag{172}$$

In addition, as presented in the following equation, the offload factor is defined as the absolute difference between vertical wheel-rail forces acting on the left and right wheels divided by the summation of the vertical wheel-rail forces (Dimitrakopoulos and Zeng, 2015; Guo et al., 2013). Each country has their own criteria. In the case of Korea, the allowable derailment and offload factors are 0.8 (Hwang, 2015).

$$Offload\ Factor = \frac{|P_L - P_R|}{P_L + P_R} \tag{173}$$

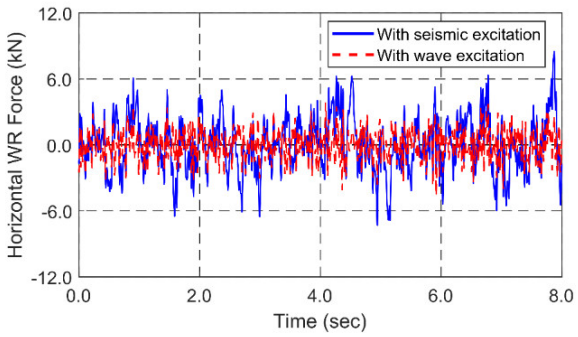

Figure 108. Time histories of the horizontal wheel-rail forces of the first, left wheel attached to the first car-body under wave (dashed line) and seismic (solid line) excitations (train speed= 80m/s).

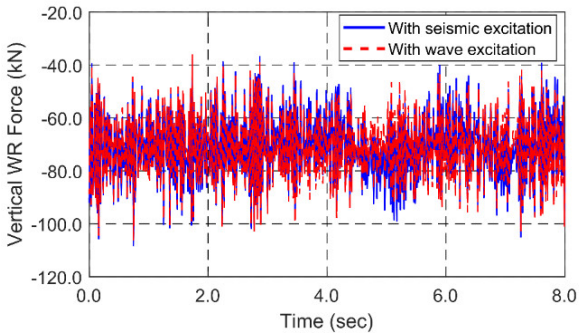

Figure 109. Time histories of the vertical wheel-rail forces of the first, left wheel attached to the first car-body under wave (dashed line) and seismic (solid line) excitations (train speed= 80m/s).

Figures 110-111 show the derailment factor and the offload factor with varying vehicle speeds from 30 m/s to 80 m/s. In addition, as mentioned before, in the case of wave excitation, a total of 4 moving trains are operated during the 20-minute simulation period with a 5-minute interval. On the other hand, in the case of seismic excitation, a 150-second simulation is conducted with one moving train passing through the middle location of the tunnel at 78 sec. Then, from the respective simulations, the maximal values are presented in Figures 110-111. Generally, the derailment factor and offload factor increase with increasing vehicle speed both in wave and earthquake conditions. At high vehicle velocity, the fluctuations of the vehicle/tunnel and track irregularities are generally large. In this case, the large variations of horizontal and vertical wheel-rail forces increase the possibility of the high derailment and offload factors. For the given wave and earthquake conditions, the derailment factor of the latter is larger when considering an identical vehicle and its speed. It is because of large high-frequency variations of the horizontal motion of the tunnel, which increase the horizontal wheel-rail force, as shown in Figure

110. Whereas, the vertical wheel-rail force is similar for both wave and seismic cases. The similar vertical wheel-rail force also leads to the similar offload factor at the same vehicle speed. The maximum derailment and offload factors are 0.25 and 0.55 at the speed of 80 m/s, respectively, which are smaller than the criteria of Korea. However, the general trend is that both factors increase with train speed, so more care is needed when the train speed is much higher than 80m/s. At any rate, the previous analyses demonstrate that the operation of the high-speed train is feasible even for SFTs under typical wave and seismic excitations below extreme survival conditions. Of course, more intensive research needs to be completed to understand the whole system better and improve the reliability of the train operation through SFTs.

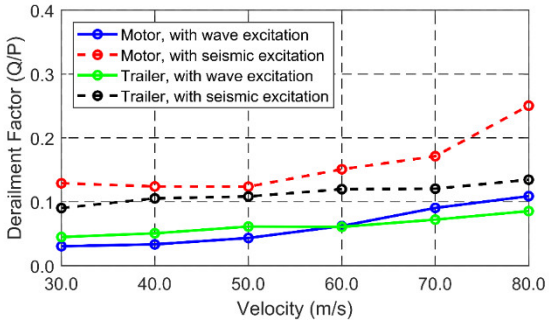

Figure 110. Derailment factor with varying vehicle speeds from 30 m/s to 80 m/s.

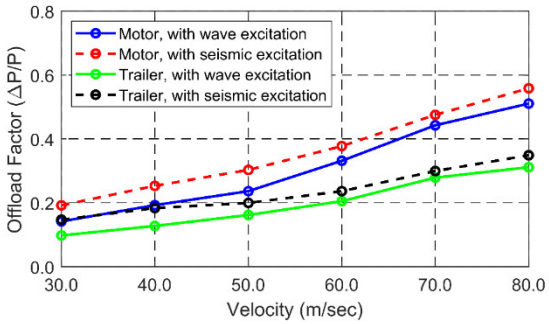

Figure 111. Offload factor with varying vehicle speeds from 30 m/s to 80 m/s.

Finally, the vehicle's riding comfort is another important issue. It is usually determined by looking at the sway/heave accelerations of the train, i.e. sway and heave accelerations of the car-body should be smaller than 0.1 g and 0.13 g, respectively, based on Chinese code (Dimitrakopoulos and Zeng, 2015). The criterion is selected in the present study. Figures 112-113 show the time histories of sway (horizontal) and heave (vertical) accelerations of the first car-body with the velocity of 80 m/s. The absolute maximum values of the horizontal and vertical accelerations under the seismic excitation are 0.84 m/s^2 (0.086 g) and 0.60 m/s^2 (0.061 g), which satisfy the criteria of the high-speed vehicle. The absolute maximum values are even smaller for the wave case. The wave case is more relevant in the case of passengers' comfort since it persists for a long time, while earthquakes are transient for a very short time.

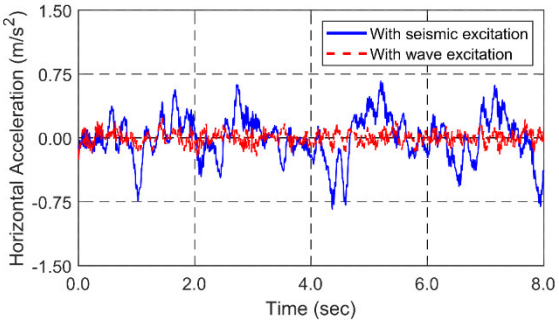

Figure 112. Time histories of sway accelerations of the first car-body at the speed of 80 m/s.

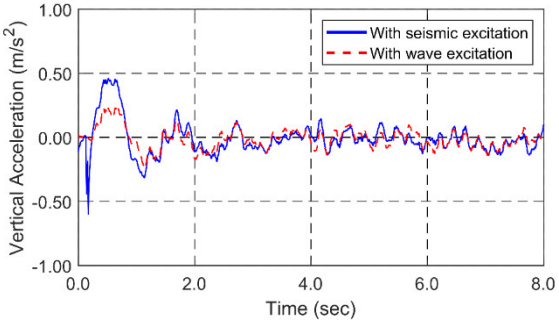

Figure 113. Time histories of heave accelerations of the first car-body at the speed of 80 m/s.

CHAPTER IV

CONCLUSIONS

Conclusions for CHAPTER II

In this study, the performance of the SR-WEC that utilizes the pitch motion induced by ocean waves is evaluated through numerical simulations. A numerical model of two bodies, which consists of a floating body (cylinder) equipped with the armature assembly and the magnet assembly, is developed, and their interaction force is also calculated to couple the objects. Besides, a single point mooring (SPM) is also modeled and connected to the outer cylinder for the station-keeping purpose. The numerical model is verified by comparing the results with experimental ones. The sliding performance of the magnet assembly is compared with 2-DOF-actuator tests, and displacement and velocity trends are in good agreement. The maximum velocity in the numerical simulation is approximately 10 % higher than the experiment for 2-DOF-actuator tests. The power calculation scheme is also verified with previous experimental results, and the maximum difference of power output is only -5.3 % among eight sea states. After verifications, the frequency-domain analysis is conducted to calculate wave forces and moments on the floating body, to obtain added masses and moments, radiation damping coefficients, and hydrostatic restoring coefficients for the time-domain analysis. In the time-domain analysis, a SPM is coupled with the floating body, and the generator dynamics is also considered. The two-body interaction is considered by computing the magnetic force between the magnet and armature assemblies and considering conservation of momentum

at both ends. The parametric study is conducted to find out the optimum condition. Optimum values of the load resistance, the magnitude of the magnetic force, the sliding length are dependent on the wave condition. The higher coefficient of restitution and mass of the magnet assembly result in higher power output. Under the optimum system parameters, average power outputs are obtained at different wave conditions. Higher wave height and smaller wave period contribute to higher power output. Peak average power output for prototype WEC is 1.31 kW at a significant wave height of 3.5 m and a peak period of 5 sec. In order to maximize power output, the pitch natural frequency can be rearranged, and a control system to adjust the natural frequency can be used such as the movable ring mass.

Conclusions for CHAPTER III

In the Case Study I, global performance analysis of the SFT was carried out for survival random wave and seismic excitations. To solve tunnel-mooring coupled hydro-elastic responses, an in-house time-domain- simulation computer program was developed. The hydro-elastic equation of motion for the tunnel and mooring was based on rod-theory-based finite element formulation with Galerkin method. The dummy-connection-mass method was devised to conveniently connect multiple segmented objects and mooring lines with linear and rotational springs. Considering the slender shape of the structure, hydrodynamic forces were computed by the modified Morison equation. The numerical results produced by the developed program were in good agreement with those by the commercial program OrcaFlex based on lumped-mass method. The differences in the

maximum values of horizontal and vertical motions under wave excitations are -2.2 % and 3.1 % while those under real seismic excitations are -6.9 % and 4.9 %. The extreme wave excitations caused the maximum SFT dynamic motions of 24 cm and 6 cm in the horizontal and vertical directions and the corresponding mooring tensions below the allowable level. Snap motions and loadings of mooring lines were not observed. Under regular seismic excitations, large resonant responses of the tunnel were observed at first and third natural frequencies. In the case of seabed earthquake, the seabed motions are transferred to SFT through mooring lines and through seawater fluctuations called seaquake. When the latter is further considered, horizontal responses were not affected but vertical responses become significantly reduced especially at its lowest natural frequency. After analyzing the behaviors of the two contributions, it was found that the reduction was caused by the phase-cancellation effect. However, in other cases, the phases could enhance each other to increase the total responses of the SFT. Under extreme irregular seismic excitations, the maximum SFT dynamic motions of 7 cm and 2 cm were generated and the corresponding mooring tensions were about 30% smaller compared to the extreme wave case. However, when the frequencies of seismic excitations are closer to SFT natural frequencies, larger dynamic amplifications are expected.

In Case Study II, tunnel-mooring-vehicle fully-coupled dynamic analyses are conducted under wave or seismic excitations. The rod FE theory is used to develop the tunnel and mooring-line dynamics, which is same as the Case Study I. A train moving with constant speed along the SFT is modeled by using the seven-rigid-body-element dynamic method. The interaction between the tunnel and the vehicle is analyzed by using

the correspondence assumption and the simplified Kalker creep theory. In the case of moving train in a calm water condition, the numerical results of the developed program are satisfactorily compared with those of the commercial program, OrcaFlex. The magnitudes of downward motions by the moving train with various speeds are obtained, which is about the order of 2 mm and not sensitive to train speed. The horizontal responses of the tunnel are little influenced by the tunnel-vehicle interaction under wave and seismic excitations whereas there are small but some influences on vertical responses and mooring tensions. Their magnitudes are much smaller than the motions of the tunnel by wave and seismic excitations. In addition, several safety and comfort criteria of the vehicle are evaluated under wave or seismic excitations by using the newly developed tunnel-train-mooring fully-coupled dynamic simulation program. For the given earthquake and train speed, the maximum derailment factor and offload factor are 0.25 and 0.55, respectively, and the maximum horizontal and vertical accelerations of the car-body are 0.086 g and 0.061 g, which satisfy the typical safety and comfort criteria. However, the general trend of the derailment and offload factors increases with train speed, so more care is needed when the train speed is much higher than 80m/s. The influence of moving trains on the structural robustness of SFT system is very minor compared to wave and earthquake effects for the present case of large-size SFT. However, as the SFT size decreases, the relative importance of moving trains is expected to increase. The present investigations based on the newly developed numerical-simulation tool support that the high-speed train is feasible to be used for the SFT under reasonable wave and seismic excitations.

REFERENCES

API, 1996. Recommended practice for design and analysis of stationkeeping systems for floating structures: exploration and production department. API recommended practice 2SK (RP 2SK): Effective Date: March 1, 1997. *American Petroleum Institute*.

Bae, YH, 2013. Coupled Dynamic Analysis of Multiple Unit Floating Offshore Wind Turbine.

Baker, N, Mueller, MA, 2001. Direct drive wave energy converters, Rev. Energ. Ren.: Power Engineering, pp. 1-7.

Chen, Z, Xiang, Y, Lin, H, and Yang, Y, 2018. Coupled vibration analysis of submerged floating tunnel system in wave and current. *Applied Sciences* 8 (8), 1311.

Cifuentes, C, Kim, S, Kim, M, and Park, W, 2015. Numerical simulation of the coupled dynamic response of a submerged floating tunnel with mooring lines in regular waves. *Ocean Systems Engineering* 5 (2), 109-123.

Di Pilato, M, Perotti, F, and Fogazzi, P, 2008. 3D dynamic response of submerged floating tunnels under seismic and hydrodynamic excitation. *Engineering structures* 30 (1), 268-281.

Dimitrakopoulos, EG, Zeng, Q, 2015. A three-dimensional dynamic analysis scheme for the interaction between trains and curved railway bridges. *Computers & structures* 149, 43-60.

Dinh, VN, Kim, KD, and Warnitchai, P, 2009. Dynamic analysis of three-dimensional bridge–high-speed train interactions using a wheel–rail contact model. *Engineering structures* 31 (12), 3090-3106.

Drew, B, Plummer, AR, and Sahinkaya, MN, 2009, A review of wave energy converter technology,

Engebretsen, KB, Jakobsen, KK, Haugerud, SA, and Minoretti, A, 2017. A Submerged Floating Tube Bridge Concept for the Bjørnafjord Crossing: Marine Operations, ASME 2017 36th International Conference on Ocean, Offshore and Arctic Engineering. *American Society of Mechanical Engineers*, pp. V07BT06A027-V007BT006A027.

Faggiano, B, Landolfo, R, and Mazzolani, F, 2001. Design and modelling aspects concerning the submerged floating tunnels: an application to the Messina Strait crossing. *Krobeborg. Strait Crossing*, 511-519.

Faggiano, B, Landolfo, R, and Mazzolani, F, 2005. The SFT: an innovative solution for waterway strait crossings, IABSE Symposium Report. *International Association for Bridge and Structural Engineering*, Lisbon, Portugal, pp. 36-42.

Faltinsen, O, 1993. Sea loads on ships and offshore structures. *Cambridge university press*, London, UK.

Fazal, I, Karsiti, MN, Zulkifli, SA, Ibrahim, T, and Rao, KR, 2010. Modeling and simulation of a moving-coil linear generator, 2010 International Conference on Intelligent and Advanced Systems. *IEEE*, pp. 1-5.

Fu, S, Cui, W, 2012. Dynamic responses of a ribbon floating bridge under moving loads. *Marine Structures* 29 (1), 246-256.

Fujii, T, 1996. Submerged floating tunnels project in Funka Bay design and execution, International Conference on Submerged Floating Tunnel. *Sandnes, Norway*.

Gao, Y, Shao, S, Zou, H, Tang, M, Xu, H, and Tian, C, 2016. A fully floating system for a wave energy converter with direct-driven linear generator. *Energy* 95, 99-109.

Garrett, D, 1982. Dynamic analysis of slender rods. *Journal of energy resources technology* 104 (4), 302-306.

Ge, F, Lu, W, Wu, X, and Hong, Y, 2010. Fluid-structure interaction of submerged floating tunnel in wave field. *Procedia engineering* 4, 263-271.

Ghimire, A, Prakash, O, 2017. Intangible Study for the Design and Construction of Submerged Floating Tunnel. *Imperial Journal of Interdisciplinary Research* 3 (4), 721-724.

Goldemberg, J, 2000. World energy assessment: Energy and the challenge of sustainability. *United Nations Pubns*.

Guo, W, Xia, H, and Zhang, N, 2013. Dynamic responses of Tsing Ma Bridge and running safety of trains subjected to Typhoon York. *International Journal of Rail Transportation* 1 (3), 181-192.

Han, JS, Won, B, Park, W-S, and Ko, JH, 2016. Transient response analysis by model order reduction of a Mokpo-Jeju submerged floating tunnel under seismic excitations. *Struct. Eng. Mech* 57, 921-936.

Herzog, AV, Lipman, TE, and Kammen, DM, 2001, Renewable energy sources,

Hong, Y, Ge, F, and Lu, W, 2016. On the two essential concepts for SFT: synergetic buoyancy-weight ratio and slack-taut map. *Procedia engineering* 166, 221-228.

Hwang, SH, 2015. Evaluation of train runnability on bridges considering train/track/wind interaction. *PhD Dissertation submitted to Seoul National University*.

Islam, N, Ahrnad, S, 2003. Nonlinear seismic response of articulated offshore tower. *Defence Science Journal* 53 (1), 105-113.

Jin, C, Kim, M-H, 2018. Time-domain hydro-elastic analysis of a SFT (submerged floating tunnel) with mooring lines under extreme wave and seismic excitations. *Applied Sciences* 8 (12), 2386.

Jin, C, Kim, M, 2017. Dynamic and structural responses of a submerged floating tunnel under extreme wave conditions. *OCEAN SYSTEMS ENGINEERING-AN INTERNATIONAL JOURNAL* 7 (4), 413-433.

Jin, C, Lee, J, Kim, H, and Kim, M, 2017. Dynamic Responses of a Submerged Floating Tunnel in Survival Wave and Seismic Excitations, The 27th International Ocean and Polar Engineering Conference. *International Society of Offshore and Polar Engineers*, San Francisco, USA, pp. 547-551.

Kim, J, Koh, H, Cho, I, Kim, M, and Kweon, H, 2017. Experimental study of wave energy extraction by a dual-buoy heaving system. *International Journal of Naval Architecture and Ocean Engineering* 9 (1), 25-34.

Kim, M, Koo, B, Mercier, R, and Ward, E, 2005. Vessel/mooring/riser coupled dynamic analysis of a turret-moored FPSO compared with OTRC experiment. *Ocean Engineering* 32 (14-15), 1780-1802.

Kunisu, H, Mizuno, S, Mizuno, Y, and Saeki, H, 1994. Study on submerged floating tunnel characteristics under the wave condition, The Fourth International Offshore and Polar Engineering Conference. *International Society of Offshore and Polar Engineers*, Osaka, Japan, pp. 27-32.

Lee, J, Jin, C, and Kim, M, 2017. Dynamic response analysis of submerged floating tunnels by wave and seismic excitations. *OCEAN SYSTEMS ENGINEERING-AN INTERNATIONAL JOURNAL* 7 (1), 1-19.

Lee, JH, Seo, SI, and Mun, HS, 2016. Seismic behaviors of a floating submerged tunnel with a rectangular cross-section. *Ocean Engineering* 127, 32-47.

Lejerskog, E, Boström, C, Hai, L, Waters, R, and Leijon, M, 2015. Experimental results on power absorption from a wave energy converter at the Lysekil wave energy research site. *Renewable Energy* 77, 9-14.

Lin, H, Xiang, Y, Yang, Y, and Chen, Z, 2018. Dynamic response analysis for submerged floating tunnel due to fluid-vehicle-tunnel interaction. *Ocean Engineering* 166, 290-301.

Long, X, Ge, F, and Hong, Y, 2015. Feasibility study on buoyancy–weight ratios of a submerged floating tunnel prototype subjected to hydrodynamic loads. *Acta Mechanica Sinica* 31 (5), 750-761.

Long, X, Ge, F, Wang, L, and Hong, Y, 2009. Effects of fundamental structure parameters on dynamic responses of submerged floating tunnel under hydrodynamic loads. *Acta Mechanica Sinica* 25 (3), 335-344.

López, I, Andreu, J, Ceballos, S, de Alegría, IM, and Kortabarria, I, 2013. Review of wave energy technologies and the necessary power-equipment, Renewable and Sustainable Energy Reviews, pp. 413-434.

Lu, W, Ge, F, Wang, L, Wu, X, and Hong, Y, 2011. On the slack phenomena and snap force in tethers of submerged floating tunnels under wave conditions. *Marine Structures* 24 (4), 358-376.

Martinelli, L, Barbella, G, and Feriani, A, 2011. A numerical procedure for simulating the multi-support seismic response of submerged floating tunnels anchored by cables. *Engineering structures* 33 (10), 2850-2860.

Martinelli, L, Domaneschi, M, and Shi, C, 2016. Submerged floating tunnels under seismic motion: vibration mitigation and seaquake effects. *Procedia engineering* 166, 229-246.

Mazzolani, F, Landolfo, R, Faggiano, B, Esposto, M, Perotti, F, and Barbella, G, 2008. Structural analyses of the submerged floating tunnel prototype in Qiandao Lake (PR of China). *Advances in structural engineering* 11 (4), 439-454.

Miles, LF, 2017. A Permanent-Magnet Linear Generator Wave Energy Converter for Low Power Ocean Sensors.

Mirzapour, J, Shahmardani, M, and Tariverdilo, S, 2017. Seismic response of submerged floating tunnel under support excitation. *Ships and Offshore Structures* 12 (3), 404-411.

Morison, J, Johnson, J, and Schaaf, S, 1950. The force exerted by surface waves on piles. *Journal of Petroleum Technology* 2 (05), 149-154.

Mork, G, Barstow, S, Kabuth, A, and Pontes, MT, 2010. Assessing the Global Wave Energy Potential, pp. 447-454.

Mousavi, SA, Bargi, K, and Zahrai, SM, 2013. Optimum parameters of tuned liquid column–gas damper for mitigation of seismic-induced vibrations of offshore jacket platforms. *Structural Control and Health Monitoring* 20 (3), 422-444.

Muhammad, N, Ullah, Z, and Choi, D-H, 2017. Performance evaluation of submerged floating tunnel subjected to hydrodynamic and seismic excitations. *Applied Sciences* 7 (11), 1122.

Orcina, 2018. OrcaFlex Manual,

Paik, IY, Oh, CK, Kwon, JS, and Chang, SP, 2004. Analysis of wave force induced dynamic response of submerged floating tunnel. *KSCE Journal of Civil Engineering* 8 (5), 543-550.

Park, S-S, Park, SM, Jung, J, and Kim, JH, 2013. Analysis and experiments of the linear electrical generator in wave energy farm utilizing resonance power buoy system. *Journal of Magnetics* 18 (3), 250-254.

Parthasarathy, R, 2012. Linear PM Generator for Wave Energy Conversion. *Louisiana State University*.

Prudell, J, 2007. Novel design and implementation of a permanent magnet linear tubular generator for wave energy conversion. *MS thesis, Oregon State University, Corvallis, OR*.

Prudell, J, Stoddard, M, Amon, E, Brekken, TKA, and von Jouanne, A, 2010. A Permanent-Magnet Tubular Linear Generator for Ocean Wave Energy Conversion. *Ieee Transactions on Industry Applications* 46 (6), 2392-2400.

Ran, Z, 2000. Coupled dynamic analysis of floating structures in waves and currents.

Ran, Z, Kim, M, and Zheng, W, 1999. Coupled dynamic analysis of a moored spar in random waves and currents (time-domain versus frequency-domain analysis). *Journal of Offshore Mechanics and Arctic Engineering* 121 (3), 194-200.

Remseth, S, Leira, BJ, Okstad, KM, Mathisen, KM, and Haukås, T, 1999. Dynamic response and fluid/structure interaction of submerged floating tunnels. *Computers & structures* 72 (4-5), 659-685.

Rhinefrank, K, Agamloh, E, von Jouanne, A, Wallace, A, Prudell, J, Kimble, K, Aills, J, Schmidt, E, Chan, P, and Sweeny, B, 2006. Novel ocean energy permanent magnet linear generator buoy. *Renewable Energy* 31 (9), 1279-1298.

Salcher, P, Pradlwarter, H, and Adam, C, 2016. Reliability assessment of railway bridges subjected to high-speed trains considering the effects of seasonal temperature changes. *Engineering structures* 126, 712-724.

Seo, S-i, Mun, H-s, Lee, J-h, and Kim, J-h, 2015. Simplified analysis for estimation of the behavior of a submerged floating tunnel in waves and experimental verification. *Marine Structures* 44, 142-158.

Shixiao, F, Weicheng, C, Xujun, C, and Cong, W, 2005. Hydroelastic analysis of a nonlinearly connected floating bridge subjected to moving loads. *Marine Structures* 18 (1), 85-107.

Skorpa, L, 1989. Innovative norwegian fjord crossing. How to cross the Høgsjord, alternative methods, Proceedings of the 2nd Congress AIOM (Marine and Offshore Engineering Association), Naples, Italy, pp. 15-17.

Song, M-K, Noh, H-C, and Choi, C-K, 2003. A new three-dimensional finite element analysis model of high-speed train–bridge interactions. *Engineering structures* 25 (13), 1611-1626.

Stelzer, M, Joshi, R, 2012. Evaluation of wave energy generation from buoy heave response based on linear generator concepts. *Journal of Renewable and Sustainable Energy* 4 (6), 063137.

Suh, K-D, Kwon, H-D, and Lee, D-Y, 2010. Some statistical characteristics of large deepwater waves around the Korean Peninsula. *Coastal Engineering* 57 (4), 375-384.

Tariverdilo, S, Mirzapour, J, Shahmardani, M, Shabani, R, and Gheyretmand, C, 2011. Vibration of submerged floating tunnels due to moving loads. *Applied Mathematical Modelling* 35 (11), 5413-5425.

Thompson, N, 1980. Mean forces, pressure and flow field velocities for circular cylindrical structures: single cylinder with two-dimensional flow. *EDU Data Item* 80025.

USGS, 2018. National strong-motion project earthquake data sets, United States Geological Survey.

Veritas, DN, 2009. Offshore standard DNV-OS-E302: offshore mooring chain. *Det Norske Veritas (DNV) Oslo*.

Veritas, DN, 2010. Offshore standard DNV-OS-E301: Offshore standard-position mooring. *Det Norske Veritas (DNV) Oslo*.

Veritas, N, 2000. Environmental conditions and environmental loads. *Det Norske Veritas*.

Wu, Z, Ni, P, and Mei, G, 2018. Vibration response of cable for submerged floating tunnel under simultaneous hydrodynamic force and earthquake excitations. *Advances in structural engineering* 21, 1761-1773.

Xia, H, Zhang, N, 2005. Dynamic analysis of railway bridge under high-speed trains. *Computers & Structures* 83 (23-24), 1891-1901.

Xia, H, Zhang, N, and Guo, W, 2017. Dynamic interaction of train-bridge systems in high-speed railways: theory and applications. *Springer*.

Xiao, J, Huang, G, 2010. Transverse earthquake response and design analysis of submerged floating tunnels with various shore connections. *Procedia engineering* 4, 233-242.

Yuan, Z, Man-sheng, D, Hao, D, and Long-chang, Y, 2016. Displacement Response of Submerged Floating Tunnel Tube Due to Single Moving Load, Procedia Engineering, pp. 143-151.

Zhang, N, Xia, H, 2013. Dynamic analysis of coupled vehicle–bridge system based on inter-system iteration method. *Computers & structures* 114, 26-34.

ZHANG, N, XIA, H, Guo, W, and De Roeck, G, 2010. A vehicle–bridge linear interaction model and its validation. *International Journal of Structural Stability and Dynamics* 10 (2), 335-361.

Zheng, Z-Q, Huang, P, Gao, D-X, and Chang, Z-Y, 2015. Analysis of electromagnetic force of the linear generator in point absorber wave energy converters. *Journal of Marine Science and Technology* 23 (4), 475-480.